EXPERIMENTAL AND THEORETICAL STUDIES ON THE DYNAMICS OF DISSOCIATIVE EXCITATIONS OF MOLECULES IN THE GAS PHASE

by Kiyohiko Someda

Thesis submitted to
the University of Tokyo
January, 1988

Acknowledgements

The author takes this opportunity to express his thanks to Professor Kozo Kuchitsu, his thesis advisor, for his guidance and encouragement throughout the present work.

The author is grateful to Professor Tamotsu Kondow for his helpful discussions, suggestions and encouragement.

Grateful acknowlegement is made to Drs. Kaoru Suzuki and Takashi Nagata for their advice and many helpful discussions.

Thanks are given to all the member of Professor Kuchitsu's laboratory for their encouragement and fruitful discussions.

Grateful acknowlegement is made to Dr. Nobuhiro Kosugi for his support in the work on the molecular-orbital calculation.

The author is grateful to Professor Ikuo Tokue for his helpful comments on the analysis of NH(A-X, c-a) emission bands.

Thanks are also given to Professor Hiroki Nakamura for his helpful discussions on the present work.

Contents (page)

PART I. DYNAMICS OF DISSOCIATIVE EXCITATIONS OF MOLECULES IN COLLISION WITH HELIUM METASTABLE ATOMS

PART II. TIME DEPENDENT VARIATIONAL METHOD FOR PHOTODISSOCIATION DYNAMICS

GENERAL INTRODUCTION

Dynamical processes of electronically excited atoms and molecules are one of the fundamental subjects of the study of molecular reaction dynamics. These excited speices have high reactivity and their behavior is variant; many final channels giving different products are open and the branching depends on the electronic state of the reactant. In particular, dissociative excitation is one of the dynamical processes typical of the electronically excited molecules. Dissociation of the molecules can be regarded as the latter half of the full reaction. Therefore, studies on dissociative excitation can serve for understanding some aspects of the reaction dynamics of electronically excited species. In the present study, dynamics of dissociative excitation is investigated experimentally and theoretically. The present study consists of two parts; in part I, dissociative excitation of molecules in collision with helium metastable atoms, $He(2^3S_1)$, is discussed, and in part II, a theory for photodissociation dynamics based on the time-dependent variational principle is developed.

Helium metastable atom, $He(2^3S_1)$, is the helium atom in the lowest triplet excited state, the electron configuration of which is $(1s)^1(2s)^1$, and has a very long lifetime on the order of 10^3 s in the collision-free condition.[1-3] The excitation energy of the $He(2^3S_1)$ atom is 19.81 eV ,[1-3] which is higher than the first ionization potentials of all the atoms and molecules except for He and Ne. When the $He(2^3S_1)$ atom collides with the target molecule, the target molecule is excited to a certain electronically excited state or ionized. The latter process is generally called Penning ionization,[4] on which many investigations have been made by means of electron spectroscopy of the ejected electrons[5] and optical spectroscopy of the product ions.[6] If the target molecule is excited to an electronically excited state of the neutral species, the resultant electronic states should be super-excited states, which are defined as the excited states having excitation energy higher than the first ionzation potential.[7] These super-excited states release their electronic energy through autoionization and dissociation;[7] the probability of the radiative decay of the super-excited states is negligible. The fragments produced in the dissociation of these highly-excited states are often electronically excited, and emission from these fragments can be observed.

The electronically excited states located at about 20 eV can be classified by their electron configurations: singly-excited states and doubly-excited states; in the former, one electron is promoted to a vacant orbital, whereas in the latter, two electrons are promoted. The singly-excited states located at about 20 eV are almost always high-Rydberg states converging to a certain ionic state with a hole in an outer-valence molecular orbital, and usually bound states, potential surfaces of which are similar to those of the corresponding ionic state. On the other hand, the doubly-excited states located at about 20 eV may have either Rydberg- or valence-character and usually dissociative because at least one antibonding molecular orbital is occupied. The singly-excited states often predissociate to the dissociative doubly-excited states. Therefore, these doubly-excited states play a crucial role in dissociative excitation, and the participation of these doubly-excited states, which are located near or above 20 eV, is one of the characteristics of the dissociation dynamics in the energy range in question. However, direct excitation to the doubly-excited states is optically forbidden unless certain singly-excited configurations are mixed with them, whereas in the excitation transfer from He(2^3S_1), it is unknown whether or not such a selection rule with respect to the electron configuration holds.

Dissociative excitation in collision with the He(2^3S_1) atom have not been studied as much as those in collision with other rare-gas metastables, especially those with Ar($^3P_{0,2}$) and Xe($^3P_{0,2}$), on which many investigations have been made.[1-3] In the studies on the reaction of He(2^3S_1), attention has been focused mainly on Penning ionization. This trend can be partly ascribable to the fact that a large portion of the reaction cross section of He(2^3S_1) is carried by Penning ionization, and this is a reflection of the nature of the super-excited states; a large fraction of the super-excited states decay through autoionization, and branching to dissociation is usually small. On the other hand, systematic studies on the nature of the super-excited states itself, which can be studied most effectively by optical spectroscopy in the extended-UV region, is now in progress by utilizing synchrotron-radiation.[8] In this context, studies on dissociative excitation in collision with the He(2^3S_1) atom can provide valuable information on the behavior of these super-excited states, especially of the doubly-excited states, and this information can be complementary to that obtained by optical spectroscopy because the optical selection rule does not necessarily hold in the reaction of He(2^3S_1). On the other hand, dissociation dynamics of the doubly-excited states is expected to be different from that of the singly-excited states located below 10 eV, which are usually studied through excitation by absorption of vacuum-UV photons[9,10] and collision of Ar-, Kr-, and Xe-metastables,[1-3] because the potential surfaces of the doubly-excited states are expected to have topograpy different from those of the singly-excited states due to the difference of the electronic structures.

In the present study, emission from the electronically excited fragments produced in the dissociative excitation in collision with the He(2^3S_1) atoms is observed by a flowing afterglow technique;[1-3] namely, the He(2^3S_1) atoms are generated in a discharge flow and the target gas is introduced about 15 cm downstream from the discharge region into the flow. Emission from the reaction region is focused on the monochromator equipped with a photon-counting system. By analyzing the emission spectra in the UV-visible region, internal-state distributions of the fragments are obtained. The flowing afterglow technique has an advantage, in comparison with a beam technique, that one can obtain emission strong enough to measure high-resolution spectra, and has disadvantages that the pressure of the reaction region is rather high, 0.15-0.4 Torr in the present work, and that several active species other than $He(2^3S_1)$, for example, $He(2^1S_0)$, He^+, He_2^+, and thermal electrons, are simultaneously contained in the flow.[1-3] The former disadvantage is not serious in the present experiment because radiative lifetimes of the excited fragments are short enough that the fragments emit photons before any relaxation and secondary reactions take place. The latter disadvantage can be overcome by making diagnoses on the active species responsible for the observed emission; such diagnoses can be achieved by measuring dependences of the emission intensity on the pressure of the flow and on the potential applied to the retarding grids placed between the discharge region and the reaction region.

On the basis of the observed internal-state distribution of the fragments, dissociation dynamics is discussed. In chapter 1, the rotational distribution of $NH(A^3\Pi,c^1\Pi)$ produced from NH_3 is analyzed and the dynamics of the rotational excitation is discussed from the viewpoint of the motion of the nuclei. The mechanism of the rotational excitation is indicated to be different from that in the photodissociation of NH_3 with lower excitation energy (about 10 eV). In chapter 2, the dissociative excitation of metal-complex molecules, $Fe(CO)_5$ and $Fe(C_5H_5)_2$, is studied. The electronic state distributions of the Fe atom produced show that the motion of the electrons in the Fe atom interacts strongly with the vibration of the ligands; namely, the ligands serve as a heat bath attached to the Fe atom. In chapter 3, the n-distributions of $H(n)$ produced from H_2O, D_2O, and H_2S are discussed. The formation of these excited hydrogen atoms is typical of dissociative excitation with high excitation energy near or above 20 eV, and their n-distributions contain information on the transient Rydberg states of the parent molecule. The rates of dissociation and autoionization of the transient Rydberg states are discussed. In chapter 4, the potential energy surfaces relevant to the dissociative excitation of HCl in collision with He(2^3S_1) are obtained by SCF-CI calculation, and the mechanism of the excitation transfer is studied. The transient dissociative states of HCl are found to be doubly-excited states and the mechanism of formation of the doubly-excited states is discussed from the viewpoint of the behavior of the electrons.

Theories, on which the experimental results such as final-state distribution should be explained, are at present composed of two extremes: those theories which consist of completely qualitative concepts, and those theories which require a large amount of numerical calculation but provide only very limited intuition on the essence of the dynamics. In consequence, the existing theories cannot necessarily lead us to systematic understanding of experimental facts accumlated so far. Difficulties in the theories of dynamics partly originate from the fact that application of the exact quantum-mechanical equations of motion to realistic dynamical processes of molecules requires a considerable amount of calculation. Even when a certain quasi-classical approximation is employed, one needs thousands of classical trajectories in order to obtain final-state distributions. The study presented in chapter 5 aims at developing a theoretical method for obtaining approximately the final-state distributions of photodissociation with a reasonable amount of numerical calculation in such a manner that some intuition on the essence of the dynamics can be obtained. In order to make a physical picture clear, it seems to be effective to trace time evolution of the distribution function in the phase space, especially for discussing the final-state distributions. In the present study, time evolution of the distribution function in the phase space is approximately described by using several variational parameters. The time dependences of these parameters are determined from the time-dependent variational principle, which is generally called TDHF (time-dependent Hartree-Fock) theory and has been employed in nuclear physics.[11] An application of the TDHF theory to dynamical processes of molecules has been proposed by several investigators,[12-16] but the methodology has not yet been established. In the present study, special attention is paid to the distribution function in the phase space; the deformation of the distribution function in the course of time evolution is expressed by a sequence of transformations in the phase space. This method can give us some intuition on the time evolution of the system.

Rererences

(1) Kolts, J.H.; Setser, D.W. in *Reaction Intermediates in the Gas Phase* ed. Setser, D.W.; Academic Press, New York, 1979.

(2) Stedman, D.H.; Setser, D.W. *Progr. Reaction Kinetics* **1971,** *6,* 193.

(3) King, D.L.; Setser, D.W. *Ann. Rev. Phys. Chem.* **1976,** *27,* 407.

(4) Niehaus, A. *Ber. Bunsenges. Phys. Chem.* **1973,** *77,* 632.

(5) Čermák, V. *J. Chem. Phys.* **1966,** *44,* 3774.

(6) Richardson, W.C.; Setser, D.W. *J. Chem. Phys.* **1973,** *58,* 1809.

(7) Nakamura, H. *J. Phys. Chem.* **1984,** *88,* 4812.

(8) Dutuit, O.; Tabche-Fouhaile, A.; Nenner, I.; Frohlich, H.; Guyon, P.M. *J. Chem. Phys.* **1985,** *83,* 584.

(9) Simons, J.P. *J. Phys. Chem.* **1984,** *88,* 1287.

(10) Bersohn, R. *J. Phys. Chem.* **1984,** *88,* 5145.

(11) Negele, J.W. *Rev. Mod. Phys.* **1982,** *54,* 913.

(12) Tishby, N.Z.; Levine, R.D. *Phys. Rev. A* **1984,** *30,* 1477.

(13) Levine, R.D. *J. Phys. Chem.* **1985,** *89,* 2122.

(14) Heller, E.J. *J. Chem. Phys.* **1976,** *64,* 63.

(15) Grad, J.J.; Yuan, Y.J.; Mukamel, S. *Chem. Phys. Letters* **1987,** *134,* 291.

(16) Kucar, J.; Meyer, H.-D.; Cederbaum, L.S. *Chem. Phys. Letters* **1987,** *140,* 525.

PART I

DYNAMICS OF DISSOCIATIVE EXCITATIONS OF MOLECULES IN COLLISION WITH HELIUM METASTABLE ATOMS

Chapter 1

Rotational distribution of NH($A^3\Pi$,$c^1\Pi$) produced from NH_3 in collision with helium metastable atoms

ABSTRACT

The emission spectra of NH($A^3\Pi - X^3\Sigma^-$) and NH($c^1\Pi - a^1\Delta$) produced from NH_3 in collision with $He^m(2^3S_1)$ was measured by a flowing afterglow experiment. The rotational distributions of NH($A^3\Pi$; $v=0, 1$) and NH($c^1\Pi$; $v=0$) obtained from the spectra show intense rotational excitation of the NH radical; the average rotational energies are found to range 0.3-0.5 eV. The observed rotational distributions are analyzed on the basis of a statistical model in which the rotational distribution is governed by the upper limit of the impact parameter of the half collision, $NH_3 \rightarrow NH + H_2$ or 2H. This upper limit of the impact parameter, estimated from the observed rotational distributions, is found to be less than 0.6 Å. This implies that essentially axial recoil of the H atoms takes place. Namely, the rotational excitation of NH is caused almost exclusively by a torque exerted by the dissociating H atoms, and the inversion motion of the transient NH_3 molecule does not significantly contribute to the rotational excitation of NH.

INTRODUCTION

The rotational distribution of the NH radical produced in dissociative excitation of NH_3 molecule has been studied extensively by photoexcitation involving single- and multiphoton processes,[1-6] electron impact,[7,8] and energy transfer from an argon metastable atom[9,10] with excitation energy ranging from the near-threshold up to 12 eV. Intense rotational excitation of the NH radical has often been observed.[2] Such rotational excitation is interpreted to be induced by the inversion motion of the transient NH_3 molecule.[2] The mechanism of the rotational excitation is essentially governed by topography of the potential energy surface of the transient states of NH_3. Therefore, different mechanisms are expected if one allows NH_3 molecule to dissociate from excited states with very different electronic characters.

In order to gain further insight into this problem, a study has been made in the present paper to excite NH_3 to highly excited states located about 20 eV by energy transfer from a helium metastable atom $He^m(2^3S_1)$ and to measure the rotational distribution of the dissociation product $NH(A^3\Pi, c^1\Pi)$. The excited states located at about 20 eV are likely to have doubly excited configurations, and their potential energy surfaces to have very different topography from those of singly excited states.

A simple way to describe the dynamics of rotational excitation of the fragment NH is to use the impact parameter of the half collision, $NH_3 \rightarrow NH + H_2$ or 2H. Namely, if the inversion motion of NH_3 induces the rotational excitation, the impact parameter should be equal to the N-H bond length or larger; on the other hand, if the rotational excitation is caused by axial recoil of the H atoms, the impact parameter should be much smaller. This impact parameter has a certain distribution. However, the impact parameter generally should have an upper limit because the velocity vector of the fragment cannot be changed at a large inter-fragment distance where the interaction fades out. This upper limit of the impact parameter is considered to be one of the quantities which characterize the dissociation dynamics. In the present study, a statistical model in which the rotational distribution is governed by the upper limit of the impact parameter[4,8,11-13] is developed, and mechanism of the rotational excitation of the fragment NH is discussed by analyzing the observed rotational distribution on the basis of this model. The analysis implies that the rotational excitation of NH is caused almost exclusively by a torque exerted by axial bond rupture, but that the inversion motion of the transient NH_3 molecule has little effect. This dissociation dynamics is very different from that in VUV-photodissociation,[2] in which case the inversion motion induces rotational excitation. This difference can essentially be ascribed to the difference in topography of the potential surfaces of the dissociative states. Discussion on the dissociative states indicates that the most probable dissociative states are doubly excited states.

EXPERIMENTAL SECTION

A flowing afterglow method was employed.[14] Helium gas was purified by passing through molecular sieve cooled by liquid nitrogen and led into a discharge region. Helium metastable atoms were generated by a microwave discharge (2.45 GHz, 100 W) and admitted to a reaction tube, which was evacuated by a mechanical booster pump (500 *l*/s). Ammonia gas was introduced into the flow 15 cm downstream from the discharge region. Commercial NH_3 gas (Takachiho, 99.8% purity) was used without further purification. Charged particles such as He^+ and thermal electrons generated in the discharge were removed from the flow by a pair of grids biased at -10 V. The pressures of He and NH_3 in the reaction region, measured by a Pirani gauge, were typically 0.3 Torr and several mTorr, respectively.

The emission from the reaction region was observed through a quartz window, dispersed by a 1 m monochromator (Spex 1704) and detected by a photomultiplier (Hamamatsu R585) and a photon-counting system. The spectral response of the monochromator and the detection system was calibrated by using a standard lamp.

The emission spectrum was measured in the region of 200-500 nm; strong emissions from $NH(A^3\Pi)$ and $NH(c^1\Pi)$ were observed. The spectra of the $NH(A^3\Pi-X^3\Sigma^-)$ 0-0 and 1-1 bands and the $NH(c^1\Pi-a^1\Delta)$ 0-0 band were recorded with a resolution of 0.03 nm (see Figure 1). The wavelength-range where $NH(d^1\Sigma^+-c^1\Pi)$, $NH_2(\tilde{A}^2A_1-\tilde{X}^2A_1)$ and hydrogen Balmer-series emissions were expected was scanned carefully, but none of these emission spectra were detected.

The emission intensities of the NH(A-X) and NH(c-a) bands were found to be independent of the potential applied to the grids. Hence, it was concluded that no charged particles (He^+ and thermal electrons etc.) produced in the discharge contributed to the observed dissociation processes. Furthermore, the intensities showed the dependence on the He pressure from 0.15 to 0.6 Torr which was identical with that of the N_2^+(B-X) 0-0 emission band produced by Penning ionization, $He(2^3S_1)+N_2 \rightarrow He+N_2^+(B)+e$. Therefore, it was confirmed that the active species responsible for the production of $NH(A^3\Pi, c^1\Pi)$ was the $He(2^3S_1)$ atom.

The spectral feature exhibited no distinct change as the He pressure was varied from 0.15 to 0.6 Torr. This observation indicated that collisional relaxation was insignificant. This finding is in line with the following observation reported by Sekiya et al.[10]: The rotational distribution of NH(A,c) obtained by an experiment of Ar flowing afterglow with an Ar pressure ranging 0.2-0.5 Torr was identical with those obtained by an experiment made under a collision-free condition where the Ar pressure was $1-3\times10^{-3}$ Torr. This implies that the radiative lifetimes of NH(A) and NH(c), about 400 ns,[15] are shorter than the relaxation time. One can expect that a similar condition holds for the present experiment of He flowing afterglow because the cross section for the rotational relaxation by collision with He is likely to be smaller than that by collision with Ar.

ANALYSIS

The observed emission spectra were analyzed by means of a computer simulation to determine the rovibrational distributions of NH(A) and NH(c). The emission intensity of a transition from a (v',N') state to a (v'',N'') state is represented by[16]

$$I_{v'N'}^{v''N''}=\nu^3R_{v'v''}\mathrm{Re}_{v'v''}S_{N'N''}\tau_{v'N'}P(v',N') \qquad (1)$$

where ν is the transition frequency, $R_{v'v''}$ is the Franck-Condon factor, $R_{v'v''}$ is the transition dipole, $S_{N'N''}$ is the rotational line strength, $\tau_{v'N'}$ is the natural lifetime of the (v',N') state, and $P(v',N')$ is the rate of formation of the (v',N') state. The transition frequencies reported by Dixon[17] and by Funke[18] were used for the simulation of the A-X band, while the transition frequencies for the c-a band were calculated from the spectroscopic constants reported in ref.19. The Franck-Condon factors and the values of the transition dipole were taken from ref.20. The line strengths for the NH(A-X) transition were calculated according to the formula derived by Budó,[21] by using the spectroscopic constants reported in ref.19. Only the main branches were taken into account, since the line strengths for the satellite branches were negligible in comparison with those for the main branches. The line strengths for the NH(c-a) transition were calculated by the Hönl-London formula.[16] The values of $\tau_{v'N'}$ reported by Smith et al.[15] were used for the lifetimes. A Gaussian slit function was convoluted into the rotational lines to calculate the spectral envelope (see Figure 1). The relative rate of formation for each rovibrational state was estimated by trial and error so as to reproduce the observed spectrum. Uncertainties in the rates of formation were estimated from the limiting values beyond which the discrepancy in the spectral fit became apparent.

RESULTS

The rotational distributions for the NH($A^3\Pi$) $v=0,1$ and NH($c^1\Pi$) $v=0$ states determined by the spectral simulation are shown in Figures 2 and 3, respectively. The rotational distribution for the NH(c) $v=0$ state can be represented by a Boltzmann function with a rotational temperature of $T_{\mathrm{rot}}=3600\pm300$ K. On the other hand, the rotational distributions for the NH(A) $v=0$ and 1 states cannot be represented by a single Boltzmann distribution.

The vibrational distribution of NH(A) and the branching ratio of NH(A) vs. NH(c) are estimated by summation of the rates of formation of all the rovibronic states multiplied by their degeneracies ($2K'+1$ for the $c^1\Pi$ state and $3(2N'+1)$ for the $A^3\Pi$ state):

$$P(\mathrm{NH}(A^3\Pi)v=1)\ /\ P(\mathrm{NH}(A^3\Pi)v=0)=0.3\pm0.1. \tag{2}$$

$$P(\mathrm{NH}(c^1\Pi))\ /\ P(\mathrm{NH}(A^3\Pi))\geq0.5. \tag{3}$$

Only the lower limit of the branching ratio can be given in eq.(3), because the contribution of the predissociative NH($c^1\Pi,v\geq1$) states to $P(\mathrm{NH}(c^1\Pi))$ cannot be estimated properly.

The average rotational energies, $<E_{\mathrm{rot}}>$, for the NH(A) $v=0$ and 1 states are estimated by

$$<E_{\mathrm{rot}}>=\frac{\sum\limits_{N'}E_{N'}(2N'+1)P(v',N')}{\sum\limits_{N'}(2N'+1)P(v',N')}, \tag{4}$$

where $E_{N'}$ is the rotational energy. On the other hand, the $<E_{\mathrm{rot}}>$ value for the NH(c) $v=0$ state is estimated simply by $<E_{rot}>=kT_{rot}$ in order to avoid an underestimate of $<E_{rot}>$ caused by the neglect of the contributions of the higher rotational states which are not observed in the present experiment. The values of $<E_{rot}>$ thus obtained are listed in Table I.

DISCUSSION

A. Identification of the observed processes

The energetically accessible processes which lead to the formation of NH($A^3\Pi$, $c^1\Pi$) are listed in Table II. Processes (C)-(E) cannot be regarded as dominant for formation of NH(A), because the higher rotational states which cannot be produced via these processes are found to have sufficient distributions (see Figure 2). Process (A) is less probable than process (B), because the excess energy in process (A) is so large (12.1 eV) that the internal energy distributed to the vibration of $H_2(X^1\Sigma_g^+)$ is likely to exceed the dissociation energy of $H_2(X^1\Sigma_g^+)$ (4.5 eV). This conjecture is supported by the analysis of the rotational distribution described in subsection C. Accordingly, the process of dissociative excitation responsible for the formation of the NH(A) radical observed is likely to be process (B),

$$He(2^3S_1)+NH_3 \rightarrow He(1^1S_0)+NH(A^3\Pi)+2H(1s). \qquad (5)$$

As for the formation of NH(c), process (F) can be excluded, because this process is spin-forbidden. It is also unlikely that the NH(c) fragment is produced mainly through a radiative cascade from NH(d), since the NH(d-c) emission is not detected. Therefore, process (G) is possibly responsible for the formation of NH(c),

$$He(2^3S_1)+NH_3 \rightarrow He(1^1S_0)+NH(c^1\Pi)+2H(1s). \qquad (6)$$

The fraction of the average rotational energy to the excess energy is estimated in Table I for the NH(A) $v=0$, 1 and NH(c) $v=0$ states by use of the excess energies of the above processes.

B. Upper limit of the impact parameters of the fragments

As shown in Figure 2, the slope of the rotational distribution for NH($A^3\Pi$; $v=0$) increases with the rotational energy, and there is a sudden change in the slope at $N'=17$. This trend indicates that formation of the NH radical which has a large rotational angular momentum is suppressed by a certain dynamical constraint, ascribable to that on the impact parameter of the dissociating fragments, as is often encountered in dissociation dynamics.[23] In the present analysis, the rotational distribution of NH is explained by a statistical model in which this dynamical constraint is taken into account.

The impact parameter for the half collision, $NH_3 \rightarrow NH+H+H$, is subject to the potential energy surfaces of the dissociative states: For example, a large impact parameter is expected if the inversion motion of NH_3 is excited in the dissociation; on the other hand, the impact parameter is small if the H atoms are recoiled coaxially with the N-H bond axis. In general the impact parameter has an upper limit, because the velocity vector of the fragment cannot be changed at a large inter-fragment distance where the interaction practically vanishes. This limit of the impact parameter sets a maximum on the orbital angular momentum, and this upper limit and the conservation of the total angular momentum determine the maximum rotational angular momentum of the NH fragment.

The rotational distribution of NH can be explained by a model that the impact parameter has an upper limit. The details of this model are described in Appendix. The model consists of the following three major assumptions:

Assumption (1): The translational motion of the helium atom does not participate in the disposals of energy and angular momentum throughout the collision. As far as the disposals of energy and angular momentum are concerned, the dissociation dynamics can fully be described by the unimolecular dissociation of the parent molecule in a transient excited state, NH_3^{**}. Furthermore, it follows that the rotational distribution of NH_3^{**} is the Boltzmann distribution at room temperature. The present assumption is valid so far as the translational energy of the outgoing helium atom is thermal.

Assumption (2): If one of the impact parameters of the fragments (two H atoms or one H_2 molecule) exceeds a given upper limit, b_{max}, the dissociation does not occur at all. The actual dynamics may not be so simple, and a certain distribution of the impact parameter must be considered. However, in the present model the restriction on the impact parameter is treated in the simplest way as stated above.

Assumption (3): All the final quantum states which satisfy the conditions set on the impact parameter and the energy and angular momentum conservation are equally probable. This assumption does not necessarily mean that complete energy randomization in NH_3^{**} takes place, but it is an analogue of a prior distribution or a linear surprisal distribution employed in the information theoretic approach to reaction dynamics.[24]

A model calculation is carried out in the following four cases. Cases (1) and (2) correspond to

$$NH_3^{**} \rightarrow NH(A\ \mathrm{or}\ c) + H(1s) + H(1s). \tag{7}$$

The motions of the two H atoms are treated as independent in case (1), whereas a certain correlation between the motions of the two H atom is assumed in case (2), i.e., two H atoms are regarded as a single fragment which has no rovibrational degrees of freedom. Cases (1) and (2) correspond to "three-body dissociation" and "two-body dissociation," respectively. On the other hand, cases (3) and (4) correspond to

$$NH_3^{**} \rightarrow NH(A\ \mathrm{or}\ c) + H_2(X^1\Sigma_g^+). \tag{8}$$

In case (3), no restriction other than the conservation of angular momentum is placed on the rotation of H_2(X), while it is assumed in case (4) that no torque works on H_2. The details of these cases are described in Appendix.

C. Analysis of the rotational distribution

The relative rates of formation, $P(N')$, are calculated acoording to the formulas described in Appendix (eq A5, A12, A17, and A21), and the rotational distributions thus obtained are fitted to the experimental ones by adjusting the $b_{\max}$ parameter and the scaling factor which determines the magnitude of the calculated $P(N')$ as a whole. The parameters are determined independently for the three vibronic states, $A^3\Pi(v=0$, and $1)$ and $c^1\Pi(v=0)$. The results are shown in Figures 4-8.

The $A^3\Pi(v=0)$ *state*: The experimental distribution can be reproduced in cases (1) and (2), but not in cases (3) and (4) (see Figure 4). Therefore, it is unlikely that molecular elimination (processes (C),(D), and (E) in Table I) takes place. This statement is consistent with the discussion in subsection A. In case (1), the slope of the distribution at higher N' is well reproduced, although agreement is less satisfactory at lower N'. On the other hand, the overall feature of the experimental distribution is well reproduced in case (2). However, one cannot draw any definitive conclusion as to which of cases (1) or (2) is to be favored. These mechanisms are two extremes, and the actual mechanism may well be an intermediate. Namely, it is probable that the motions of the two H atoms are neither purely independent nor strongly correlated.

The $A^3\Pi(v=1)$ *state*: The distribution can be reproduced by cases (1) and (2) (see Figure 7). A good agreement is obtained with case (1), but for case (2) the agreement is restricted to higher N'. Cases (3) and (4) cannot reproduce the experimental distribution. As in the case of the $A^3\Pi(v=0)$ state, cases (1) and (2) are both acceptable, but case (1) (independent motions of the H atoms) is clearly favored in this case.

The $c^1\Pi(v=0)$ *state*: A good agreement is obtained with cases (1) and (2). Molecular elimination (process F in Table II), which corresponds to cases (3) and (4), can be excluded by the spin-conservation rule (see subsection A), but the distribution can also be reproduced for cases (3) and (4). In conclusion, the number of experimental data is not sufficient for determining the mechanism for production of NH(c).

D. The values of $b_{\max}$ *and the dissociation dynamics*

The values of $b_{\max}$ which result in the best fit for each vibronic state and for each case are listed in Table III. The optimum values of $b_{\max}$ are all very small, i.e., they are even smaller than the N-H bond length for $NH_3(\tilde{X})$, 1.0 Å. Therefore, it can be concluded that essentially axial recoil of the H atoms takes place. In this case, the two H atoms dissociate along the N-H bond axis, and the rotational excitation of NH is ascribed only to the torque exerted on NH by the N-H bond rupture. This means that the inversion motion of the parent NH_3 molecule has little effect on the rotational excitation of the NH fragment. This dissociation dynamics is opposite to that in the VUV-photodissociation of NH_3,[1-4] in which case the inversion motion is believed to play a crucial role in the NH rotational excitation.

One can consider two possible explanations for the axial recoil: (1) Because of the large excess energy ($\approx$ 7 eV) the H atoms dissociate along a very steep repulsive wall of the potential surface, and therefore, the energy of the inversion motion is negligible in comparison with that of the dissociative motion along the N-H bond axis. (2) If the equilibrium structure of the transient NH_3^{**} molecule is pyramidal, it is unlikely that the inversion motion is excited significantly.

E. Dissociative states

The electron configuration of the ground state NH_3 is

$$(1a_1)^2(2a_1)^2(1e)^4(3a_1)^2.$$

The ionization potentials are listed in Table IV. No precise knowledge is available on the neutral excited states located near the excitation energy of $He(2^3S_1)$, 19.8 eV. The neutral excited states in this region are generally classified into the following four types:

I valence-type singly excited states
II valence-type doubly excited states
III Rydberg-type singly excited states
IV Rydberg-type doubly excited states

In the present section, possible dissociative states are examined for each type and it is shown that excited states of type II are the most probable dissociative states.

Type I: The excitation energy, 19.8 eV, exceeds the ionization potentials of the $(3a_1)^{-1}$ and $(1e)^{-1}$ ionic states. Therefore, the excited states of the present type located near 19.8 eV should have one hole in the $2a_1$ orbital. This $2a_1$ orbital is the inner-valence orbital and has a character of the 2s orbital of the N atom. Excitation to this inner-valence excited state by collision with $He(2^3S_1)$ reqires overlap of the $2a_1$ orbital of NH_3 with the 1s orbital of $He(2^3S_1)$.[26] Since the electron density of the $2a_1$ orbital is localized inside the NH_3 molecle, the excitation to such an inner-valence excited state by collision with $He(2^3S_1)$ is expected to be inefficient.

Type II: Possible excited states of this type located near 19.8 eV are those states which are obtained by promoting two electrons from the outer-valence orbitals, $3a_1$, and 1e, to certain antibonding orbitals. These excited states, which are expected to be repulsive because two of the antibonding orbitals are occupied, are suitable candidates for the dissociative states in question.

Type III: The excited states of this type corresponds to the Rydberg states converging to $(3a_1)^{-1}$, $(1e)^{-1}$, and $(2a_1)^{-1}$ ionic states. The ionization potential of the $(2a_1)^{-1}$ ionic state, 27 eV, is so high that the Rydberg states converging to this limit are expected to be inaccessible at 19.8 eV. As for the $(3a_1)^{-1}$, and $(1e)^{-1}$ ionic states, an examination on the photoelectron spectrum indicates that the vibrational states of these ionic states are not accessible by the vertical transition at 19.8 eV. Since excitation by collision with $He(2^3S_1)$ generally follows the Franck-Condon principle,[27] excitation to the Rydberg states converging to these ionic states is not expected to take place.

Type IV: Excited states of this type is formed when one electron is promoted to a Rydberg orbital and another electron is promoted simultaneously to a certain antibonding orbital. Excitation to the corresponding ionic states also requires two-electron promotion, which is optically forbidden. In consequence, the corresponding photoelectron bands are not found in ordinary photoelectron spectra. However, the existence of such ionic states at about 19.8 eV is indicated by Kronebusch et al.[28]: They found that the onset of formation of NH^+ by the dissociative photoionization of NH_3 ranged from 17.6 eV (thermochemical threshold) to 21.2 eV (minimum photon energy for detection of NH^+) and that the cross section for formation of NH^+ was about 1/100 of those for formation of NH_3^+ and NH_2^+. Since there are no ionic states produced by one-electron promotion in the energy range of 17.6-21.2 eV, this onset indicates that the ionic state formed by the two-electron promotion from $NH_3(\tilde{X})$ is located in this region, and excitation to this state leads to the formation of NH^+. According to the ion-core model,[29,30] however, excitation to the Rydberg states converging to this ionic state gives NH radical in the Rydberg-type excited states instead of the valence-type excited states such as $A^3\Pi$ and $c^1\Pi$; hence, these Rydberg states are not likely to be the dissociative states involved in the dissociation discussed in the present paper.

In conclusion, the excited states of type III can be excluded, and those of types I and IV are considered to be unlikely. Therefore, the most probable dissociative states belong to type II. Nevertheless, one cannot assign the dissociative states in more detail because of the lack of further precise information on the neutral excited states located at about 19.8 eV.

APPENDIX : *Rotational distribution resulting from the upper limit of the impact parameters*

The present model is based on the model that the rotational distribution of the NH fragment is governed by the upper limit of the impact parameters of the half collision of the fragments in the dissociation. According to the difference in the motions of the two H atoms, the following four cases are considered:

Case (1): One considers unimolecular dissociation of the transient excited parent molecule, NH_3^{**} [Assumption (1) in Discussion B],

$$NH_3^{**} \rightarrow NH + H_a + H_b. \tag{A}$$

Conservation of the energy and that of the angular momentum leads to the following relations:

$$E_a + E_b + B_{NH}N(N+1) = E_{ex}, \tag{A1}$$

and

$$\mathbf{J} = \mathbf{N} + \mathbf{l}_a + \mathbf{l}_b, \tag{A2}$$

where

$$E_{ex} = (\text{excitation energy of He}(2^3S_1)\text{:}19.8\text{ eV}) \\ -(\text{dissociation energy}) - (\text{vibronic energy of NH}).$$

Here, **J** and **N** are the rotational angular momenta of NH_3^{**} and NH, respectively, $\mathbf{l}_i$ is the orbital angular momentum of the relative motion of NH and

H_i, B_{NH} is the rotational constant of NH, and E_i is the kinetic energy of the relative motion of NH and H_i, where i=a,b. Since $m_H/m_N \ll 1$, where m_H and m_N are the masses of the H and N atoms, respectively, $\mathbf{l}_i$ can be related to the impact parameter, b_i, of the relative motion of NH and H_i by

$$|\mathbf{l}_i| \approx m_H v_i b_i = (2m_H E_i)^{1/2} b_i, \tag{A3}$$

where v_i is the velocity of the relative motion of NH and H_i, and the atomic units are employed.

It is assumed that the impact parameter has an upper limit, b_{max}; namely, $b_i \leq b_{max} (i=\mathrm{a,b})$ [Assumption (2)]. This condition places a restriction on $\mathbf{l}_i$:

$$|\mathbf{l}_i| \leq |\mathbf{l}_i^{max}| \approx (2m_H E_i)^{1/2} b_{max}, \tag{A4}$$

and this restriction sets a limit on **N** by eq (A2).

It is further assumed that all the accessible final quantum states are equally probable [Assumption (3)]. A group of the dissociative states of NH_3** having energy E and angular momentum **J** are evolved into a group of final states having energy E and angular momenta **N**, $\mathbf{l}_a$, and $\mathbf{l}_b$, which satisfy eq (A2) and (A4). The last assumption means that all the members of this group have equal rates of formation. Therefore, the rate of formation, $P(N)$, of the NH fragment having a given rotational quantum number N is obtained by counting the number of final quantum states having N which satisfies eq (A1), (A2), and (A4). In this counting procedure, one needs to consider the initial distribution of **J**, which originates from the rotation of NH_3**, by introducing a weight factor $g(J)$. Accordingly, $P(N)$ is given by

$$P(N) \propto \iint_{D_1} \mathrm{d}E_a \mathrm{d}E_b \sum \sum_{(\mathbf{l}_a,\mathbf{l}_b,\mathbf{J}) \in D_2} \sum g(J) \rho(E_a) \rho(E_b), \tag{A5}$$

where

$$D_1: E_a + E_b = E_{ex} - B_{NH} N(N+1) \text{ and } E_a, E_b \geq 0, \tag{A6}$$

$$D_2: \{(\mathbf{l}_a,\mathbf{l}_b,\mathbf{J}) \,|\, \mathbf{l}_a + \mathbf{l}_b + \mathbf{N} = \mathbf{J},\ |\mathbf{l}_i| \leq (2m_H E_i)^{1/2} b_{max}\} \ (i=\mathrm{a,b}), \tag{A7}$$

and

$$\rho(E_i) = (E_i)^{1/2} \quad (i = \mathrm{a,b}). \tag{A8}$$

Here, $\rho(E_i)$ represents the energy dependence of the density of states of the three-dimensional translation. It is assumed that the rotational distribution of NH_3** is a Boltzmann function with a rotational temperature $T_{\mathrm{rot}} = 300$ K; it therefore follows that

$$g(J) \propto \sum_{K=-J}^{J} \exp[-\{BJ(J+1) + (C-B)K^2\}/kT_{\mathrm{rot}}], \tag{A9}$$

where B and C are the rotational constants of NH_3, and K is the projection of **J** onto the c-axis. It is noted that the $(2J+1)$-fold degeneracy with respect to M_J (z-projection of **J**) is automatically taken into account in the summation in eq (A5).

Case (2): In this case, one considers the same unimolecular dissociation, reaction (A), as in case (1) except that complete correlation between the motions of the two H atoms is assumed. This assumption implies that the momentum vector of one H atom is specified uniquely, if one specifies the momentum vector of the other H atom. One possible physical picture is that the two H atoms dissociate in such a manner that the plane of symmetry of the system is conserved. In this case, one can regard the two H atoms as one fragment with no rovibrational degree of freedom. Then, the conditions of the conservation of energy and angular momentum are represented as

$$E_{\mathrm{k}} + B_{\mathrm{NH}} N(N+1) = E_{\mathrm{ex}}. \tag{A10}$$

and

$$\mathbf{J} = \mathbf{N} + \mathbf{l}, \tag{A11}$$

where E_{k} and **l** represent the kinetic energy and the orbital angular momentum of the "fragment (H-H)," and the definition of E_{ex} is identical with that in case (1) (see eq (A1) and (A2)). Equation (A5) is modified as follows:

$$P(N) \propto [\sum_{(\mathbf{l},\mathbf{J}) \in D} \sum g(J)] \rho(E_{\mathrm{k}}(N)), \tag{A12}$$

where

$$E_k(N) = E_{ex} - B_{NH}N(N+1), \tag{A13}$$

and

$$D:\{(\mathbf{l},\mathbf{J})|\mathbf{l}+\mathbf{N}=\mathbf{J},\ |\mathbf{l}|\leq(4m_H E_k)^{1/2}b_{max}\}. \tag{A14}$$

The definitions of $g(J)$ and $\rho(E_k(N))$ are the same as those in case (1) (see eq (A8) and (A9)).

Case (3): The dissociation process,

$$NH_3^{**} \rightarrow NH + H_2\ , \tag{B}$$

is considered in this case. Conservation of the energy and the angular momentum is represented by

$$E_k + E_{vib} + B_{H_2}K(K+1) + B_{NH}N(N+1) = E_{ex}\ , \tag{A15}$$

and

$$\mathbf{J} = \mathbf{N} + \mathbf{K} + \mathbf{l}, \tag{A16}$$

where $\mathbf{K}$ is the rotational angular momentum of H_2, E_k and $\mathbf{l}$ are the kinetic energy and the orbital angular momentum of the relative motion of NH and H_2, respectively, B_{H_2} is the rotational constant of H_2, E_{vib} is the vibrational energy of H_2, and other notations follow case (1) (see eq (A1) and (A2)). The orbital angular momentum, $\mathbf{l}$, is assumed to have the upper limit determined by b_{max} (see eq (A4)), whereas no restriction is set on the magnitude of $\mathbf{K}$. The rate of formation, $P(N)$, is represented by

$$P(N) \propto \sum_{v}\sum \sum_{(\mathbf{J},\mathbf{l},\mathbf{K})\in D} \sum g(J)\rho(E_k), \tag{A17}$$

where

$$E_k = E_{ex} - E_{vib}(v) - B_{NH}N(N+1) - B_{H_2}K(K+1), \tag{A18}$$

and

$$D:\{(\mathbf{l},\mathbf{K},\mathbf{J})|\mathbf{l}+\mathbf{K}+\mathbf{N}=\mathbf{J},\ |\mathbf{l}|\leq(4m_H E_k)^{1/2}b_{max}\}. \tag{A19}$$

The definitions of $g(J)$ and $\rho(E_k)$ are the same as those in case (1) (see eq

(A8) and (A9)), and $E_{\rm vib}(v)$ is evaluated by

$$E_{\rm vib}(v)=\omega_e(v+\frac{1}{2})-\omega_e x_e(v+\frac{1}{2})^2. \qquad \text{(A20)}$$

The summation over v in eq (A17) is taken up to the dissociation limit of $H_2(X)$.

Case (4): In this case, one considers the process in case (3) except for the additional assumption that no torque works on H_2 in the dissociation. With this condition, **K** is always perpendicular to **N**, and the rotation of H_2 originates only from that of the parent molecule. Conservation of energy and that of angular momentum are the same as those in case (3) (eq (A15) and (A16)). The rate of formation, $P(N)$, is expressed as

$$P(N)\propto\sum_v\sum\sum_{(\mathbf{J},\mathbf{l},\mathbf{K})\in D}\sum g(J)g'(K)\rho(E_k), \qquad \text{(A21)}$$

where

$$D:\{(\mathbf{J},\mathbf{l},\mathbf{K})|\mathbf{l}+\mathbf{K}+\mathbf{N}=\mathbf{J},\ \mathbf{K}\cdot\mathbf{N}=0,\ |\mathbf{l}|\le(2m_H E_k)^{1/2}b_{\max}\}. \qquad \text{(A22)}$$

The definition of E_k is identical with that in eq (A17), and the rotational distribution of H_2, $g'(K)$, is assumed to be the Boltzmann distribution at 300 K. The condition that $\mathbf{K}\cdot\mathbf{N}=0$ is treated in the counting of quantum states as follows: If $\mathbf{K}\cdot\mathbf{N}=0$, the vector sum, **M**, of **N** and **K** are given by

$$|\mathbf{M}|^2=|\mathbf{N}|^2+|\mathbf{K}|^2. \qquad \text{(A23)}$$

The representation in which $|\mathbf{M}|^2$, $|\mathbf{N}|^2$, and $|\mathbf{K}|^2$ are simultaneously diagonal being taken, one obtains that

$$M(M+1)=N(N+1)+K(K+1). \qquad \text{(A24)}$$

Since M, N, and K are all integers, eq (A24) is not satisfied except by chance. Namely, the geometrical condition that **N** is parpendicular to **K** is meaningful only in the classical limit, because the direction of the angular momentum is not observable in quantum mechanics. In the present analysis, M is calculated by solving eq (A24) with given N and K, and then this value is replaced by the nearest integer.

References

(1) Kawasaki, M.; Tanaka, I. *J. Phys. Chem.* **1974,** *78,* 1784.

(2) Quinton, A.M.; Simons, J.P. *Chem. Phys. Letters* **1981,** *81,* 214.

(3) Quinton, A.M.; Simons, J.P. *J. Chem. Soc., Faraday Trans.* 2 **1982,** *78,* 1261.

(4) Washida, N.; Inoue, G.; Suzuki, M.; Kajimoto, O. *Chem. Phys. Lett.* **1985,** *114,* 274.

(5) Haak, H.K.; Stuhl, F. *J. Phys. Chem.* **1984,** *88,* 2201.

(6) Hellner, L.; Grattan, K.T.V.; Hutchinson, M.H.R. *J. Chem. Phys.* **1984,** *81,* 4389.

(7) Tokue, I.; Iwai, M. *Chem. Phys.* **1980,** *52,* 47.

(8) Tokue, I.; Ito, Y. *Bull. Chem. Soc. Jpn.* **1985,** *58,* 3480.

(9) Tabayashi, K.; Shobatake, K. *J. Chem. Phys.* **1986,** *84,* 4930.

(10) Sekiya, H.; Nishiyama, N.; Tsuji, M.; Nishimura, Y. *J. Chem. Phys.* **1987,** *86,* 226.

(11) Pechukas, P.; Light, J.C.; Rankin, C. *J. Chem. Phys.* **1966,** *44,* 794.

(12) Light, J.C. *J. Chem. Phys.* **1964,** *40,* 3221.

(13) Powis, I. *J. Chem. Soc., Faraday Trans.* 2 **1981,** *77,* 1433.

(14) Ozaki, Y.; Kondow, T.; Kuchitsu, K. *Chem. Phys.* **1986,** *109,* 345.

(15) Smith, W.H.; Brzozowski, J.; Erman, P. *J. Chem. Phys.* **1976,** *64,* 4628.

(16) Kovacs, I. *Rotational Structure in the Spectra of Diatomic Molecules*; Hilger: London, U.K., 1969.

(17) Dixon, R.N. *Can. J. Phys.* **1959,** *37,* 1171.

(18) Funke, G. *Z. Physik* **1935,** *96,* 787.

(19) Huber, K.P.; Herzberg, G. *Constants of Diatomic Molecules*; Van Nostrand, New York, 1979.

(20) Smith, W.H.; Liszt, H.S. *J. Quant. Spectry. Radiat. Transfer* **1971,** *11,* 45.

(21) Budó, A. *Z. Physik* **1937,** *105,* 579.

(22) Okabe, H. *Photochemistry of Small Molecules*; John Wiley; New York, 1978.

(23) Lu, R.; Halpern, J.B.; Jackson, W.M. *J. Phys. Chem.* **1984,** *88,* 3419.

(24) Levine, R.D. *Ann. Rev. Phys. Chem.* **1978,** *29,* 59.

(25) Kimura, K.; Katsumata, S.; Achiba, Y; Yamazaki, T.; Iwata, S. *Handbook of HeI Photoelectron Spectra of Fundamental Organic Molecules*; Japan Scientific Societies Press: Tokyo, 1981.

(26) Ohno, K.; Mutoh, H.; Harada, Y. *J. Am. Chem. Soc.* **1983,** *105,* 4555.

(27) Niehaus, A. *Ber. Bunsenges. Phys. Chem.* **1973,** *77,* 632.

(28) Kronebusch, P.L.; Berkowitz, J. *Int. J. Mass Spectry.* and *Ion Phys.* **1976,** *22,* 283.

(29) Schiavone, J.A.; Smyth, K.C.; Freund, R.S. *J. Chem. Phys.* **1975,** *63,* 1043.

(30) Carnahan, B.L.; Zipf, E.C. *Phys. Rev. A* **1977,** *16,* 991.

TABLE I

Partition of rotational energy to NH from NH_3 by impact of $He(2^3S_1)$.

states	$<E_{rot}>$/eV[a)]	E_{ex}/eV[b)]	$<E_{rot}>/E_{ex}$
NH(A) $v=0$	0.46(5)	7.6	0.060(6)
NH(A) $v=1$	0.41(4)	7.3	0.056(6)
NH(c) $v=0$	0.33(3)	6.0	0.055(6)

a) Average rotational energy obtained in the present study. Values in parentheses represent errors.

b) Excess energy, calculated by use of data in refs. 19 and 22.

TABLE II

Energetically possible processes in the $He(2^3S_1)+NH_3$ reaction forming NH(A) and NH(c)

$He(2^3S_1)+NH_3 \rightarrow$	E_{ex}/eV	
$He(1^1S_0)$ + $NH(A^3\Pi)$ + $H_2(X^1\Sigma_g^+)$	12.1	(A)
$He(1^1S_0)$ + $NH(A^3\Pi)$ + 2H(1s)	7.6	(B)
$He(1^1S_0)$ + $NH(A^3\Pi)$ + $H_2(B^1\Sigma_u^+)$	0.9	(C)
$He(1^1S_0)$ + $NH(A^3\Pi)$ + $H_2(c^3\Pi_u)$	0.3	(D)
$He(1^1S_0)$ + $NH(A^3\Pi)$ + $H_2(a^3\Sigma_g^+)$	0.3	(E)
$He(1^1S_0)$ + $NH(c^1\Pi)$ + $H_2(X^1\Sigma_g^+)$[a]	10.4	(F)
$He(1^1S_0)$ + $NH(c^1\Pi)$ + 2H(1s)	6.0	(G)

a) This process does not conserve the spin angular momentum.

TABLE III

Optimum values of b_{max} (in Å).[a]

	cases			
	(1)	(2)	(3)	(4)
$A^3\Pi$ $v=0$	0.5	0.3	–[b]	–[b]
$A^3\Pi$ $v=1$	0.6	0.3	–[b]	–[b]
$c^1\Pi$ $v=0$	0.5	0.3	0.05	0.1

a) The upper limit of the impact parameter is denoted as b_{max}. See Discussion B and D.

b) No close fitting could be obtained in these cases.

TABLE IV

Ionization potentials for NH_3

states	$(3a_1)^{-1}$	$(1e)^{-1}$	$(2a_1)^{-1}$
IP/eV[a)]	10.85	15.8	27

a) Ionization potentials taken from ref. 25

Figure Captions

Figure 1: Emission spectra of the NH($A^3\Pi-X^3\Sigma^-$) and NH($c^1\Pi-a^1\Delta$) bands. The upper trace is the spectrum obtained from NH_3 in the He flowing afterglow. The resolution was 0.03 nm (FWHM). The lower trace is a simulated spectrum.

Figure 2: Rotational distributions of NH($A^3\Pi$; $v=0,1$). The rates of formation, $P(N')$, were normalized against that of NH($A^3\Pi$; $v=0; N=1$). The distribution for $v=0$ can be represented by two straight lines with different slopes; see Discussion B. The broken line represents a prior distribution for NH($A^3\Pi$; $v=0$).

Figure 3: Rotational distribution of NH($c^1\Pi$; $v=1$). The line represents a Boltzmann distribution with a rotational temperature of 3600 K.

Figure 4: Rotational distribution of NH($A^3\Pi$; $v=0$) calculated by a model for cases (1)-(4) (see Discussion B and C): — corresponds to case (1) with $b_{\max}$ = 0.5 Å, --- to case (2) with $b_{\max}$ = 0.3 Å, –·– to case (3) with $b_{\max}$ = 0.03 Å, and –··– to case (4) with $b_{\max}$ = 0.05 Å. Closed circles represent the relative rates of formation obtained experimentally.

Figure 5: Rotational distribution of NH($A^3\Pi$; $v=0$) calculated by the model for case (1) with three different values of $b_{\max}$; — corresponds to $b_{\max}$ = 0.5 Å, --- to $b_{\max}$ = 0.6 Å, and –·– to $b_{\max}$ = 0.4 Å. Closed circles represent the experimental data.

Figure 6: Rotational distribution of NH($A^3\Pi$; $v=0$) calculated by the model for case (2) with three different values of $b_{\max}$; — corresponds to $b_{\max}$ = 0.30 Å, --- to $b_{\max}$ = 0.36 Å, and –·– to $b_{\max}$ = 0.27 Å. Closed circles represent the experimental data.

Figure 7: Rotational distribution of NH($A^3\Pi$; $v=1$) calculated by the model for cases (1)-(4); — corresponds to case (1) with $b_{\max}$ = 0.6 Å, --- to

case (2) with $b_{\max} = 0.3$ Å, —·— to case (3) with $b_{\max} = 0.05$ Å, and —··— to case (4) with $b_{\max} = 0.05$ Å. Closed circles represent the experimental data.

Figure 8: Rotational distribution of NH(c$^1\Pi$; $v=0$) calculated by the model for cases (1)-(4); — corresponds to case (1) with $b_{\max} = 0.5$ Å, --- to case (2) with $b_{\max} = 0.3$ Å, —·— to case (3) with $b_{\max} = 0.05$ Å, and —··— to case (4) with $b_{\max} = 0.1$ Å. Closed circles represent the experimental data.

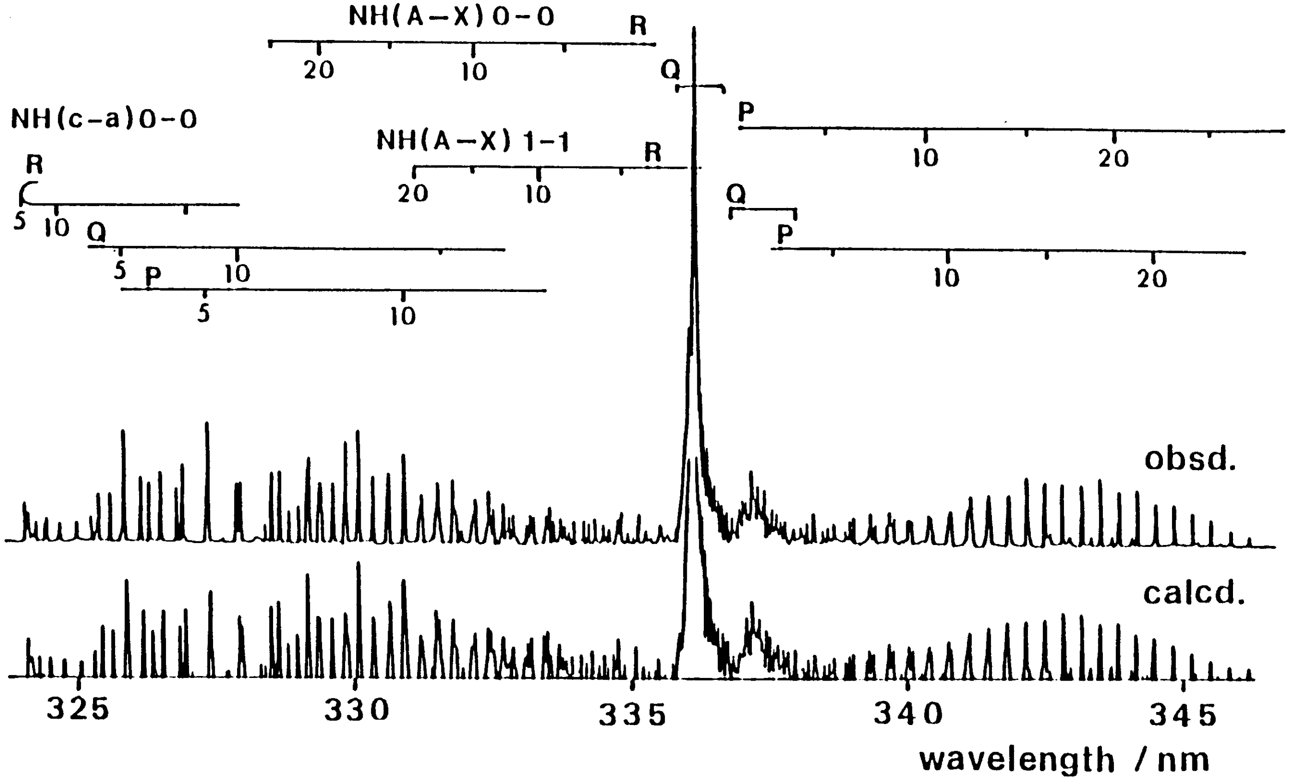
NH(A−X) 0−0
R
20
10
Q
P
10
20
NH(c−a) 0−0
R
5
10
Q
5
10
P
5
10
NH(A−X) 1−1
R
20
10
Q
P
10
20
obsd.
calcd.
325
330
335
340
345
wavelength / nm

Figure 1

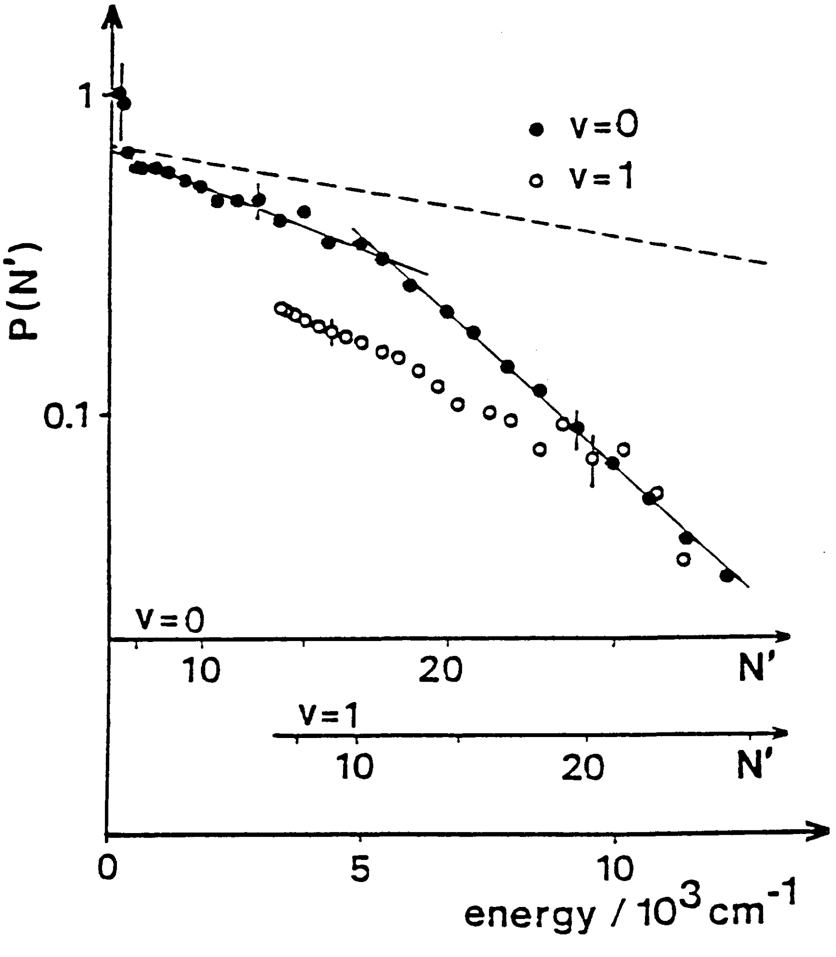

Figure 2

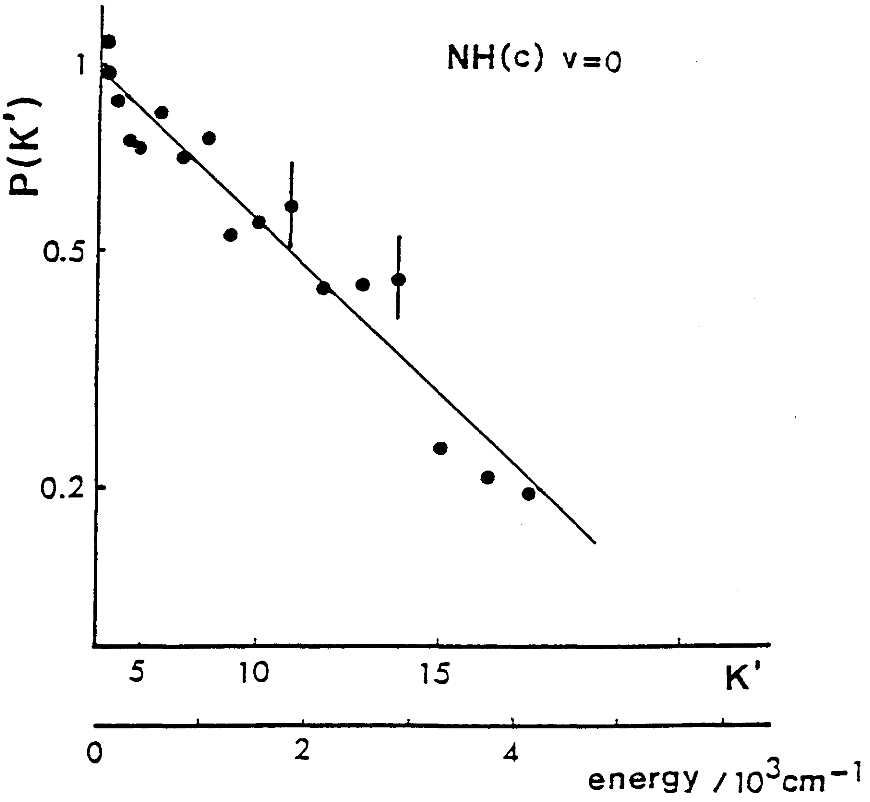

Figure 3

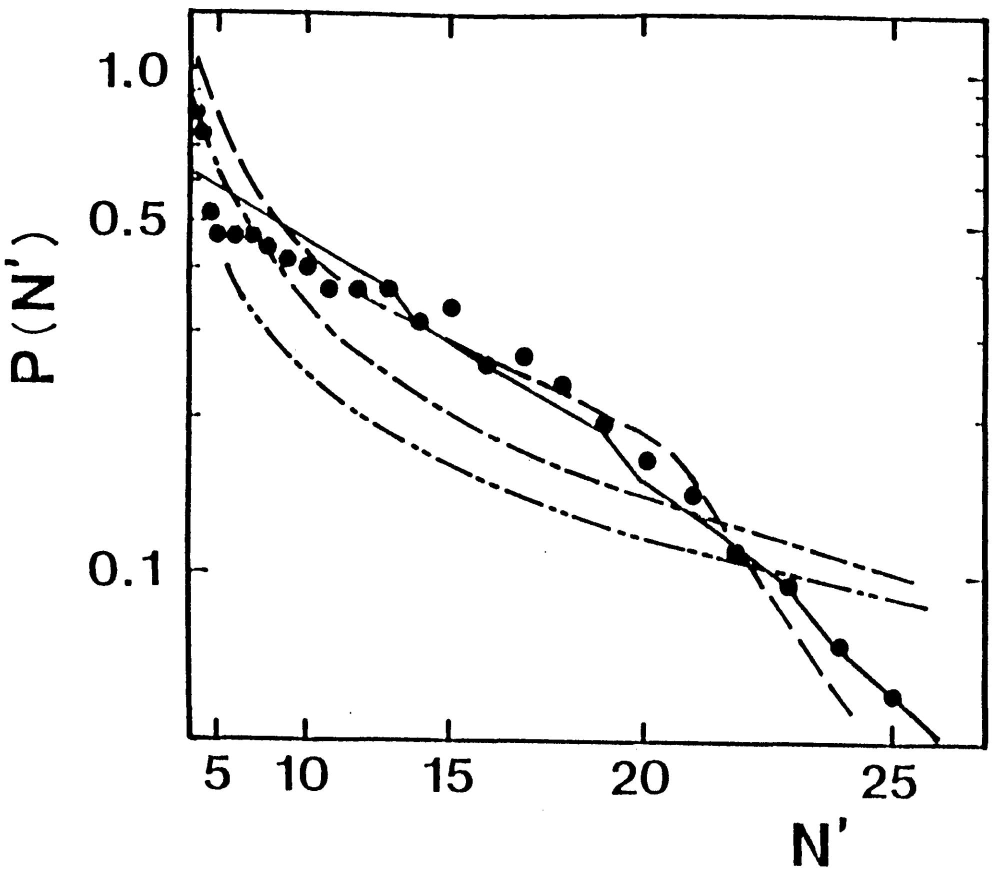

Figure 4

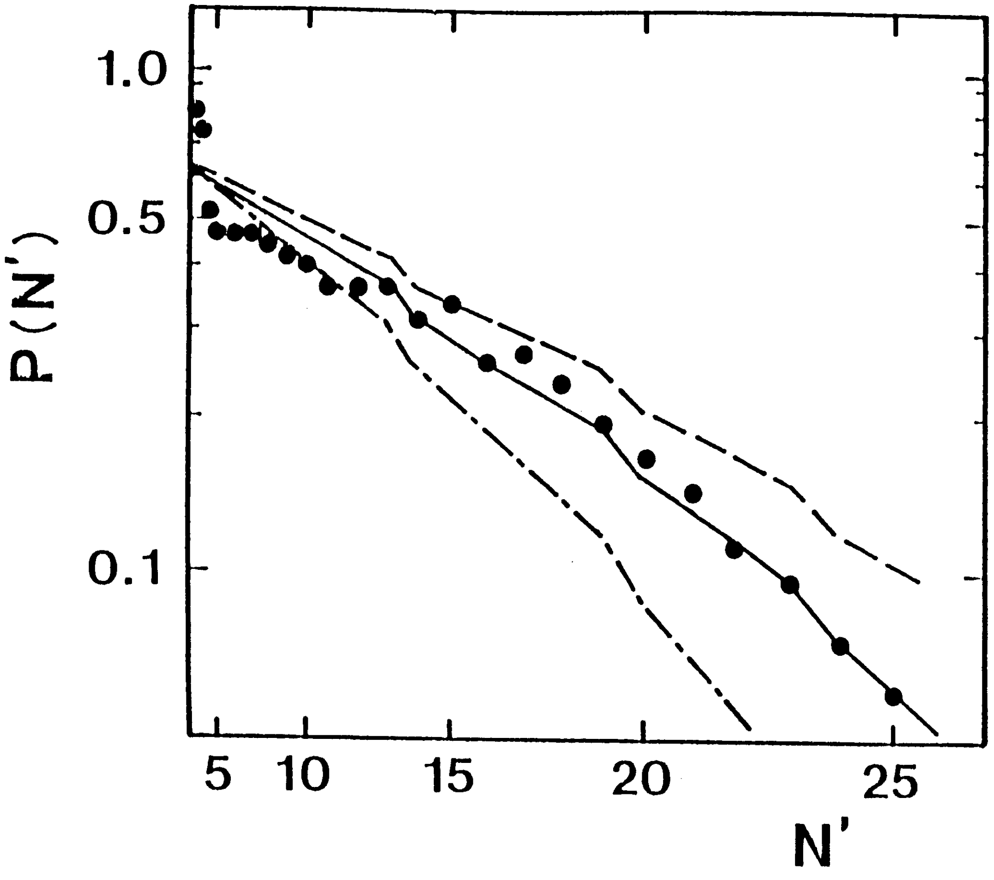

Figure 5

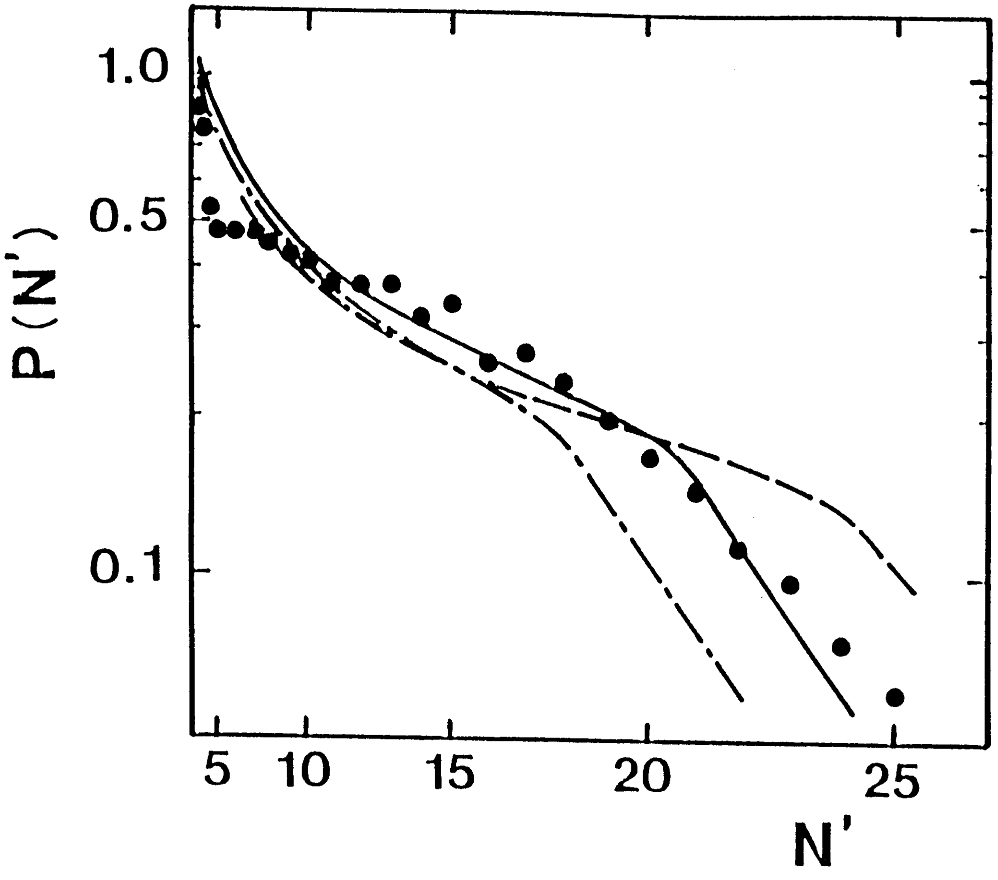

Figure 6

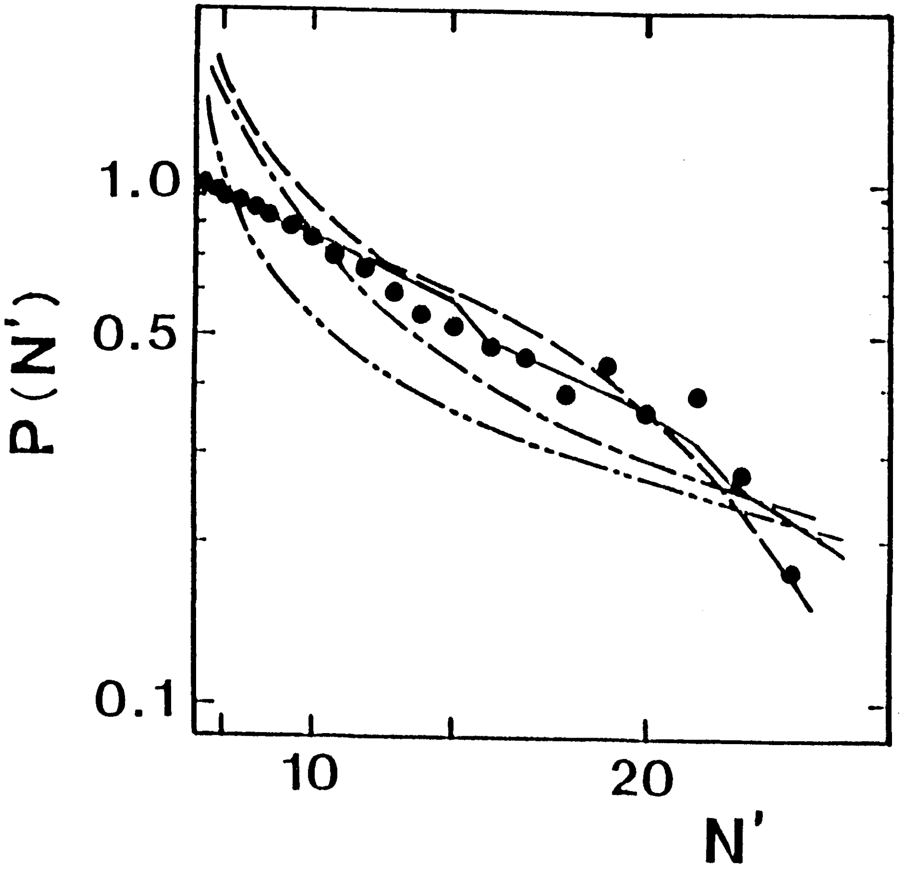

Figure 7

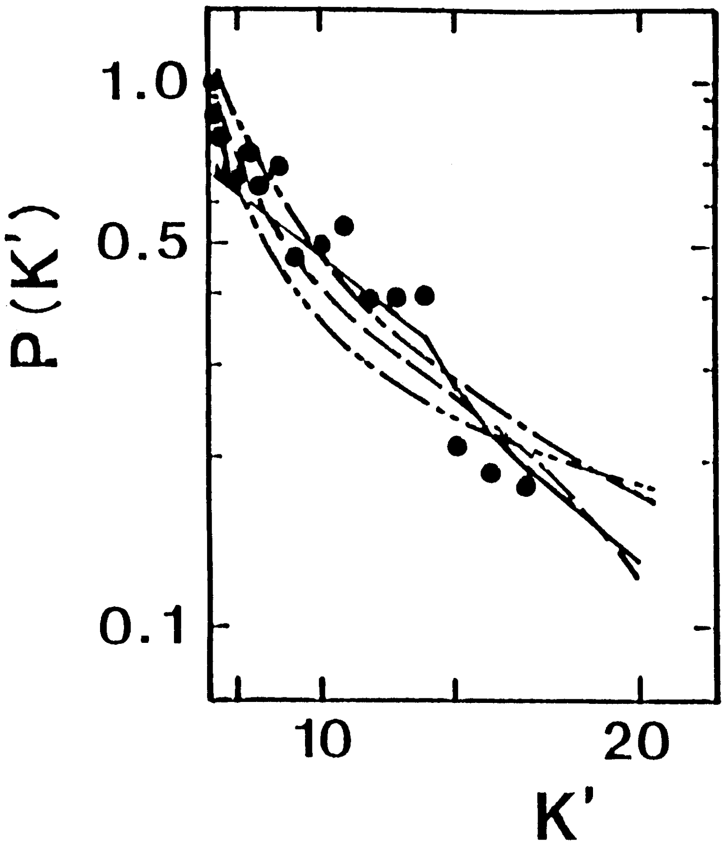

Figure 8

Chapter 2

Electronic State Distributions of Fe Atoms Produced $Fe(CO)_5$ and $Fe(C_5H_5)_2$

ABSTRACT

Dissociative excitations of $Fe(CO)_5$ and $Fe(C_5H_5)_2$ in collision with $He(2^3S_1)$ are investigated. The emission spectra of the excited Fe atoms produced in these reactions are analyzed, and the electronic-state distributions are obtained. A statistical model is developed for interpreting these state distributions, from which the energy partitioning between the Fe atom and the ligands is studied. A consideration of the molecular-orbital correlation indicates that the dissociative states are formed by electron rearrangement in the transient excited states of the parent molecule primarily produced in the collision with $He(2^3S_1)$. The modes of nuclear motions of the ligands which mainly participate in the energy partitioning are assigned by assuming that the energy partitioning occurs in this electron rearrangement accompanied by the vibrational excitation of the parent molecule.

INTRODUCTION

Electronically excited Fe atoms are produced in dissociative excitations of $Fe(CO)_5$ and $Fe(C_5H_5)_2$ by various excitation methods such as photoexcitation,[1-12] electron impact,[13] and collision with active nitrogen[14] or rare gas metastable atoms.[15-18] In the processes of dissociative excitation, a metal-complex molecule can be regarded as a metal atom embedded in a heat bath, between which the excess energy of the reaction is distributed. The electronic-state distributions of the metal atom produced in these processes contain information on the interaction between the motions of the electrons in the metal atom and the nuclear motions of the ligands.

In particular, excitation by collision with the He metastable atom, $He^m(2^3S_1)$, is characterized by the following features: The excitation energy of the He^m atom, 19.8 eV, is sufficient to excite the target molecule to certain superexcited states such as Rydberg states with an excited ion core. This excitation mechanism differs from that in laser multiphoton dissociation,[2-10] in which the energy is poured into the parent molecule step by step; in each step the ligands are dissociated, and no substantial energy may be stored in the parent molecule. Excitation by He^m-impact also differs from photo-excitation at wavelengths corresponding to 19.8 eV[12] in that it is not restricted by optical selection rules. Therefore, two-electron-excited states can be produced in collision with the He^m atom.[19] These highly excited states, many of which are located in the vicinity of 19.8 eV, are likely to take part in the processes of dissociative excitation. An additional feature of the He^m-impact excitation is a steric effect, as observed typically in Penning ionization;[20,21] in molecules such as $Fe(CO)_5$ and $Fe(C_5H_5)_2$, the metal atom is "shielded" by the ligands so that the He^m atom cannot fully interact with the metal atom. In consequence, the ligands are first excited and then the energy is transferred to the metal atom.

Several studies of the reactions of $Fe(CO)_5$ with rare gas metastable atoms have been reported. Snyder et al. and Kobovitch et al. have observed the emission from the excited Fe atoms produced from $Fe(CO)_5$ by impact of an Ar^m beam.[17,18] The electronic-state distributions of the Fe atoms produced in the flowing-afterglow reactions of Ar^m,Ne^m, and He^m atom with $Fe(CO)_5$ have been analyzed in terms of a statistical model by Hartman et al.;[15,16] an "explosive dissociation mechanism" has been proposed, in which all the ligands dissociate at once.[16]

In the present work, the $He^m + Fe(CO)_5$ reaction is re-examined, and the electronic-state distribution is determined over many more electronic states than in the previous work.[16] The $He^m + Fe(C_5H_5)_2$ reaction, which has not been reported so far, is also studied, and the reactions of these two molecules are compared. A statistical model is developed for interpreting the electronic-state distributions obtained, from which the number of effective degrees of freedom of the heat bath is estimated. The dissociative states are also studied on the basis of a molecular-orbital correlation scheme, and it is found that the dissociative states are formed by electron rearrangement in the transient-excited states of the parent molecule primarily produced in the collision with He^m. The modes of the nuclear motions which contribute effectively to the heat bath are assigned by assuming that the energy partitioning between the Fe atom and the ligands occurs in this electron rearrangement accompanied by the vibrational excitation of the transient molecule.

EXPERIMENTAL SECTION

A flowing afterglow method was employed.[22] Helium gas, purified by passing through molecular sieve cooled at liquid nitrogen temperature, was let into a discharge region, where the He metastable atoms were generated by a microwave discharge (2.45 GHz, 100 W), and then admitted to a reaction chamber, which was evacuated by a mechanical booster pump (500 *l*/s). The pressure of He in the reaction region was 0.15-0.4 Torr. Charged particles produced simultaneously in the discharge were removed by a pair of grids, one of which was biased at -10 V.[22]

The target gas was introduced 15 cm downstream from the discharge region. Commercial $Fe(CO)_5$ (Alfa Ventron) and $Fe(C_5H_5)_2$ (Wako Chemicals) were used after degassing by several freeze-pump-thaw cycles. In the experiment on $Fe(CO)_5$, the pushing pressure of the sample gas, typically 5 Torr, was always monitored. On the other hand, in the case of $Fe(C_5H_5)_2$ a sample reservoir and an inlet pipe were heated to about 100°C so as to obtain a sufficient vapor pressure, about 10 Torr at 100°C.[23] The temperatures of the sample reservoir and the inlet pipe were always monitored so as to keep the pushing pressure constant. The pressure of the sample gas in the reaction region was several mTorr.

The emission from the reaction region was observed through a quartz window, dispersed by a 1 m monochromator (Spex 1704), and detected by a photomultiplier (Hamamatsu R585) and a photon-counting system. The spectral response of the monochromator and the detection system was calibrated by use of a standard lamp.

The emission spectra were measured in the range of 250-550 nm; many atomic lines of Fe(I) were observed, but no emission to be assigned to C_5H_5 or CO was observed. The emission spectra of Fe(I) in the range of 340-550 nm, measured with a resolution of 0.05-0.1 nm, were used for the analysis. A portion of the spectra of Fe(I) is shown in Figure 1.

The active species responsible for the production of the excited Fe atoms was identified as $He(2^3S_1)$ in the following way:[22] The emission intensities of the Fe(I) atomic lines were totally independent of the potential applied to the grids. Therefore, contributions of charged particles such as He^+ and thermal electrons to the reaction under consideration were found to be negligible. The dependence of the emission intensity on the He pressure was identical with that of the emission intensity of the $N_2^+(B\text{-}X)$ 0-0 band produced by Penning ionization, $He(2^3S_1)+N_2$. Therefore, it was confirmed that the excited Fe atoms were produced by a single collision with the $He(2^3S_1)$ atom.

ANALYSIS

A. Relative rates of formation

The relative rates of formation of the electronically excited states of the Fe atoms are calculated as follows. The number density of the Fe atom in the n-th electronic state, N_n, satisfies the relation

$$\frac{dN_n}{dt} = \sum_{m=n+1}^{\infty} A_{mn}N_m - \left(\sum_{l=1}^{n-1} A_{nl}\right)N_n + g_nR_n \ , \tag{1}$$

where A_{mn} is the Einstein A coefficient for the transition from the m-th to the n-th state, g_n is the multiplicity of the n-th state, and R_n is the rate of formation of the n-th state. The electronic states are numbered in the order of increasing energy. Under steady-state conditions, eq (1) leads to

$$R_n = K_n - L_n \ , \tag{2}$$

where

$$K_n = \left(\sum_{l=1}^{n-1} A_{nl}\right)N_n/g_n \tag{3}$$

and

$$L_n = \sum_{m=n+1}^{\infty} A_{mn}N_m/g_n \ . \tag{4}$$

Here, K_n corresponds to the total rate of formation of the n-th state, including contributions from cascades, and L_n represents the rate of formation of the n-th state due to cascading from all the higher states (see Figure 2). The relative values of the number densities, N_n and N_m, in eq (3) and (4) can be estimated from the relative emission intensities of the observed transitions; for example, the intensity of the transition from a given state n to a certain lower state k can be estimated by

$$I_{nk} = \alpha \nu_{nk} A_{nk} N_n \ , \tag{5}$$

where ν_{nk} represents the transition frequency and α is a constant.

The summation of A_n in eq (3) is taken over the transitions ranging 200-900 nm.[24] Possible errors caused by the neglect of the transitions outside this range are estimated in the following section. The summation in eq (4) is taken over those indices of m for which N_m's are obtained. It is found that the contributions of the cascades from upper electronic states to the state under consideration, L_n, do not appreciably influence the rates of formation, R_n, except for the three lower-lying excited states, z^7D, a^7F, and z^7P (the designation of the electronic states follows that in ref.25).

B. Random experimental errors in the rates of formation.

Random experimental errors are estimated from the fluctuations of the data obtained from several runs of the measurement and from the scatter in the rates of formation of a given state estimated independently from different transitions. The limits of error range from 10 to 50% of the rates of formation depending on the state of the Fe atom, as shown in Figure 3.

C. Systematic uncertainties inherent in the analysis.

The transitions with wavelengths longer than 900 nm are disregarded in the present analysis, but they are expected to have only a trivial influence on the summation of A_n in eq (3), because their A coefficients are generally smaller than those of the transitions in the UV-visible region. The A coefficients of these transitions disregarded can be estimated by assuming that the transition dipole matrix elements are constant for all the transitions and the A coefficient depends only on ν^3. Under the assumption that there are several transitions in the infrared region, the errors caused by the neglect of these transitions are estimated to be about 30% of the rate of formation obtained for all the states concerned.

The transitions with wavelengths shorter than 200 nm, which are also disregarded in the present analysis, can result in a more serious underestimate of the rate of formation of that state. Only the excited states above 6.2 eV (corresponding to the energy of 200 nm photon) are influenced by this source of systematic error. The *A* coefficients of these transitions with wavelengths shorter than 200 nm are generally larger than those of the transitions in the range of 200-900 nm, because the *A* coefficient is proportional to ν^3. Therefore, the neglect of the former transitions may have a strong influence on the summation: For example, if the sum in eq (3) is composed of the *A* coefficients for one transition at 170 nm and five other transitions near 400 nm but the transition at 170 nm is disregarded, the summation is underestimated to be about 1/70 of the true value. Therefore, the analysis of the state distribution to be discussed in the following sections is based only on the rates of formation of the states below 6.2 eV, which are free from uncertainties under consideration. Nevertheless, the rates of formation of the states above 6.2 eV are also in good agreement with those predicted by the statistical model. Therefore, the systematic error mentioned above for these states seems to be inessential.

RESULTS

A. Electronic-state distributions.

The quantum numbers of the observed excited states of Fe are $L=0-6$, $S=0-3$, and $J=1-7$, and their electron configurations are $3d^7 4s$, $3d^6 4s^2$, $3d^6 4s4p$, and $3d^6 4s5s$. The relative rates of formation of these excited states are plotted in Figure 3 as a function of their excitation energy. The rates decrease uniformly with the energy, and the energy dependence of the rate for $Fe(CO)_5$ is weaker than that for $Fe(C_5H_5)_2$. The rates of formation of the spin substates of the z^7F_J state depend on their total angular momentum, J, as shown in Figure 4, whereas the substates of all the other electronic states have essentially equal rates of formation. As shown in the next section, the J dependence of the z^7F_J state is explained as originating from collisional relaxation.

B. Collisional relaxation.

The relative rates of formation are found to be independent of the He pressure from 0.15 to 0.5 Torr. This finding indicates that the observed rates of formation are essentially free from collisional relaxation. The above statement is supported by the following estimation of the time scales: The cross section for collisional quenching of an excited Fe atom by the He atom is estimated from the quenching cross sections of $Hg(6^3P)$ by He[26] to be on the order of 0.1-1 Å^2. The relaxation time at 0.3 Torr is then estimated to be 1-10 μs. On the other hand, the radiative lifetimes of the observed excited states of Fe range 1-50 ns, and hence, almost all the excited states are essentially free from collisional quenching under the present experimental conditions. The three lower-lying states, z^7D, z^7F, and z^7P, are the exceptions, because they have lifetimes of 1-70 μs.[24] However, the effect of collisional quenching on the rates of formation of these states is estimated to be inessential in the following way: When the He pressure is varied from 0.15 to 0.5 Torr, the change in the rates of formation of these three lower-lying states is found to be within the experimental fluctuation, which is about 10% of the rates of formation. If one assumes that this change is ascribed to the collisional quenching, the collision-free rate of formation obtained by extrapolation to the zero-pressure limit amounts to about 1.04 times the rate of formation estimated at 0.15 Torr. Therefore, the effect of collisional quenching on the rates of formation of these three lower-lying states, z^7D, z^7F, and z^7P, is negligible.

On the other hand, the cross sections for relaxation within the spin substates are expected to be several orders of magnitude larger because of the exponential-gap law.[27] In a beam experiment of the $Ar^m + Fe(CO)_5$

reaction[17,18] the rate of formation is found to be independent of J for the z^7F_J state, whereas in an experiment of Ar flowing afterglow at an Ar pressure of 2 Torr[16] the rate is found to increase rapidly with J. Therefore, relaxation among the spin substates can cause Jdependence, and the J dependence of the rates of formation of the z^7F_J states observed in the present study can be ascribed to the collisional relaxation within the spin substates. Nevertheless, this relaxation does not alter the rate of formation averaged over the spin substates. Therefore, the analysis of the state distribution discussed in the following sections is based on the rate of formation of the z^7F_J state averated over the spin substates. However, this type of relaxation is considered to be negligible for any other electronic states, because their rates of formation are found to be independent of J.

DISCUSSION

A. Statistical model.

The gradual and monotonic decrease in the rates of formation with the energy of the excited Fe atom indicates that the state distributions are explicable by a statistical model. The analysis is based on the following model: The excess energy of the reaction is distributed among the motions of the electrons in the Fe atom and the vibrational motions of the parent molecule. In the dissociation limit the normal modes of the parent molecule are connected to the translational, rotational, and vibrational motions of the ligands. Therefore, these normal modes of the parent molecule can be grouped into the translation-like, rotation-like, and vibration-like modes. The translation-like modes correspond to the vibrational modes composed mainly of the motions of the centers of mass of the fragments. The vibration-like modes correspond to the vibrational modes of the fragments. The remaining modes of the parent molecule are the rotation-like modes. The excess energy is assumed to be distributed, besides the electronic energy of the Fe atom, among the translation-like, rotation-like, and vibration-like modes, which have N_t, N_r, and N_v effective degrees of freedom, respectively; these modes act as a heat bath attached to the Fe atom. If the Fe atom has an electronic energy of E, the heat bath shares the energy of $E_{ex}-E$, where E_{ex} is the excess energy defined by

$$\begin{aligned} E_{ex} = &\text{(excitation energy of He(}2^3\text{S}_1\text{), 19.8 eV)} \\ &-\text{(energy required separate all the ligands)} \\ &-\text{(electronic energy of theseparated ligands)}. \end{aligned} \tag{6}$$

If one assumes that all the final quantum states are equally probable, the probability, $P(E)$, of producing the Fe atom which has an energy E is proportional to the density of states of the heat bath at $E_{ex}-E$. By use of the rigid rotor-harmonic oscillator approximation, $P(E)$ is given by[28,29]

$$P(E) = \text{const.} \times (E_{ex}-E)^n \ , \tag{7}$$

$$n = ½(N_t+N_r+s)+N_v-1 \ , \tag{8}$$

where $s=2$ if the centers of mass of the fragments have a linear configuration in the parent molecule before the dissociation, and $s=3$ otherwise. The parameter s originates from the degree of freedom of the orientation of the parent molecule, which is unspecified in the present experiment.

B. Analysis of P(E).

The parameters, E_{ex} and n, are determined by fitting $P(E)$ to the experimental distributions. In this fitting procedure, the curvature of $P(E)$ is adjusted by choosing E_{ex} from the possible excess energies of the energetically accessible processes listed in Table I, and the rate of decrease in $P(E)$ is adjusted by varying n. The best-fit curves are shown in Figure 3, and the values of E_{ex} and n which give the best-fit curves are listed in Table II.

In the case of $Fe(CO)_5$, the value of E_{ex} is determined uniquely to be 7.8

eV. If E_{ex} is set equal to 13.8 eV, the graph of $P(E)$ becomes a straight line irrespective of the value of n, and $P(E)$ cannot be fitted to the experimental state distribution which has a certain curvature. On the other hand, if E_{ex} is set equal to 6.9 eV or smaller, the curvature of $P(E)$ is too large for any value of n to obtain a good fitting. Therefore, the value of n is determined by adjusting the rate of decrease in $P(E)$ after E_{ex} is fixed at 7.8 eV.

In the case of $Fe(C_5H_5)_2$, the graph of the experimental state distribution is a straight line, and $P(E)$ can be fitted equally well for E_{ex} ranging 13.4-8.0 eV, beyond which the curvature is too large to be acceptable. The value of n is determined by adjusting the rate of decrease in $P(E)$, which is insensitive to the value of E_{ex} in the range of 13.4-8.0 eV.

From the value of E_{ex} obtained, the electronic states of the separated ligands can be identified. On the other hand, the parameter n provides information on the degrees of freedom of the heat bath involved in the dissociation.

C. Estimation of the effective degrees of freedom.

The values of N_t, N_r, and N_v are estimated from eq (8) by use of the estimated value of n under the following constraints:

(1) N_t, N_r, and N_v do not exceed the available degrees of freedom, N_t^0, N_r^0, and N_v^0, respectively (see Appendix).

(2) N_t is non-zero, i.e., it is assumed that the translational motions of the dissociating fragments are always fully effective as the heat bath, because the translational motions are the motions along the dissociation coordinates to which the excess energy must be partitioned in order that the dissociation takes place.

(3) Dissociation forming N_f independent fragments involves $3N_f-6$ translational degrees of freedom (or $3N_f-5$, if the centers of mass of the

fragments have a linear configuration in the parent molecule), because the degrees of freedom of the relative motions of N_f particles are $3N_f-6$ (or $3N_f-5$). Therefore, it follows that

$$N_t=3N_f-6 \text{ (nonlinear configuration),}$$

or

$$N_t=3N_f-5 \text{ (linear configuration).} \tag{9}$$

By substitution of N_t with N_f, eq (8) is expressed as

$$n=½(3N_f+N_r-3)+N_v-1 \; . \tag{10}$$

The dissociation mechanism can be determined from N_f. The efficiency of the heat bath, η, can be calculated by

$$\eta=(N_t+N_r+N_v)/(N_t^0+N_r^0+N_v^0) \; . \tag{11}$$

The modes which contribute effectively to the heat bath are those modes which are likely to share the excess energy with the Fe atom. Therefore, these modes should interact strongly with the motions of the electrons around the Fe atom in the dissociative states. In order to assign the effective modes, one needs information on the vibronic interaction in the dissociative states.

D. Dissociative states and vibrobic interaction.

When a target molecule collides with He^m, the target molecule is excited by promotion of either one or two electrons from the occupied orbital(s); these orbitals should have sufficient overlaps with the 1s orbitals of He^m in order that the excitation takes place with an appreciable cross section.[20,21] This criterion, along with the consideration of the energetics, enables the assignment of the electron configurations of the primary excited states.

Since various electronic states of Fe are produced in the reaction under consideration, the primary excited states should decay into many dissociative states, each of which correlates with a different electronic state of Fe. The energy partitioning between the Fe atom and the nuclear motions occurs in this non-radiative electronic transition accompanied by the vibrational excitation of the transient molecule. This electronic transition, in other words electron rearrangement, can be traced by considering the correlation between the electron configurations of the primary excited state and the final products. Then one can predict which vibrational modes are likely to be excited.

The probability amplitude, T_{fi}, for this electron rearrangement with vibrational excitation is expressed as

$$T_{\mathrm{fi}} = <\psi_{\mathrm{f}}(\mathbf{r},\mathbf{Q})\chi_{\mathrm{f}}(\mathbf{Q})|V(\mathbf{r})|\psi_{\mathrm{i}}(\mathbf{r},\mathbf{Q})\chi_{\mathrm{i}}(\mathbf{Q})> \tag{12}$$

where ψ and χ are the electronic and vibrational wave functions, respectively, $\mathbf{r}$ is the electron coordinate, $\mathbf{Q}$ is the normal coordinate, and $V(\mathbf{r})$ represents the Coulombic interaction among the electrons. After integration with respect to $\mathbf{r}$, one can rewrite eq (12) as

$$T_{\mathrm{fi}} = <\chi_{\mathrm{f}}(\mathbf{Q})|\bar{V}(\mathbf{Q})|\chi_{\mathrm{i}}(\mathbf{Q})>, \tag{13}$$

where $\bar{V}(\mathbf{Q})$, the matrix element of the electron correlation for fixed $\mathbf{Q}$, is defined by

$$\bar{V}(\mathbf{Q}) = <\psi_{\mathrm{f}}(\mathbf{r},\mathbf{Q})|V(\mathbf{r})|\psi_{\mathrm{i}}(\mathbf{r},\mathbf{Q})>. \tag{14}$$

The Taylor expansion of $\bar{V}(\mathbf{Q})$ about the equilibrium nuclear coordinates leads to

$$T_{\mathrm{fi}} = \bar{V}_0<\chi_{\mathrm{f}}|\chi_{\mathrm{i}}> + \sum_s\left(\frac{\partial\bar{V}}{\partial Q_s}\right)_0<\chi_{\mathrm{f}}|Q_s|\chi_{\mathrm{i}}> + \cdots . \tag{15}$$

The second term represents the vibrational excitation induced by the electron rearrangement; the vibrational modes that have large $(\partial\bar{V}/\partial Q_s)_0$ values are likely to participate in the energy partitioning under consideration. Expressing the ψ's by the products of MO's, one can reduce $(\partial\bar{V}/\partial Q_s)_0$ to the derivative of the matrix element represented in terms of the bases of an individual molecular orbital, ϕ. Since V is the two-electron operator, the matrix element in eq. (14) can be represented in terms of the four molecular orbitals which are involved in the electron rearrangement. Therefore, it follows that

$$(\frac{\partial \bar{V}}{\partial Q_s})_0 = \frac{\partial}{\partial Q_s} <\psi_f|V|\psi_i>$$
$$= \frac{\partial}{\partial Q_s} <\phi_\lambda\phi_\mu|V|\phi_\rho\phi_\sigma>. \quad (16)$$

From eq. (16) with given electron configurations before and after the electron rearrangement, one can predict which modes have large $(\partial\bar{V}/\partial Q_s)_0$ values. Such a model calculation is applied to the formation of the excited Fe atoms from $Fe(CO)_5$ and $Fe(C_5H_5)_2$.

E. Reaction of He^m with Fe(CO)₅.

E.1 Analysis of the electronic-state distribution.

The energetically accessible processes which lead to the formation of the Fe atom are listed in Table I. By choosing E_{ex} from these values, and simultaneously varying n, the $P(E)$ defined in eq. (7) is fitted to the experimental state distribution (see section B.). The value of E_{ex} is uniquely determined to be 7.8 eV (see Table II). Therefore, the most probable process leading to the formation of excited Fe atoms is estimated to be

$$He^m + Fe(CO)_5 \rightarrow He + Fe^* + CO(a^3\Pi) + 4CO(X^1\Sigma^+). \quad (17)$$

On the other hand, the best-fit value of n defined in eq. (8) is 2 ± 0.5 (see Table II). Among the several possible combinations of N_f, N_r, and N_v which satisfy eq. (10), N_f is restricted to 2 or 3 because $N_f \leq 3$ from eq.(10) for $n=2$ and because $N_f \geq 2$ by definition, and hence, N_t has to be either 1, 3 or 4 from eq.(9). Corresponding to these two possibilities for N_f, one can consider two possible mechanisms: mechanism (1), where $N_f=2$, and mechanism (2), where $N_f=3$ (see Table III).

In mechanism (1), two independent fragments can be assigned to the Fe atom and a group of five CO ligands. This indicates that all the CO molecules explode outwards with the same velocity, i.e., they dissociate along the normal coordinate of the Fe-C breathing vibration. Several combinations of N_r and N_v are possible in this case (see Table III).

In mechanism (2), two fragments besides the Fe atom are involved. One possibility is as follows: The translational motion of the CO($a^3\Pi$) molecule and those of the explosive dissociation of the four CO($X^1\Sigma^+$) molecules are involved in the dissociation. In this case, where $N_f=3$, N_v and N_r are restricted to be zero according to eq.(10), i.e., the rotation-like and vibration-like modes are ineffective as the heat bath.

Both mechanisms involve explosive dissociation, and only a small number of the degrees of freedom are effective as the heat bath. The efficiency, η, ranges from 11% to 21%, as shown in Table III.

The present conclusion is essentially consistent with that obtained by Hartman et al.[16] They concluded a completely explosive dissociation mechanism, where $N_f=2$ and $N_r=N_v=0$, and hence, $n=0.5$ (see eq.(10)), for reactions of Ar^m, Ne^m, and He^m, with $Fe(CO)_5$ assuming that all the CO molecules were produced in the ground state $X^1\Sigma^+$. In the present work, the rates of formation are obtained over many more electronic states than in the previous work,[16] and more detailed information on E_{ex} and n is obtained: In summary, one of the five CO molecules is found to be produced in the $a^3\Pi$ excited state, and it is also found that a few degrees of freedom, besides those of the explosive dissociation, can take part in the energy partitioning.

E.2 Dissociative states and vibronic interaction.

The reaction under consideration does not involve ionization because of its energetics (see Table I). Therefore, if one-electron promotion is assumed, the electron in question must be promoted from one of the orbitals which have ionization potentials higher than 19.8 eV (the excitation energy of He^m). As mentioned in section D, this orbital should have a sufficient overlap with the 1s orbital of He^m. The orbitals which satisfy the above two criteria are the 4σ-like orbitals which have high electron densities on the O-atom side of CO (see Figure 5). The primary excited state is assigned to a Rydberg state with an electron configuration of $(4\sigma-\text{like})^{-1}(\text{Ryd})^1$, because the energetics requires that the primary excited state is one of the Rydberg states.

Since the 4σ-like orbitals are nonbonding orbitals localized on the CO ligands,[30,31] a hole in the 4σ-like orbital remains in one of the CO molecules when the dissociation proceeds, and an electronically excited CO molecule with a hole in the 4σ orbital is formed. However, formation of $\text{CO}^*((4\sigma)^{-1})$ is unacceptable because of its energetics. Furthermore, an analysis of the state distribution (section E.1) indicates that one of the CO molecules is excited to the $a^3\Pi$ state, which has the electron configuration of $(5\sigma)^{-1}(2\pi)^1$.[32] The formation of $\text{CO}(a^3\Pi)$ from Fe(CO)_5 with a hole in the 4σ-like orbital can be explained by assuming the following electron rearrangement: One electron in the 5σ-like (or 3d-like) orbital fills the hole in the 4σ-like orbital, and simultaneously one electron in the 3d-like (or 5σ-like) orbital is promoted to a Rydberg orbital (see Figure 6). In consequence, a two-electron-excited state with holes in the 5σ-like and 3d-like orbitals is formed. Dissociation from this state leads to the formation of an electronically excited Fe atom, one $\text{CO}(a^3\Pi)$ and four $\text{CO}(X^1\Sigma^+)$ molecules.

The quantity $(\partial \bar{V}/\partial Q_s)_0$ in eq.(16) corresponding to the above electron rearrangement is expressed as

$$\left(\frac{\partial \bar{V}}{\partial Q_s}\right)_0 = \frac{\partial}{\partial Q_s} \langle \phi_{\text{Ryd}}\phi_{4\sigma}|V|\phi_{5\sigma}\phi_{3\text{d}}\rangle , \tag{18}$$

where ϕ_{Ryd} represents a Rydberg orbital, $\phi_{4\sigma}$ a 4σ-like orbital, etc. Since $\phi_{4\sigma}$, $\phi_{5\sigma}$, and $\phi_{3\text{d}}$ orbitals are mainly localized on the O, C, and Fe atoms, respectively, the Fe-C and C-O stretching vibrations are expected to influence the matrix element strongly. Therefore, the normal modes which involve the Fe-C and/or C-O stretching motions, i.e., the dissociative motion, which correspond to four translation-like modes, and the stretching vibrations of the five CO ligands, which correspond to five vibration-like modes, are likely to act as the heat bath. On the other hand, the normal modes which are mainly composed of the Fe-C-O bending motions and the C-Fe-C bending motions are expected to be ineffective as the heat bath; these modes correspond to all of the rotation-like modes and four translation-like modes.

The present discussion is essentially consistent with the results obtained in section E.1: The findng in Table III that only one half, or even less, of the available translation-like degrees of freedom is effective as the heat bath can be explained by the missing contributions from the available translation-like modes of the C-Fe-C bending motions. The present discussion also predicts correctly that the number of effective rotation-like degrees of freedom is very small. As for the vibration-like modes, however, many fewer degrees of freedom than those predicted by the present analysis are actually effective.

F. Reaction of He^m *with* $Fe(C_5H_5)_2$.

F.1 Analysis of the electronic-state distribution

By an analysis of the state distribution, the value of E_{ex} is estimated to range 8.0-13.4 eV. This energy corresponds to a process producing one C_5H_5 in the ground state and the other C_5H_5 in either an excited state with energy less than 5 eV or the ground state (see Table I):

$$He^m + Fe(C_5H_5)_2 \rightarrow He + Fe^* + C_5H_5 + C_5H_5(^*), \qquad (19)$$

where $C_5H_5(^*)$ represents a C_5H_5 radical in an electronic state with energy of 0-5 eV.

The value of n is estimated to be 15 ± 3 (see Table II). Since $N_t^0=3$ (see Table III), N_t is at most 3. From eq.(9) and the constraint that $N_t\neq0$, it follows that N_t is restricted to be either 1 or 3. On the other hand, N_r should be equal to or less than 3 because $N_r^0=3$ (see Table III). In consequence, the value of N_v is limited in the range of 12-15 because of eq.(8) with $n=15$ (see Table III). This means that effectively 6-8 vibrational modes per one C_5H_5 radical act as the heat bath. The efficiency, η, given in Table III is found to be higher than that for $Fe(CO)_5$; in other words, the $(C_5H_5)_2$ ligands provide a more efficient heat bath than the $(CO)_5$ ligands.

F.2 Dissociative states and vibronic interaction.

The energetics analysis of the state distribution (Table I) indicates that the reaction under consideration does not involve ionization. Therefore, if one-electron promotion occurs the molecular orbital involved should have an ionization potential higher than the energy of He^m, 19.8 eV. The orbitals which satisfy this requirement are the σ orbitals (see Figure 7), which mainly consist of the 2s orbitals of the C atoms.[33] However, the probability of the promotion from a σ orbital is expected to be small because the σ orbitals do not overlap sufficiently with the 1s orbital of He^m. On the other hand, two-electron promotion from the π orbitals is expected to have an appreciable cross section because the π orbitals have larger overlaps, in which case the energy required to promote the two electrons should be less than the excitation energy, 19.8 eV: The states to which the molecule is excited primarily are assigned to the Rydberg states with electron configurations of $(\pi)^{-1}(\pi')^{-1}(Ryd)^2$, where π and π' orbital belong to the same C_5H_5 ligand.

The excited C_5H_5 radical produced in eq.(19) should have one hole in a π orbital because its excitation energy is small (less than 5 eV). The π-like orbital of $Fe(C_5H_5)_2$ is mainly composed of the π orbitals of the C_5H_5 ligands, and hence, the holes in the π-like orbitals are likely to remain in the C_5H_5 radical after the dissociation. Therefore, one of the two holes in the π-like orbitals should be filled by an electron of the Fe atom when the dissociatiion proceeds. Namely, electron transfer from Fe to C_5H_5 takes place. The other possibility of the product states of the C_5H_5 radicals, i.e., formation of two ground-state C_5H_5 radicals indicates that two electrons are transferred from Fe to the π orbitals of the ligand.

The quantity $(\partial\bar{V}/\partial Q_s)_0$, given in eq.(16), corresponding to the above two processes of electron transfer is given by

$$(\frac{\partial\bar{V}}{\partial Q_s})_0=\frac{\partial}{\partial Q_s}<\phi_\pi|V|\phi_{3d}> \quad \text{or} \tag{20}$$

$$=\frac{\partial}{\partial Q_s}<\phi_\pi\phi_{\pi'}|V|\phi_{3d}\phi_{3d'}>. \tag{21}$$

The Fe$-(C_5H_5)$ stretching motions are expected to have large $(\partial\bar{V}/\partial Q_s)_0$ values, because the overlap between a π orbital and a 3d orbital is strongly influenced by these motions. The skeletal vibrations of C_5H_5 are also expected to have large $(\partial\bar{V}/\partial Q_s)_0$ values, because the skeletal vibrations cause a deformation of the π-electron cloud. Therefore, the dissociative motion and the skeletal vibrations of the C_5H_5 ligands are expected to be effective as the heat bath. Since one C_5H_5 ligand has 9 skeletal modes, the present discussion explains why 6-8 vibrational modes per one C_5H_5 ligand act as the heat bath.

APPENDIX : *Evaluation of the available degrees of freedom for the heat bath*

The upper limit of the degrees of freedom of the heat bath is equal to the number of the normal modes of the parent molecule. In practice, however, not all of these degrees of freedom can contribute to the heat bath even in the limit of completely statistical partitioning of the excess energy, because the excitation of some degrees of freedom violates the conservation of the total angular momentum. When one considers the conservation of the total angular momentum, it is necessary to take account of the coupling of the angular momenta. The initial total angular momentum, which is composed of the rotational angular momentum of the parent molecule and the orbital angular momentum of the incoming He^m atom, should be equal to the final total angular momentum, which is composed of the angular momenta of the motions of the fragments, the electronic angular momentum of the excited Fe atom, and the orbital angular momentum of the outgoing He atom.

The angular momenta carried by the rotation of the parent molecule and the motion of the helium atom are small (at most several tens of $\hbar$) because these motions are thermal motions. The electronic angular momentum of the excited Fe atom produced in the dissociation is found to range from $\hbar$ to $7\hbar$ (see Results A). On the other hand, the angular momenta of the translational and rotational motions of the fragments can be much larger than those mentioned above, because the fragments may have translational energies of several eV and may also be rotationally excited, whereas the vibrational angular momenta of the fragments are on the order of $\hbar$ even if they are vibrationally excited.[34] Such large angular momenta of the translational and rotational motions of the fragments cannot be cancelled by coupling with any other angular momenta within the final system of the fragments. Therefore, it can be assumed that the translational and rotational degrees of freedom which have angular momenta do not contribute significantly to the heat bath. Following this assumption, the available translation-like and rotational-like degrees of freedom, N_t^0 and N_r^0, are here defined as those translation-like and rotation-like degrees of freedom which have no angular momenta, respectively. On the other hand, the available vibration-like degrees of freedom, N_v^0, are defined as the total vibration-like degrees of freedom. In order to obtain N_t^0 and N_r^0, one needs to assign which degrees of freedom have angular momenta.

A degenerate vibrational mode of the parent molecule which belongs to either translation-like or rotation-like mode may have a vibrational angular momentum, which can be transmitted to the angular momenta of the translational or rotational motions of the separeted ligands as the dissociation proceeds. Therefore, the degenerate translation-like and rotation-like modes which have angular momenta are, under the assumption stated above, ineffective as the heat bath. In other words, for one doubly degenerate mode belonging to the translation-like or rotation-like modes, only the vibrational mode with zero vibrational angular momentum, $l=0$, is effective as the heat bath, so that such a degenerate mode should be counted as one (instead of two) available degree of freedom.

The above prescription is applied to $Fe(CO)_5$ and $Fe(C_5H_5)_2$. The symmetry species of the normal modes of the parent molecules, $Fe(CO)_5$ and $Fe(C_5H_5)_2$, listed in Table IV, are grouped into the translation-like, rotation-like, and vibration-like modes. The available degrees of freedom estimated on the basis of this table are given in table III.

References

(1) Thrush, B. A. *Nature* **1956,** *178,* 155.

(2) Leutwyler, S.; Even, U.; Jortner, J. *Chem. Phys. Lett.* **1980,** *74,* 11.

(3) Leutwyler, S.; Even, U.; Jortner, J. *J. Phys. Chem.* **1981,** *85,* 3026.

(4) Leutwyler, S.; Even, U.; Jortner, J. *Chem. Phys.* **1981,** *58,* 409.

(5) Engelking, P. C. *Chem. Phys. Lett.* **1980,** *74,* 207.

(6) Duncan, M. A.; Dietz, T. G.; Smalley, R. E. *Chem. Phys.* **1979,** *44,* 415.

(7) Whetten, R. L.; Fu, K.-J.; Grant, E. R. *J. Chem. Phys.* **1983,** *79,* 4899.

(8) Yardley, J. T.; Gitlin, B.; Nathanson, G.; Rosan, A. M. *J. Chem. Phys.* **1981,** *74,* 370.

(9) Nagano, Y.; Achiba, Y.; Sato, K.; Kimura, K. *Chem. Phys. Lett.* **1982,** *93,* 510.

(10) Majima, T.; Tashiro, H.; Midorikawa, K.; Takami, M. *Chem. Phys. Lett.* **1985,** *121,* 65.

(11) Karny, Z.; Naaman, R.; Zare, R. N. *Chem. Phys. Lett.* **1978,** *59,* 33.

(12) Horak, D. V.; Winn, J. S. *J. Phys. Chem.* **1983,** *87,* 265.

(13) Hale, B. C.; Winn, J. S. *J. Chem. Phys.* **1984,** *81,* 1050.

(14) Bronnen, W. R.; Kistiakowsky, G. B. *J. Chem. Phys.* **1966,** *44,* 2695.

(15) Hartman, D. C.; Winn, J. S. *J. Chem. Phys.* **1978,** *68,* 2990.

(16) Hartman, D. C.; Hollingsworth, W. E.; Winn, J. S. *J. Chem. Phys.* **1980,** *72,* 833.

(17) Snyder, H. L.; Parr, T. P.; Parr, D. H.; Smith, B. T.; Martin, R. M. *Chem. Phys. Lett.* **1980,** *73,* 487.

(18) Kobovitsh, J.; Krenos, J. *J. Chem. Phys.* **1981,** *74,* 2662.

(19) Chapter 4.

(20) Harada, Y.; Ohno, K.; Mutoh, H. *J. Chem. Phys.* **1983,** *79,* 3251.

(21) Munakata, T.; Harada, Y.; Ohno, K.; Kuchitsu, K. *Chem. Phys. Lett.* **1981,** *84,* 6.

(22) Ozaki, Y.; Kondow, T.; Kuchitsu, K. *Chem. Phys.* **1986,** *109,* 345.

(23) Polino, M.; Tomassetti, M.; Picacente, V.; D'Ascenzo, G. *Thermochem. Acta* **1981,** *44,* 89.

(24) Corliss, C. H.; Bozman, W. R. *Natl. Bur. Stand. Monograph* **1962,** *53.*

(25) Moore, C. E. *Natl. Stand. Ref. Data Ser. Natl. Bur. Stand.* **1971,** *35.*

(26) Krause, L. Adv. Chem. Phys. **1975,** *28,* 267.

(27) Levine, R. D.; Bernstein, R. B. *Molecular Reaction Dynamics*; Oxford Univ. Press, 1974.

(28) Levine, R. D. *Ann. Rev. Phys. Chem.* **1978,** *29,* 59.

(29) Berry, M. J. *Chem. Phys. Lett.* **1974,** *29,* 323.

(30) Barends, E. J.; Oudshoorn, Ch.; Oskam, A. *J. Electron Spectrosc. Relat. Phenom.* **1975,** *6,* 259.

(31) Barends E. J.; Ros, P. *Mol. Phys.* **1975,** *30,* 1735.

(32) Herzberg, G. *Spectra of Diatomic Molecules*; Van Nostrand Reinhold: New York, 1945.

(33) Canletti, C.; Green, J. C.; Kelly, M. R.; Powell, P.; van Tilborg, J. *J. Electron Spectrosc. Relat. Phenom.* **1980,** *19,* 327.

(34) Herzberg, G. *Infrared* and *Raman Spectra of Polyatomic Molecules*; Van Nostrand Reinhold: New York, 1945.

(35) Cotton, F. A.; Fischer, A. K.; Wilkinson, G. *J. Am. Chem. Soc.* **1958,** *81,* 800.

(36) Wilkinson, G.; Pauson, P. L.; Cotton, F. A. *J. Am. Chem. Soc.* **1954,**

76, 1970.

(37) Huber, K. P.; Herzberg, G. *Constants of Diatomic Molecules*; Van Nostrand: New York, 1979.

(38) Harrison, A. G.; Honner, L. R.; Dauben Jr., H. J.; Lossing, F. P. *J. Am. Chem. Soc.* **1960,** *82,* 5593.

(39) Haaland, A. *Acc. Chem. Res.* **1979,** *12,* 415.

(40) Rabalais, J. W.; Werme, L. O.; Bergmark, T.; Karlsson, L.; Hussain, M.; Siegbahn, K. *J. Chem. Phys.* **1972,** *57,* 1185.

(41) Armstrong, D. R.; Fortune, R.; Perkins, P. G. *J. Organomet. Chem.* **1976,** *111,* 197.

(42) Coutiere, M.-M.; Demuynck, J.; Veillard, A. *Theoret. Chim. Acta* **1972,** *27,* 281.

TABLE I

Energetically accessible processes

Process[1]	E_{ex}/eV^{b}
$He(2^3S_1) + Fe(CO)_5 \rightarrow$	
$He + Fe + 5CO(X^1\Sigma^+)$	13.8
$He + Fe + 4CO(X^1\Sigma^+) + CO(a^3\Pi)$	7.8
$He + Fe + 4CO(X^1\Sigma^+) + CO(a'^3\Sigma^+)$	6.9
$He + Fe + 4CO(X^1\Sigma^+) + CO(d^3\Pi)$	6.1
$He + Fe + 4CO(X^1\Sigma^+) + CO(A^1\Pi)$	5.5
$He + Fe + 4CO(X^1\Sigma^+) + CO(b^3\Sigma^+)$	3.4
$He(2^3S_1) + Fe(C_5H_5)_2 \rightarrow$	
$He + Fe + 2C_5H_5$	13.4
$He + Fe + C_5H_5 + C_5H_5{}^{*}$ [c]	9.7
$He + Fe + C_5H_5 + C_5H_5^+$	4.8

a) A cyclopentadienyl radical and its ion in the ground state are represented by C_5H_5 and $C_5H_5^+$, respectively, and $C_5H_5{}^*$ represents a cyclopentadienyl radical in the S_1 state.

b) Excess energy of the reaction defined by

(excitation energy of $He(2^3S_1)$, 19.8 eV)
−(energy required to separate all the ligands)
−(electronic energy of the separated ligands).

The values of the dissociation energy of $Fe(CO)_5$ and $Fe(C_5H_5)_2$ are taken from refs. 35 and 36, respectively. For the excitation energies of CO, those listed in ref. 37 are used. The energy value of the S_1 state of C_5H_5 is taken from ref. 1, and the ionization potential of C_5H_5 is taken from ref. 38.

c) This value corresponds to the formation of C_5H_5 in the S_1 state.[1] Excitation energies for no higher excited states have been reported.

TABLE II

Parameters for the statistical model[a]

	E_{ex}/eV	n
$Fe(CO)_5$	7.8	2 ± 0.5[c]
$Fe(C_5H_5)_2$	8.0−13.4[b]	15.3 ± 3[c]

a) The values of E_{ex} and n which provide the best fit to the experimental state-distributions. In the fitting procedure the values of E_{ex} is chosen from the excess energies of the energetically accessible processes listed in Table I, while the value of n is allowed to take any positive number.

b) The calculated state-distribution is not sensitive to E_{ex}, and therefore, the value of E_{ex} cannot be determined uniquely in the range indicated.

c) The uncertainty estimated from the limiting values of n beyond which the fit apparently breaks down.

TABLE III

The number of the degrees of freedom effective as the heat bath

$Fe(CO)_5$

	N_i^0 [a]	N_i(i=t,r,v,total)[b]	
	(i=t,r,v,total)	mechanism (1)	mechanism (2)
trans.-like	8	1	3,4
rot.-like	6	0-2	0
vib.-like	5	0-2	0
total	19	2−4[d]	3,4
efficiency[c]		11-21%	16-21%

$Fe(C_5H_5)_2$

	N_i^0 [a]	N_i [b]
	(i=t,r,v,total)	(i=t,r,v,total)
trans.-like	3	1,3
rot.-like	3	0-3
vib.-like	48	12-15
total	54	16−18[d]
efficiency[c]		28-33%

a) Available degrees of freedom N_t^0, N_r^0, N_v^0, and N_{total}^0 ($=N_t^0+N_r^0+N_v^0$), determined by the prescription described in Appendix.

b) Effective degrees of freedom, N_t, N_r, N_v, and N_{total} ($=N_t+N_r+N_v$), determined so that they satisfy eq.(8) when the value of n given in table 2 and the constraints on the translation-like degree of freedom, N_t, i.e., $N_t=3N_f-6$ (or

$3N_f-5$) are used. In the case of $Fe(CO)_5$, two mechanisms can be considered corresponding to two possible values of N_t. See Discussion E.1.

c) Efficiency of the heat bath defined by eq.(11).

d) There is a correlation among N_t, N_r, and N_v because of eq.(8), and this correlation is taken into account in the determination of N_{total}. Therefore, the upper and lower limits of N_{total} are not equal to the sum of the upper and lower limits of the N_t, N_r, and N_v listed.

TABLE IV

Classification of the vibrational modes of the parent molecule

$Fe(CO)_5/D_{3h}$					
parent molecule[a]	$4A'_1$	$+A'_2$	$+6E'$	$+4A''_2$	$+3E''$
trans.-like[b]	$2A'_1$		$+3E'$	$+2A''_2$	$+E''$
rot.-like		A'_2	$+2E'$	A''_2	$+2E''$
vib.-like	$2A'_1$		$+E'$	$+A''_2$	

$Fe(C_5H_5)_2/D_{5h}$ [c]						
parent molecule[a]	$4A'_1$	$+A'_2+6E'_1$	$+6E'_2+2A''_1$	$+4A''_2$	$+5E''_1$	$+6E''_2$
trans.-like[b]	A'_1	$+E'_1$		$+A''_2$		
rot.-like		E'_1	$+A''_1$		$+E''_1$	
vib.-like	$3A'_1$	$+A'_2+4E'_1$	$+6E'_2+A''_1$	$+3A''_2$	$+4E''_1$	$+6E''_2$

a) Symmetry species of the vibrational modes of the parent molecule.

b) The vibrational modes of the parent molecule are grouped into the translation-, rotation-, and vibration-like modes.

c) Ref. 39.

Figure Captions

Figure 1: A portion of the emission spectrum of the Fe atom obtained in the reaction of a) $He^m + Fe(CO)_5$ and b) $He^m + Fe(C_5H_5)_2$. The helium pressure was 0.2 Torr, and the resolution was 0.05 nm.

Figure 2: Schematic diagram for the analysis of cascades. The total rate of formation of the n-th state including contributions from cascades is determined from the emission intensities of the transitions from the n-th state to the k-th states, I_{nk}, and the radiative lifetimes of the n-th state, which are estimated from the sum of the transition probabilities of the transitions from the n-th state to the l-th states. The contributions of the cascades from the m-th states are evaluated from the probabilities of the transitions from the m-th states to the n-th state and the population of the m-th states, which are determined from the emission intensities of the transitions from the m-th states to the j-th states, I_{mj}.

Figure 3: Relative rates of formation, R_n, of the excited Fe atoms plotted against their electronic energies, E_n. The rates of formation are normalized against the rate of formation of the z^7F_5 state. The closed and open circles represent the data for $Fe(CO)_5$ and $Fe(C_5H_5)_2$, respectively. The rates of formation of the state above 6.2 eV (indicated by a vertical broken line) have large uncertainties (see Analysis C). The solid curves represent the best-fit curves calculated on the basis of the statistical model (see Discussion A and B).

Figure 4: Plot of the relative rates of formation of the spin substates of the z^7F_J and the z^5F_J states against their total angular momentum J. The rates of formation are normalized against the rate of formation of the z^7F_5 state.

Figure 5: Schematic diagram of the molecular orbital correlations between

$Fe(CO)_5$ and Fe + 5CO.[30,31] Thick correlation lines indicate principal components of the relevant molecular orbitals.

Figure 6: Changes in the electron configurations of $Fe(CO)_5$ during the dissociative excitation. The left column represents the initial state. The middle column represents the primary excited state with a hole in a 4σ-like orbital, and dissociation from this state gives CO with a hole in the 4σ orbital. The right column represents the dissociative state after the electron rearrangement, and dissociation from this state gives one CO molecule with a configuration of $(5\sigma)^{-1}(2\pi)^1$.

Figure 7: Schematic diagram of the molecular orbital correlations between $Fe(C_5H_5)_2$ and Fe + $2C_5H_5$.[40-42] Thick correlation lines indicate principal components of the relevant molecular orbitals.

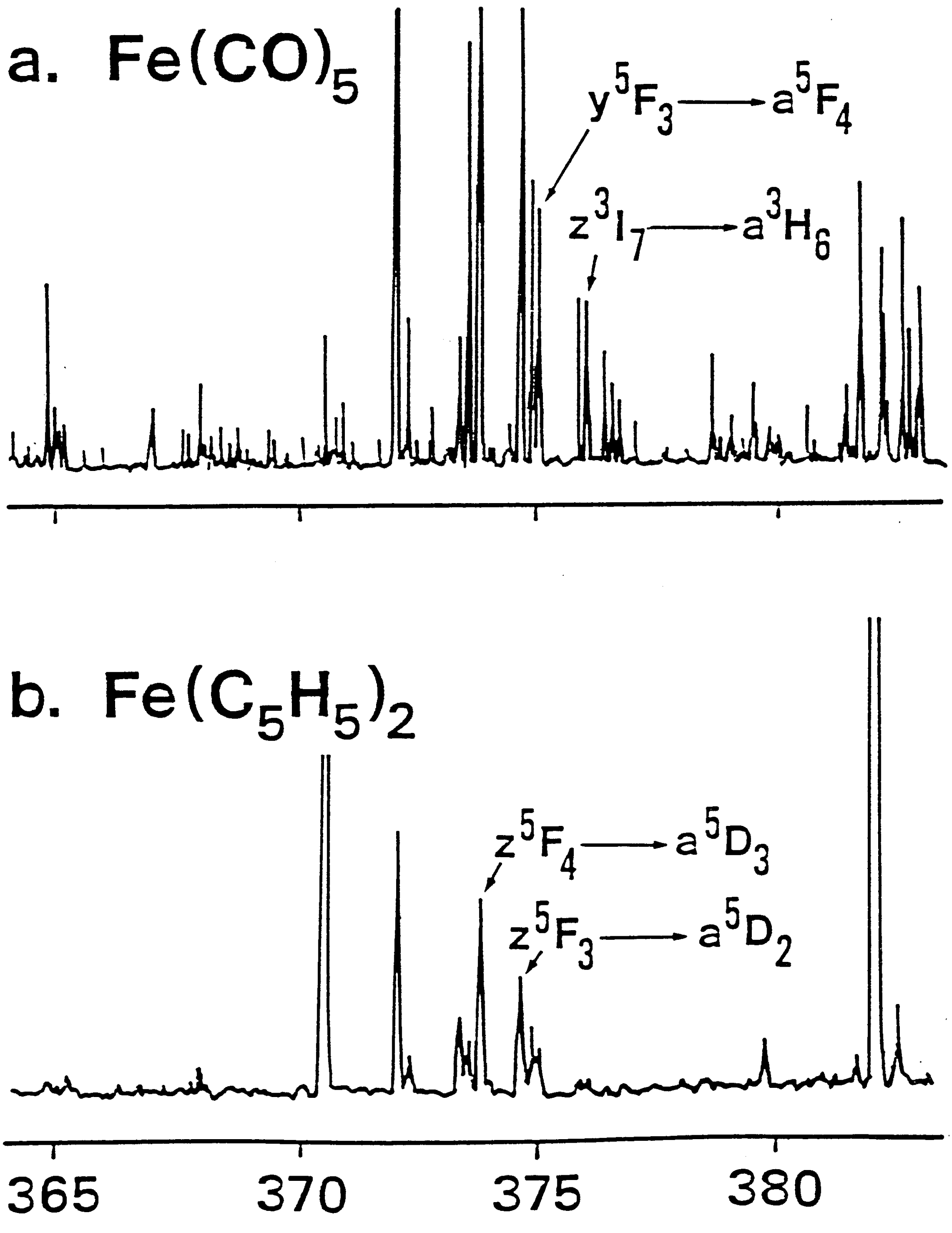
a. $Fe(CO)_5$
$y^5F_3 \longrightarrow a^5F_4$
$z^3I_7 \longrightarrow a^3H_6$
b. $Fe(C_5H_5)_2$
$z^5F_4 \longrightarrow a^5D_3$
$z^5F_3 \longrightarrow a^5D_2$
365
370
375
380
WAVELENGTH /nm

Figure 1

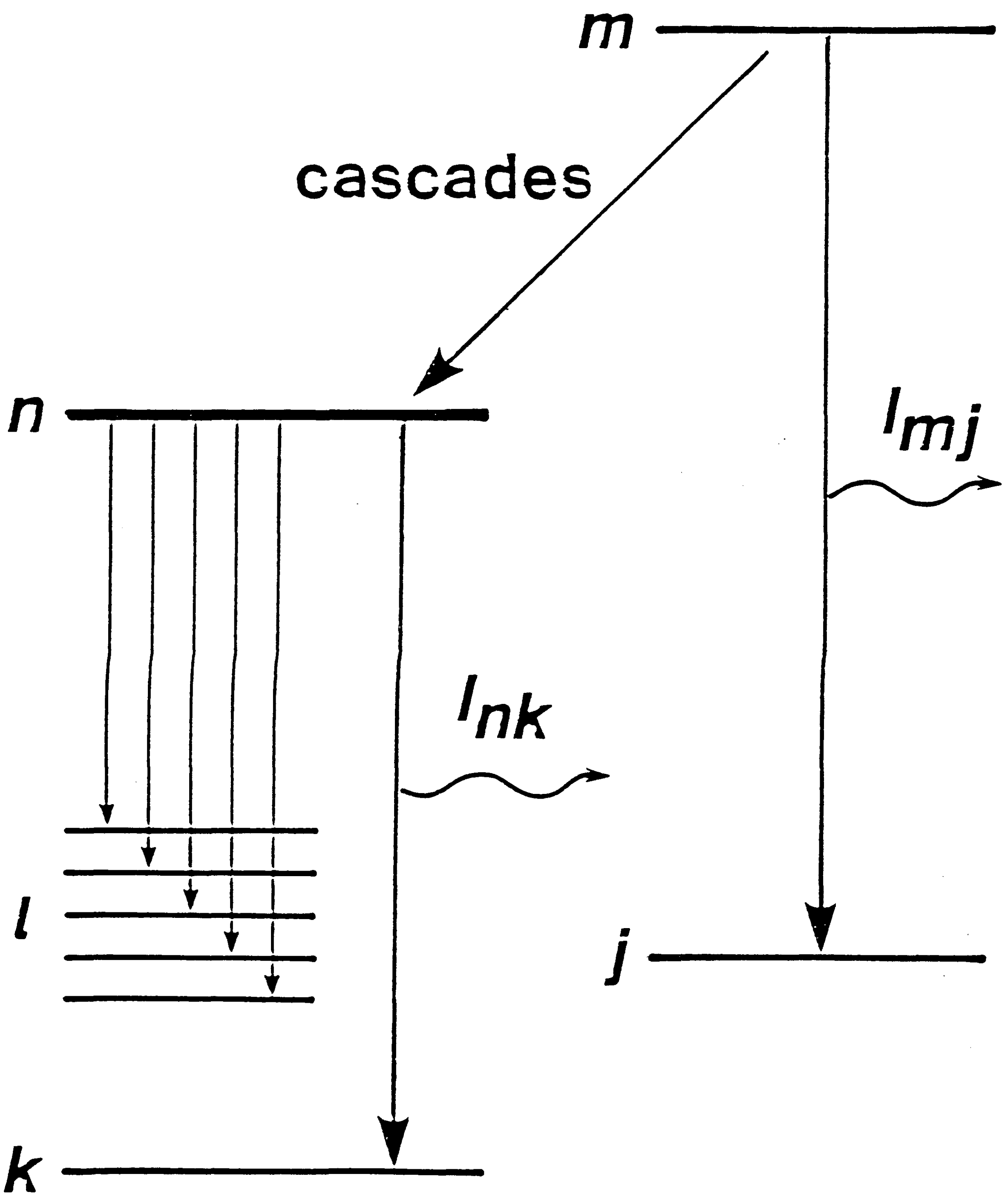

Figure 2

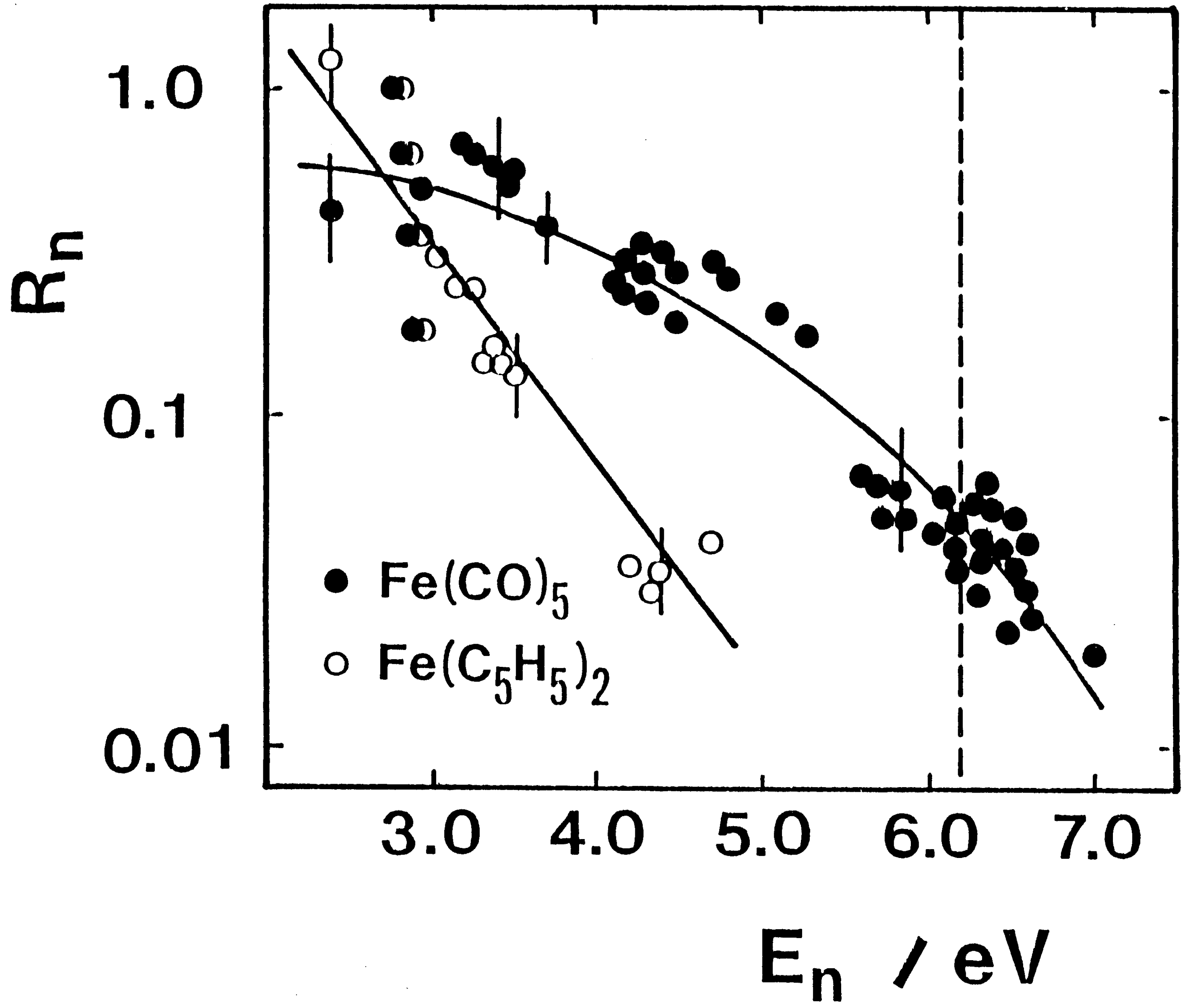

Figure 3

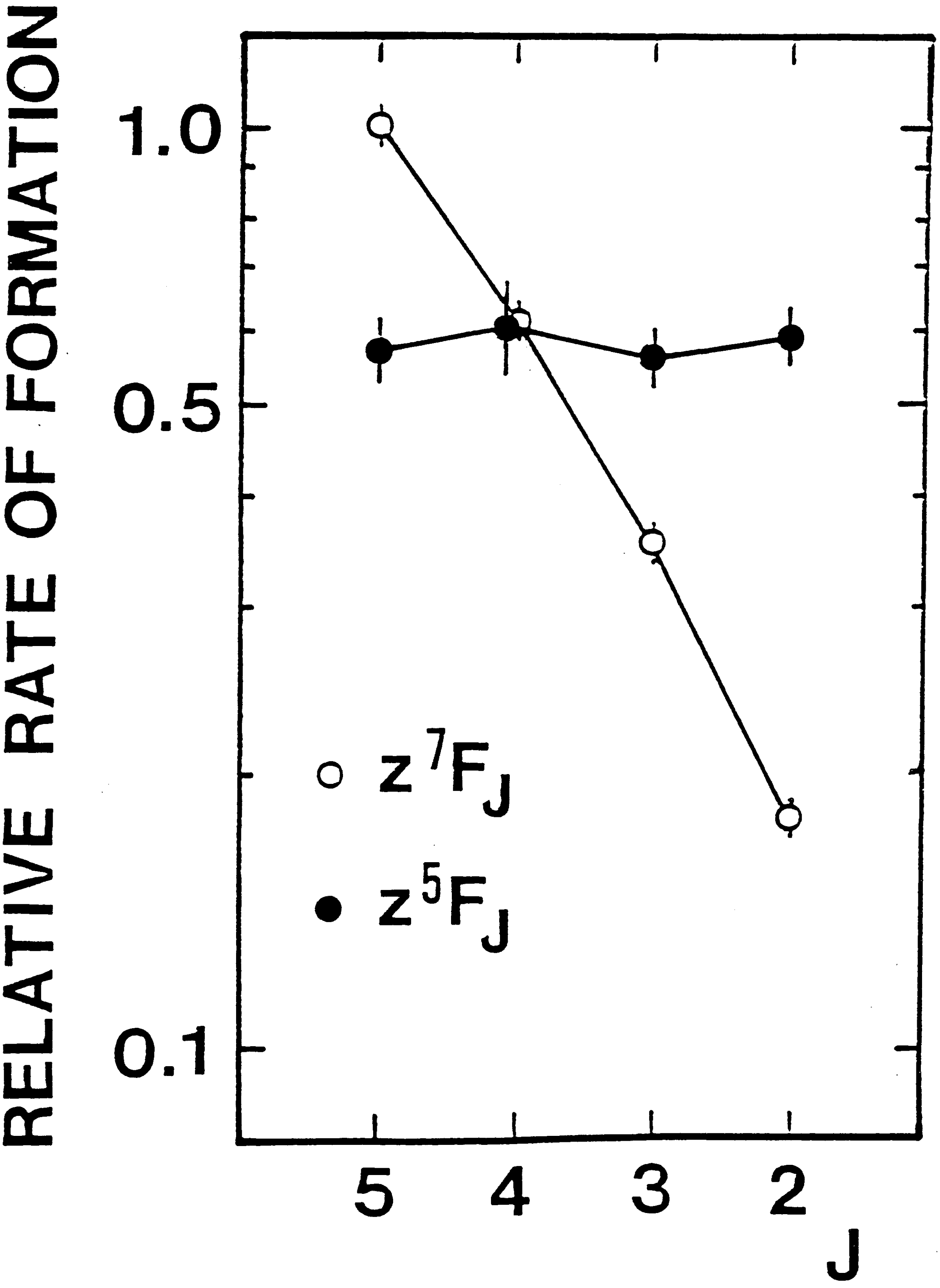

Figure 4

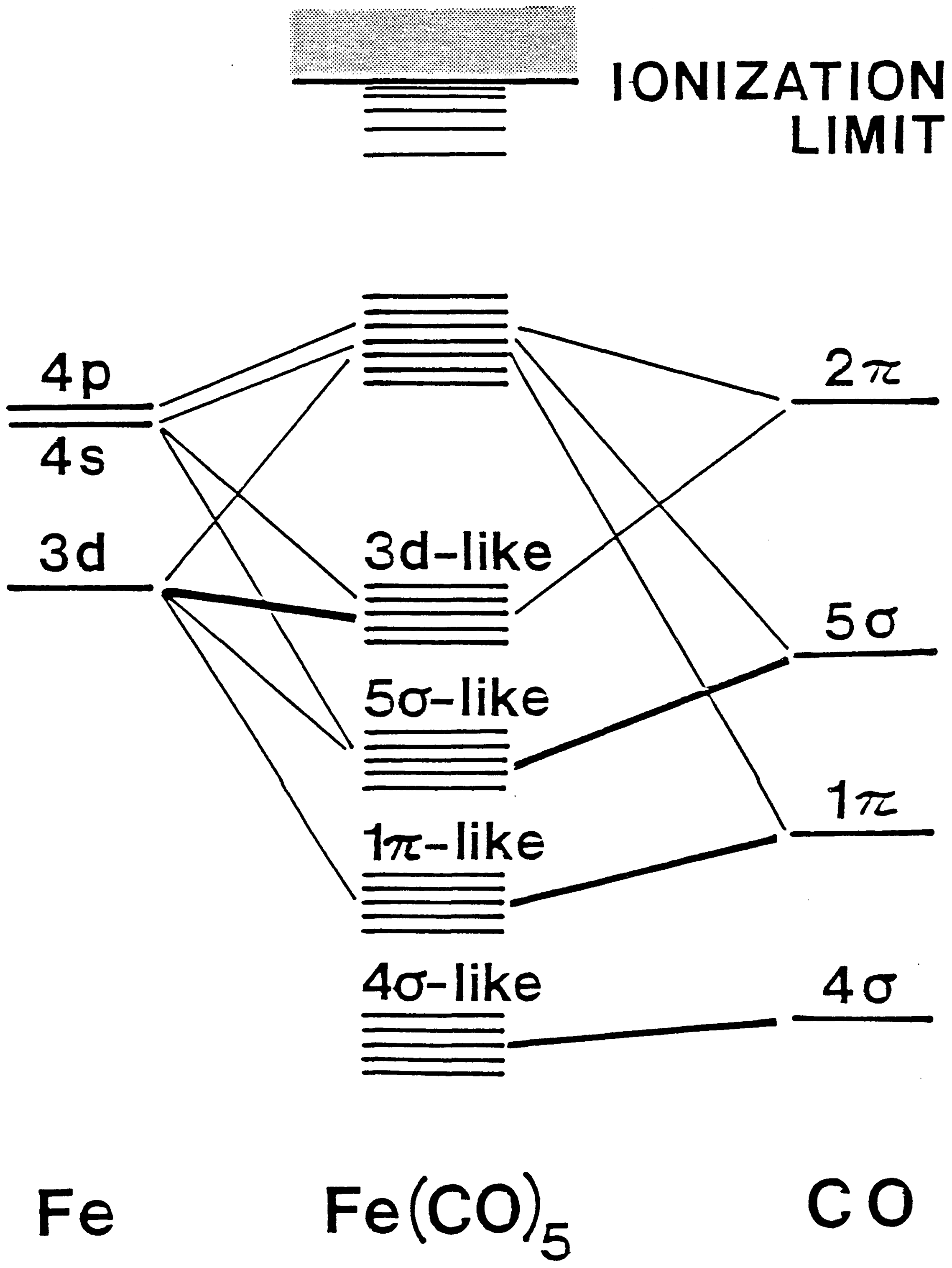
IONIZATION LIMIT
4p
4s
3d
3d-like
5σ-like
1π-like
4σ-like
2π
5σ
1π
4σ
Fe
Fe(CO)5
CO

Figure 5

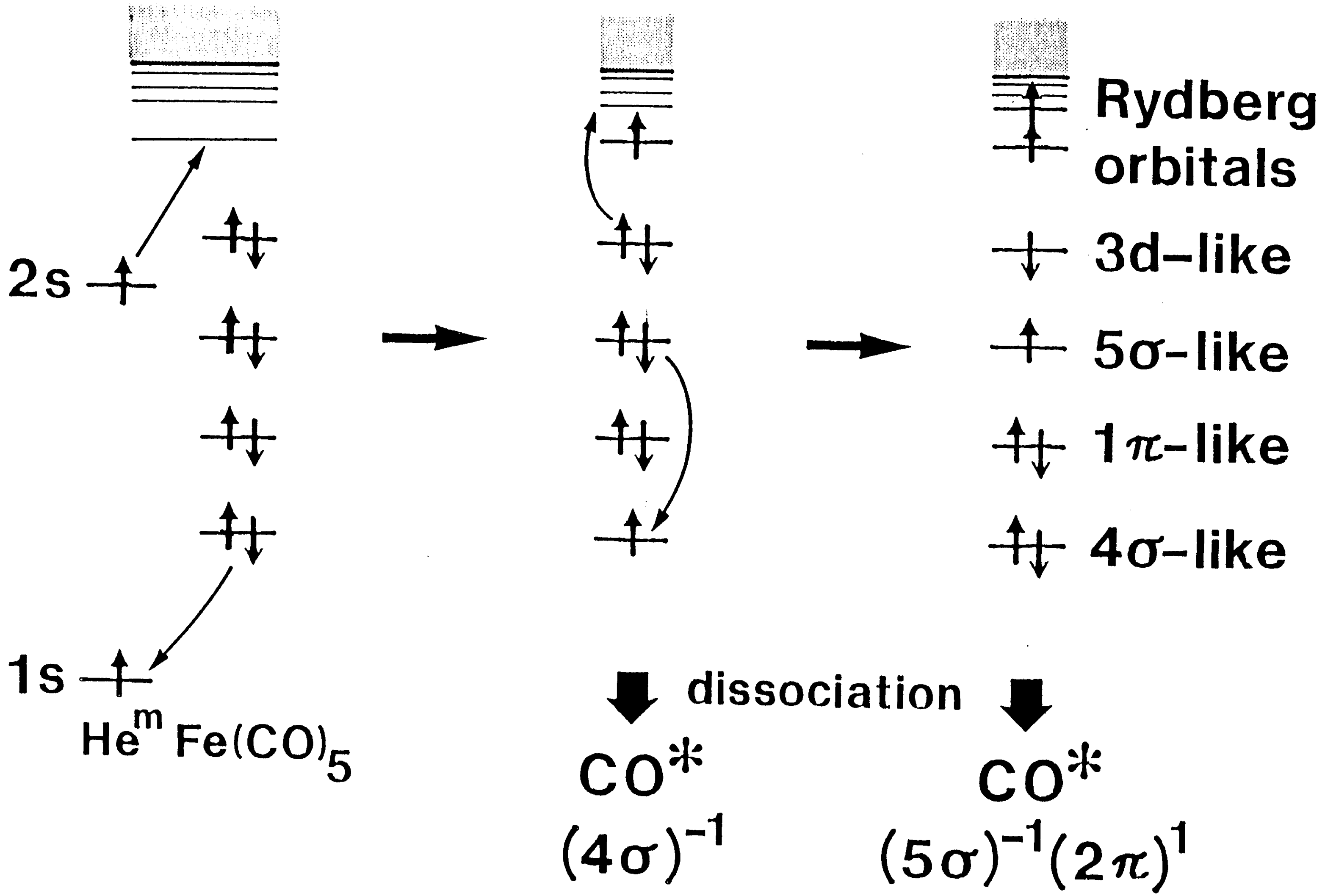
2s
1s
He^m Fe(CO)$_5$
Rydberg orbitals
3d-like
5σ-like
1π-like
4σ-like
dissociation
CO*
(4σ)$^{-1}$
CO*
(5σ)$^{-1}$(2π)^1

Figure 6

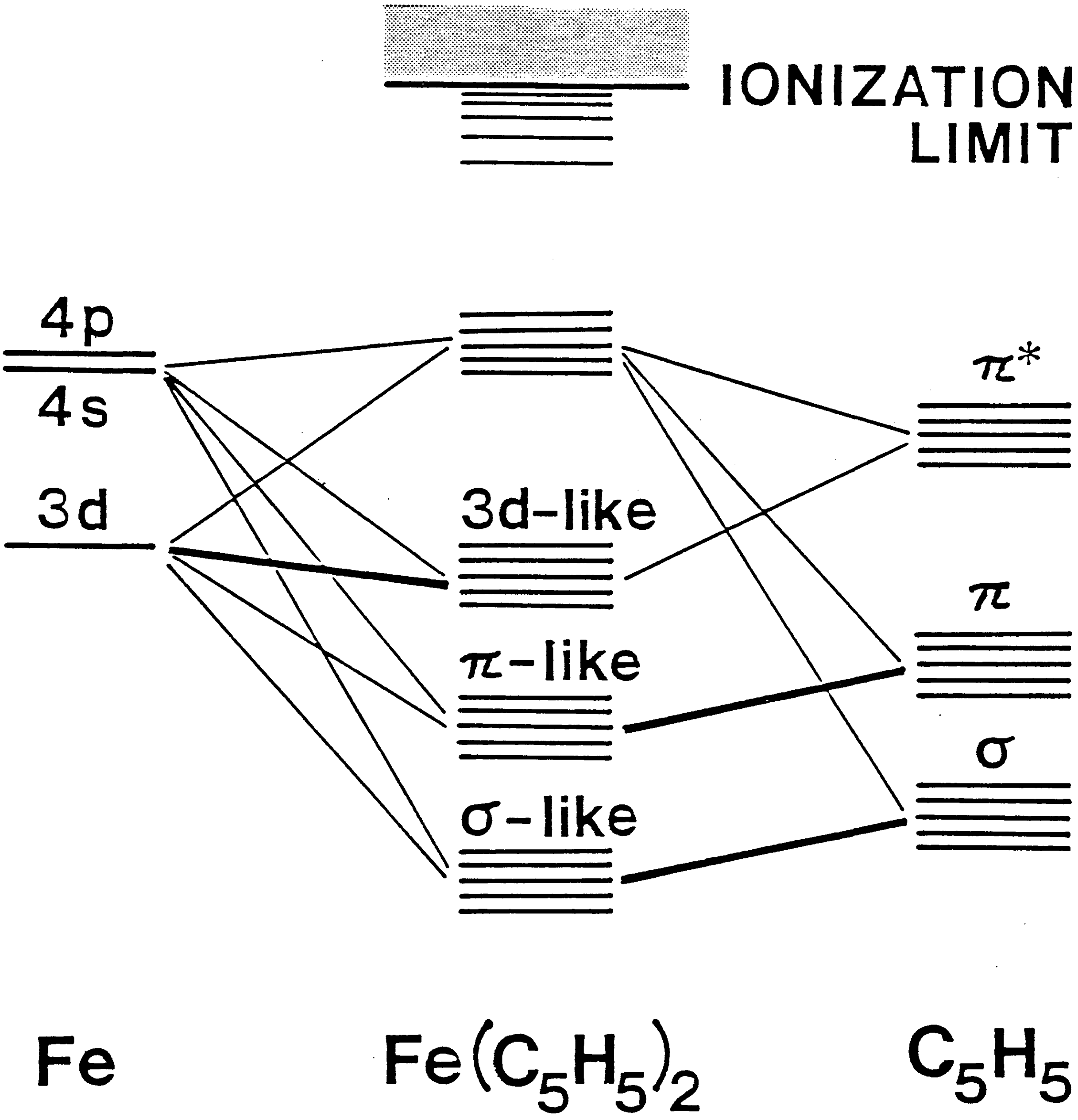
IONIZATION LIMIT
4p
4s
3d
3d-like
π-like
σ-like
π*
π
σ
Fe
Fe(C5H5)2
C5H5

Figure 7

Chapter 3

The n-distributions of H(n) Produced from H_2O, D_2O, and H_2S

ABSTRACT

The Balmer-series emissions from the H($4 \leq n \leq 10$) atoms produced in the reactions of H_2O, D_2O, and H_2S with $He^m(2^3S_1)$ were observed by flowing afterglow experiments. The emission intensities were found to be approximately proportional to $n^{-\beta}$, where the values of β were 2.37 ± 0.04 for H_2O, 2.24 ± 0.08 for D_2O, and 3.39 ± 0.05 for H_2S. This n-dependence is explained by a model which correlates the β value with the branching ratio of the Rydberg precursor states of the parent molecule to (pre)dissociation and autoionization.

INTRODUCTION

Excited hydrogen atoms $H^*(n)$ are produced when hydride molecules are excited by absorption of EUV photons,[1-3] electron impact,[4-7] and excitation transfer from helium metastable atom, $He^m(2^3S_1)$.[8,9] These studies indicate that the excited H atoms are produced by dissociation of parent molecules in highly excited Rydberg states.[4] Many studies have been made on this subject, but only a few of them have discussed on n-distributions of the product $H^*(n)$.[5] The decay rates of these Rydberg states is expected to have essential influence on the n-distribution of the product $H^*(n)$ atoms. Therefore, the n-distribution of the $H^*(n)$ atoms carries vital information on the mechanism of excitation and the lifetime of the transient Rydberg states.

The purpose of the present work is to observe and analyze the Balmer-series emissions produced in the reactions of H_2O, D_2O, and H_2S with He(2^3S_1) by helium flowing afterglow experiments. The *n*-distribution is explained by a model calculation, and the branching ratios of the transient Rydberg states to (pre)dissociation and autoionization are estimated.

EXPERIMENTAL SECTION

The flowing afterglow method was employed.[8] Helium gas, purified by passing through molecular sieve cooled at liquid nitrogen temperature, was let into a discharge region, where He metastable atoms were generated by a microwave discharge (2.45 GHz, 100 W), and then admitted to a reaction chamber, which was evacuated by a mechanical booster pump (500 *l*/s). Charged particles produced simultaneously in the discharge were removed by a pair of grids. The pressure of He in the reaction region was 0.07-0.4 Torr.

The sample gas was introduced 15 cm downstream from the discharge region into the flow. For the experiment on H_2O, distilled water was used after deaeration by several freeze-pump-thaw cycles, while liquid deuterium hydride (Merck, isotopic purity was 99.98%) was used for the experiment on D_2O. Hydrogen sulfide was obtained from a commercial gas cylinder (Takachiho, 99.8% purity) and used without further purification. The pressure of the sample gas in the reaction region was several mTorr.

The emission from the reaction region was dispersed by a 1 m monochromator (Spex 1704) with resolution ranging 0.03-0.1 nm and detected by a photomultiplier (Hamamatsu R585) and a photon-counting system. The spectral response was calibrated by use of a standard lamp.

RESULTS

The Balmer-series emission and weak emission assigned to the OH/OD ($A^2\Sigma^+ - X^2\Pi$) 0-0 band were observed in the experiments on H_2O and D_2O, while the Balmer-series emission and the $SH^+(A^3\Pi-X^3\Sigma^-)$ band were observed in the experiment on H_2S. Emissions from the excited H atoms with principal quantum numbers n ranging $4-20$ were observed, and their relative intensities were measured. The intensity of the emission from $H(n=8)$ could not be measured because this line was accidentally overlapped with a stray He(I) atomic line from the discharge region. Therefore, the intensity of this emission was estimated by interpolation.

The intensities of the Balmer-series emission were found to be independent of the potential applied to the grids; the dependence of the emission intensities on the He pressure was linear and identical to that of the N_2^+(B-X) 0-0 band produced by Penning ionization. On the other hand, the He pressure dependence of the intensity of the OH(A-X) emission, which has been ascribed to the electron-ion recombination,[9] was measured to be quadratic, and the emission intensity decreased to about one half when the potential of 10 V was applied to the grids. Therefore, the active species responsible for the formation of the excited H atoms was assigned to be the $He(2^3S_1)$ atom, and contribution of electron-ion recombination to formation of the excited H atoms was confirmed to be negligible.

The relative intensities of the Balmer-series emission are plotted in Figure 1 against the principal quantum number n of the upper state. Errors were estimated from the fluctuation of the data in several runs of the measurement. The relative emission intensities from $H^*(n\leq 10)$ were found to be independent of the He pressure from 0.07 to 0.4 Torr within experimental error. Therefore, collisional relaxation was assumed to be negligible for $H^*(n\leq 10)$. On the other hand, the relative emission intensities of $H^*(n>10)$, normalized against that of $n=4$, were found to decrease with the He pressure. This pressure dependence is ascribable to collisional relaxation; its influence is expected to increase with n because the cross section for relaxation and the natural lifetime both increase with n. Therefore, the following discussion on the n-dependence of the emission intensity is based only on those with $n \leq 10$.

The n-dependence observed for the D^* emission was found to be slightly weaker than that for the H^* emission. Therefore, a slight isotope effect on the n-dependence is present.

DISCUSSION

A. Dissociation pathways

From energetic considerations the observed processes can be assigned uniquely to

$$He(2^3S_1) + H_2O(\tilde{X}) \rightarrow He(1^1S_0) + OH(X^2\Pi) + H^*(n) \qquad (1)$$

and

$$He(2^3S_1) + H_2S(\tilde{X}) \rightarrow He(1^1S_0) + SH(X^2\Pi) + H^*(n)\ . \qquad (2)$$

The Rydberg H atom is considered to be produced by dissociation of the parent molecule in Rydberg states, MH^{**}, produced by excitation transfer from the $He(2^3S_1)$ atom,

$$He(2^3S_1) + MH \rightarrow He + MH^{**}(n') \qquad (3)$$
$$MH^{**}(n') \rightarrow M + H^*(n), \qquad (4)$$

where M represents OH/OD or SH. Evidence for the formation of $MH^{**}(n')$ with a certain n'-distribution is given in the following subsection A.

A.1 Dissociation pathways of the $He(2^3S_1) + H_2O/D_2O$ reaction

The excited states primarily produced in the energy transfer should have their excitation energies nearly equal to 19.8 eV (the excitation energy of the $He(2^3S_1)$ atom). Possible candidates are limited to the Rydberg states converging to the $\tilde{B}^2B_2$ ionic state, whose ionization potential is 18.51 eV.[10]

Examination on the Penning ionization electron spectrum of H_2O by $He(2^3S_1)$[11] shows that zero electron energy corresponds to a certain vibrationally excited state of the $\tilde{B}^2B_2$ ionic state. Therefore, the vibrationally excited Rydberg states converging to this ionic state, $H_2O^{**}(n')$ with n' up to infinity, can be produced by collision of H_2O with the $He(2^3S_1)$ atom.

The dissociative decay channels of the $\tilde{B}^2B_2$ ionic state have been investigated closely,[12,13] and this ionic state is known to predissociate through the $\tilde{A}^2A_1$, $^2B_1$, and $^4B_1$ ionic states giving $H^+ + OH(X)$, $H^+ + OH(X)$, and $H + OH(X)^+$ fragments, respectively. Therefore, the H_2O molecule excited to the Rydberg states converging to the $\tilde{B}^2B_2$ ionic state predissociates via the Rydberg states converging to the $\tilde{A}^2A_1$ and $^2B_1$ ionic states, and produces an H^* atom. This process has been confirmed experimentally by the EUV photoexcitation of H_2O[2] and has also been supported by the systematic studies of Ogawa et al. on the formation of H^* from H_2O by electron impact excitation.[6]

A.2 Dissociation pathways of the $He(2^3S_1) + H_2S$ *reaction*

The EUV photoabsorption of H_2S has indicated that two excited ionic states are located near 19.8 eV:[14] the $^4A_2$ state (18.2 eV) and the $^4B_1$ state (19.5 eV). Since these ionic states have electron configurations with one singly-occupied antibonding orbital,[15] these states are expected to be dissociative. Therefore, the primary excited states, H_2S^{**}, are expected to be the Rydberg states converging to one of these ionic states, or both, from which H^* is produced through direct dissociation.

B. Analysis of the radiative cascades

The observed relative emission intensities may not represent the relative rates of formation of $H^*(n)$ because of the presence of radiative cascades. In order to obtain exact relative rates of formation from the relative intensities, one needs to know the l-distribution of $H^*(n)$, because the transition probability depends on l as well as n. However, the cross sections for collisional l- and m-mixings of $H^*(n)$ are so large that l and m are no longer good quantum numbers when charged particles and polar molecules are present around the H^* atom. In fact, Wu et al. have shown that H(2s) and H(2p) are completely mixed in the gas cell where several mTorr of H_2O vapor is present.[1] Therefore, under the present experimental conditions the l- and m-distributions can be assumed to become uniform before any radiative transition takes place, even if some substates with specific l or m are preferentially produced.

Under the assumptions stated above, the number density of $H^*(n)$, N_n, satisfies the rate equation,

$$\frac{dN_n}{dt} = -\left(\sum_{m<n} A_{n\text{-}m}\right)N_n + \sum_{k>n} A_{k\text{-}n}N_k + R_n \ . \tag{5}$$

Here, $A_{n\text{-}m}$ represents the average A coefficient, and R_n represents the rate of formation of $H^*(n)$ summed over l and m. The steady-state condition leads to

$$R_n = \left(\sum_{m<n} A_{n\text{-}m}\right)N_n - \sum_{k>n} A_{k\text{-}n}N_k \ . \tag{6}$$

On the other hand, the number density, N_n, is related to the Balmer-series emission intensity, I_n, by

$$I_n = \alpha\omega_{n\text{-}2}A_{n\text{-}2}N_n \ , \tag{7}$$

where $\omega_{n\text{-}2}$ represents the transition frequency and α is a constant. By elimination of N_n and N_k from eq.(6) by use of eq.(7), one obtains

$$R_n = \left(\sum_{m<n} A_{n\text{-}m}\right)\frac{I_n}{\alpha\omega_{n\text{-}2}A_{n\text{-}2}} - \sum_{k>n} A_{k\text{-}n}\frac{I_k}{\alpha\omega_{k\text{-}2}A_{k\text{-}2}} \ . \tag{8}$$

The relative rates of formation summed over l and m were estimated from the observed emission intensities by use of this equation.

C. n-distribution of H(n) / D*(n)*

The emission intensity, I_n, and the rate of formation, R_n, are plotted against n in Figures 1 and 2. The n-dependence of I_n and R_n can be approximated by $I_n = \text{const.} \times n^{-\beta}$ and $R_n = \text{const.} \times n^{-\gamma}$ for n ranging 4-7. The values of the exponents are listed in Table 1. A similar observation has been reported by Möhlmann et al.,[5] who observed the Balmer-series emission from H* produced by impact of 100 eV electrons on several target molecules including H_2O and H_2S. They could represent the n-dependence of I_n by n^{-5} regardless of the parent molecule. Ibuki et al. also reported that the n-dependence of I_n could be represented by n^{-5} in the He(I) photodissociation of H_2S.[3] On the other hand, the n-dependence of I_n observed in the EUV photodissociation of H_2O by Wu et al.[1] could not be represented simply by $n^{-\beta}$. Thus the n-distribution of H* reflects the dynamics of excitation and dissociation of the parent molecules.

D. Model calculation of the n-distribution

In order to explain the observed n-distribution, the following model is set up: The H*(n) atom is formed from the parent molecule in Rydberg states, MH**(n') (see subsection A). Since the Rydberg electron interacts very weakly with the ion-core, MH^+, the n-distribution is hardly affected in the course of dissociation; Thus, the n-distribution of H*(n) is determined by the n-distribution and the decay processes of MH**(n). Generally, Rydberg states have two decay channels: (pre)dissociation and autoionization. Therefore, R_n can be represented by the following four factors,

$$R_n = P_{\text{ex}}(n) \frac{P_{\text{d}}(n)}{P_{\text{i}}(n) + P_{\text{d}}(n) + P_{\text{d}'}(n)} , \tag{9}$$

where

$P_{\mathrm{ex}}(n)$: the excitation probability to $\mathrm{MH}^{**}(n)$,

$P_{\mathrm{d}}(n)$: the rate of (pre)dissociation producing H^*,

$P_{\mathrm{d}'}(n)$: the rate of (pre)dissociation producing fragments other than H^*, and

$P_{\mathrm{i}}(n)$: the rate of autoionization.

The n-dependence of $P_{\mathrm{i}}(n)$ can be approximated to be proportional to n^{-3}. On the other hand, $P_{\mathrm{d}}(n)$ and $P_{\mathrm{d}'}(n)$ can be assumed to be independent of n, because the Rydberg electron is essentially a spectator in the dissociation of the ion-core; in other words, the topography of the potential energy surfaces does not depend on n. It therefore follows that

$$R_n = P_{\mathrm{ex}}(n) \frac{n^3}{n^3 + 64/\Gamma} \frac{P_{\mathrm{d}}}{P_{\mathrm{d}} + P_{\mathrm{d}'}} , \tag{10}$$

where Γ represents the branching ratio of (pre)dissociation to autoionization,

$$\Gamma = (P_{\mathrm{d}} + P_{\mathrm{d}'})/P_{\mathrm{i}}(n=4). \tag{11}$$

The excitation probability, $P_{\mathrm{ex}}(n)$, can be estimated by the Landau-Zener formula as follows: Since the vertical electron affinities of H_2O and H_2S are negative, formation of the ion-pair, $\mathrm{He}^+ + \mathrm{H_2O}^-$(or $\mathrm{H_2S}^-$), can be disregarded. Therefore, it is likely that the potential energy surfaces of $\mathrm{He}^{\mathrm{m}} + \mathrm{MH}$ and $\mathrm{He} + \mathrm{MH}^{**}(n)$ have crossing seams. It is assumed that the transition from $\mathrm{He}^{\mathrm{m}} + \mathrm{MH}$ to $\mathrm{He} + \mathrm{MH}^{**}$ is induced by the relative motion of the He atom with respect to the parent molecule MH, and the internal motions of MH are ignored. Then, the problem is reduced to a one-dimensional potential crossing. The transition probability, P_n, at "the crossing point n" of $\mathrm{He}^{\mathrm{m}} + \mathrm{MH}$ and $\mathrm{He} + \mathrm{MH}^{**}(n)$ is represented by the Landau-Zener formula:

$$P_n = 1 - \exp(-2\pi |H'_n|^2 / V\Delta) , \tag{12}$$

where H'_n is the interaction matrix element, V is the relative velocity at the crossing point, and Δ is the difference between the slopes of two diabatic potential curves, and the atomic units are employed. Strictly speaking, V and Δ depend on n, but these n-dependences are disregarded in the present calculation. The probability of producing MH**(n) is obtained by considering all the possible paths which finally lead to the formation of MH**(n),

$$\begin{aligned} P_{\mathrm{ex}}(n) = {} & P^{\mathrm{s}}(\infty, n+1) P_n (1-P_n) \\ & + \left[\sum_{n'=n_0}^{n-1} P^{\mathrm{s}}(\infty, n'+1) P_{n'}^2 P^{\mathrm{s}}(n'+1, n-1) \right] P_n \\ & + P^{\mathrm{s}}(\infty, n_0) P^{\mathrm{s}}(n_0, n-1) P_{n'} \ , \end{aligned} \tag{13}$$

where

$$P^{\mathrm{s}}(n,m) = \exp\left(- \sum_{k=n}^{m} 2\pi |H'_k|^2 / V\Delta\right) \ . \tag{14}$$

Here, $P^{\mathrm{s}}(n,m)$ represents the probability that the system survives on the $\mathrm{He^m}+\mathrm{MH}$ curve at all the crossing points between n and m, and n_0 is the principal quantum number of the lowest Rydberg state. In the following calculation n_0 is set equal to 3, because the valence shell of H_2O correlates to the L shell in the limit of the united atom. The n-dependence of the matrix element can be approximated by the overlap integral between the Rydberg orbital of MH**(n), ϕ_{nlm}, and the 2s orbital of $\mathrm{He^m}$, ϕ_{2s},[16]

$$|H'_n|^2 \approx \sum_l \sum_m |\langle \phi_{nlm} | \phi_{2s} \rangle|^2 |H'_{\mathrm{core}}|^2 \ , \tag{15}$$

where H'_{core} represents the interaction matrix element of the core electrons and is independent of n. The overlap integrals were calculated numerically, the wave functions being approximated by the corresponding hydrogenic wave functions. The distance between the centers of ϕ_{nlm} and ϕ_{2s} was set to 6-12 atomic units. The n-dependence of H'_n is found to be insensitive to the distance between ϕ_{nlm} and ϕ_{2s} ranging 6-12 a.u.; it is also insensitive to the choice of the parent molecule (the ion-core model).

The n-distribution was calculated by using eq (10)-(15) to reproduce the experimental data. The value of V was estimated to be the thermal velocity, 1.2×10^3 m/s, and the value of $|H'_{\mathrm{core}}|^2$ was assumed to be 10 meV.[16] The overlap integral in eq (15) was estimated at the distance between the centers of ϕ_{nlm} and ϕ_{2s} set equal to 12 a.u. The calculated n-distribution was fitted to the observed one by adjustment of Γ and Δ. It was been shown in the case of H_2O that the n-distribution was reproducible by varying Δ in the range of about 0.1-0.3 eV/Å when Γ was taken in the range $0.04<\Gamma<0.1$. In the case of D_2O, the acceptable range of Γ was $0.03<\Gamma<0.1$. Since Δ, is expected to be isotope independent, those for H_2O and D_2O were set equal to each other; then the value of Γ for H_2O was found to be larger than that for D_2O. As for H_2S, good fitting was obtained when $\Gamma>0.3$ by a suitable choice of Δ ($\Delta<0.25$ eV/Å). It is noted that the absolute value of Δ has little sense because this value depends directly on the estimation of $|H'_{\mathrm{core}}|^2$ (see eq (12)). The orders of magnitude of Γ and Δ obtained above seem to fall in the acceptable range. Therefore, the present model can be regarded as essentially valid.

The value of Γ for H_2S is larger than those of H_2O and D_2O; this indicates that the branching ratio to the dissociation is larger for H_2S^{**} than those for H_2O^{**} and D_2O^{**}. This is understandable in view of the dissociation pathways of H_2S^{**} (see subsection A2), where H_2S^{**} is expected to directly dissociate, whereas H_2O^{**} and D_2O^{**} predissociate. On the other hand, the observation that the value of Γ for H_2O is larger than that for D_2O can be explained as follows: The predissociation rate is smaller for D_2O because the vibrational motions are slower. On the other hand, the rate of autoionization is expected to be isotope independent in the present case, because autoionization of Rydberg states with an electronically excited ion-core is expected to be a purely electronic process. Such isotope effect on the branching ratio has also been observed in the cross section of the formation of H^* in electron impact on the hydrogen-containing molecules.[17]

References

(1) Wu, C. Y. R.; Phillips, E.; Judge, D. L. *J. Chem. Phys.* **1979,** *70,* 601.

(2) Dutuit, O.; Tabche-Fouhaile, A.; Nenner, I.; Frohlich, H.; Guyon, P. M. *J. Chem. Phys.* **1985,** *83,* 584.

(3) Ibüki, T. *J. Chem. Phys.* **1984,** *81,* 2915.

(4) Schiavone, J. A.; Donohue, D. E.; Freund, R. S. *J. Chem. Phys.* **1977,** *67,* 759.

(5) Möhlmann, G. R.; de Heer, F. J. *Chem. Phys.* **1979,** *40,* 157.

(6) Kurawaki, J.; Ueki, K.; Higo, M.; Ogawa, T. *J. Chem. Phys.* **1983,** *78,* 3071.

(7) Kouchi, N.; Ohno, M.; Ito, K.; Oda, N.; Hatano, Y. *Chem. Phys.* **1982,** *67,* 287.

(8) Ozaki, Y.; Kondow, T.; Kuchitsu, K. *Chem. Phys.* **1986,** *109,* 345.

(9) Yencha, A. J.; Wu, K. T. *Chem. Phys.* **1978,** *32,* 247.

(10) Kimura, K.; Katsumata, S.; Achiba, Y.; Yamazaki, T.; Iwata, S. *Handbook of HeI Photoelectron Spectra of Fundamental Organic Molecules;* Japan Scientific Societies Press: Tokyo, 1981.

(11) Ohno, K.; Mutoh, H.; Harada, Y. *J. Am. Chem. Soc.* **1983,** *105,* 4555.

(12) Leclerc, J. C.; Horsley, J. A.; Lorquet, J. C. *Chem. Phys.* **1974,** *4,* 337.

(13) Dehareng, D.; Chapuisat, X.; Lorquet, J. C.; Galloy, C.; Rasev, G. *J. Chem. Phys.* **1983,** *78,* 1246.

(14) Ibuki, T.; Koizumi, H.; Yoshimi, T.; Morita, M.; Arai. S.; Hironaka, K.; Shinsaka, K.; Hatano, Y.; Yagishita, Y.; Ito, K. *Chem. Phys. Lett.* **1985,** *119,* 327.

(15) Hirsch, G.; Bruna, P. J. *Int. J. Mass Spectry. Ion Phys.* **1980,** *36,* 37.

(16) Miller, W. H.; Morgner, H. *J. Chem. Phys.* **1977,** *67,* 4923.

(17) Tokue, I.; Nishiyama, I.; Kuchitsu, K. *Chem. Phys. Lett.* **1975,** *35,* 69.

TABLE I

Exponents of the n-dependence of I_n and R_n .[a]

	H_2O	D_2O	H_2S
β	2.37(4)[b]	2.24(8)	3.39(5)
γ	1.53(6)	1.33(11)	2.68(5)

a) I_n and R_n represent the relative emission intensities and the relative rates of formation of $H^*(n)$, respectively. Their n-dependence are expressed by $I_n = \text{const.} \times n^{-\beta}$ and $R_n = \text{const.} \times n^{-\gamma}$ (see DISCUSSION C).

b) Numbers in parentheses represent standard deviations obtained in the least-square fitting.

Figure Captions

Figure 1: Log-log plots of the emission intensities of $H^*(n)$, I_n. The values of I_n's are normalized against I_4. The values of I_8 could not be measured because the corresponding Balmer line was accidentally overlapped with a stray HeI line. The plots in parentheses represent I_8 obtained by interpolation.

Figure 2: Log-log plots of the rate of formation of $H^*(n)$, R_n. The values of R_n's are normalized against R_4. The lines represent the n-distributions calculated by a model (see DISCUSSION D) with $\Delta = 0.25$ eV/Å and the indicated values of Γ. The definitions of Γ and Δ appear in eqs.(10) and (12), respectively.

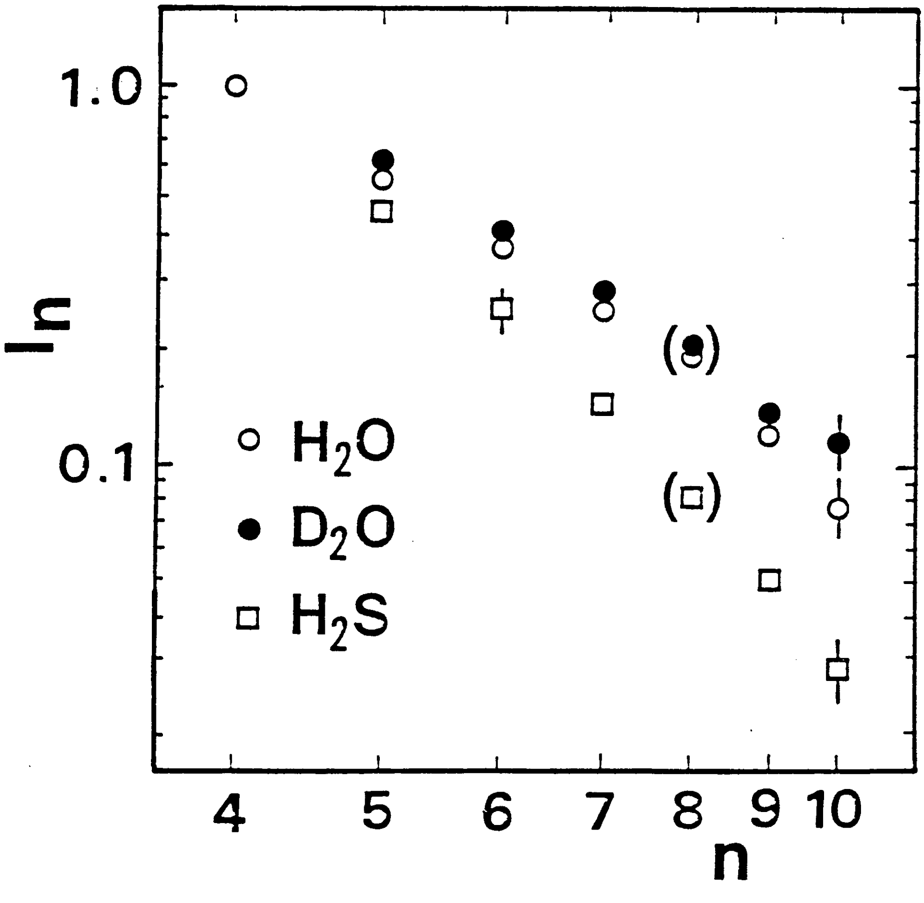

Figure 1

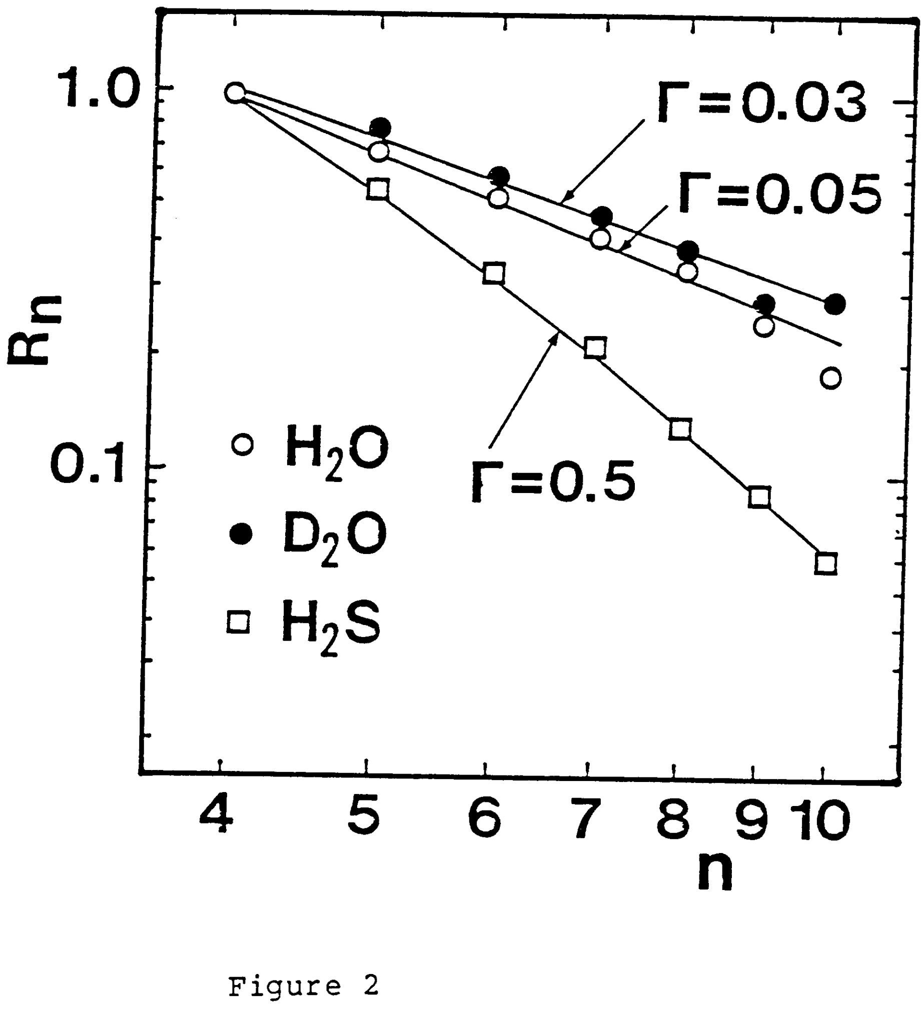

Figure 2

Chapter 4

Mechanism of the Formation of Doubly-Excited States of HCl

ABSTRACT

The dissociative excitation of HCl in collision with He(2^3S_1),

$$He(2^3S_1)+HCl(X^1\Sigma^+)\rightarrow He(1^1S_0)+Cl(^2P)+H^*(n>2),$$

is investigated by performing an SCF-CI calculation of the potential energy hypersurfaces relevant to this reaction. The most likely transient excited states of HCl are found to be the dissociative Rydberg states, $2^2\Sigma^+-4s$ and $1^4\Pi-4p$, which have doubly-excited configurations, $(3p\pi)^{-2}(3p\sigma^*)^1(4s)^1$ and $(3p\sigma)^{-1}(3p\pi)^{-1}(3p\sigma^*)^1\,(4p)^1$, respectively. Mechanisms of the formation of these doubly-excited states are studied. It is found that the formation of the $2^2\Sigma^+-4s$ state is induced by mixing of the inner valence hole configuration, $(3s\sigma)^{-1}(4s)^1$, into the $2^2\Sigma^+-4s$ state, while the $1^4\Pi-4p$ state is produced by mixing of a charge-transfer configuration, He^++HCl^-, with $He(2^3S_1)+HCl$ and $He+HCl(1^4\Pi-4p)$ as initial and final states, respectively.

INTRODUCTION

In the excitation-transfer reactions of He(2^3S_1) with a target molecule, formation of doubly-excited states of the target molecule has been suggested in several experimental studies.[1-3] Formation of a doubly-excited state is an optically forbidden process unless singly-excited configurations are mixed with the doubly-excited state in question. Similarly, no doubly-excited state can be produced by the electron-exchange mechanism, which has been postulated for the excitation-transfer from He(2^3S_1) to a target atom or molecule;[4] namely, a singly-excited state of the target molecule is formed by electron exchange, in which one electron of the target molecule fills the 1s hole of He(2^3S_1) and the 2s electron of He(2^3S_1) is transferred to the target molecule. However, doubly-excited states can be produced in excitation-transfer, as in photoexcitation, by mixing of singly-excited configuration(s). Even when such mixing of configurations does not occur, it is likely that the presence of the He(2^3S_1) atom perturbs the electronic structure of the target molecule and enables formation of a doubly-excited state.

An example of the excitation-transfer reaction in which doubly-excited states are expected to be produced is the dissociative excitation of HCl in collision with He(2^3S_1) ,[5]

$$\mathrm{He}(2^3S_1)+\mathrm{HCl}(X^1\Sigma^+)\rightarrow\mathrm{He}(1^1S_0)+\mathrm{Cl}(^2P)+\mathrm{H}^*(n>2), \qquad (1)$$

in which the transient dissociative states of HCl are inferred to be doubly-excited states for the following reason: In this reaction, HCl is considered to dissociate via dissociative Rydberg states because a Ryberg hydrogen atom is produced.[6] However, the singly-excited Rydberg states which converge to the single hole states of HCl^+ such as $X^2\Pi(3p\pi)^{-1}$, $A^2\Sigma^+(3p\sigma)^{-1}$, and $3^2\Sigma^+(3s\sigma)^{-1}$ are unlikely to be located near the excitation energy of He(2^3S_1), 19.8 eV. Theoretical studies of the HCl^+ electronic states suggest that the ionic states with 2-hole-1-particle configurations are located in the region of 20-25 eV.[7,8] This has been verified by the photoelectron spectrum[9] and the electron-energy-loss spectrum[10] of HCl. Accordingly, the doubly-excited Rydberg states converging to these ionic states are likely to be the transient dissociative states involved in reaction (1). In order to confirm this assignment and to study the mechanism of formation of doubly-excited states, the potential energy surfaces of the He+HCl system relevant to reaction (1) were calculated in the present study by an ab initio SCF-CI method. The transient dissociative states of HCl are indeed shown to be doubly-excited Rydberg states. The possible mechanisms of formation of these doubly-excited states are discussed.

CALCULATION

A. Potential energy curves of the excited states of HCl^+.

Program GSCF3[11,12] was used for all SCF and CI calculations throughout the present study. The contracted gaussian basis sets given by Dunning and Hay[13] were employed. For the chlorine atom the (11s,7p)/[6s,4p] basis set was augmented with a d polarization function (exponent $\alpha=0.75\ a_0^{-2}$), while for the hydrogen atom the (4s)/[2s] basis set was augmented with a p polarization function (exponent $\alpha=1.0\ a_0^{-2}$). An SCF calculation was carried out for the lowest $^4\Pi$ state of HCl^+, and the resultant molecular orbitals were used for the CI calculation.

In the CI calculations, single and double substitutions from all the valence-type reference configurations were taken into account, where the excitations to the lowest 14 virtual MO's were considered. The lowest five occupied MO's, which correspond to the K and L shells of chlorine, were kept doubly occupied. All the CI calculations were carried out in the C_{2v} subgroup of the $C_{\infty v}$ molecular point group. The total number of the configuration state functions was about 8000.

B. Energies of the Rydberg states

The vertical excitation energies of the Rydberg states located near 20 eV were calculated. The basis set on the chlorine atom described in subsection A was further augmented with diffuse (Rydberg-like) functions, i.e., two s functions ($\alpha=0.015$ and 0.005) and two sets of the p function ($\alpha=0.022$ and

0.004). These exponents had been optimized by monitoring the SCF orbital energies of the vacant orbitals which correspond to the Rydberg orbitals bound to the ion-core, $HCl^+(X^2\Pi)$. The molecular orbitals generated by the SCF calculation for the lowest $^4\Pi$ states of HCl^+ were used for the CI calculation.

In the CI calculation, reference configurations were composed of all the valence- and Rydberg-type configurations, and single and double substitutions to the lowest four virtual MO's were allowed, where the configurations in which two or more electrons occupy the Rydberg MO's were excluded. The K and L shells of chlorine were frozen. The total number of the configuration state functions was about 8000.

On the other hand, the energies of the $1^4\Pi$ ionic states were calculated with the CI calculation in which no Rydberg MO's were occupied at all, and the energies of the Rydberg states relative to that of the $1^4\Pi$ ionic state were obtained. The excitation energies from $HCl(X^1\Sigma^+)$ were determined from these relative energies and the ionization potential of $1^4\Pi$ obtained by the more accurate calculation described in subsection A.

C. Potential energy surfaces of the He-HCl system

The basis sets for the chlorine and hydrogen atoms were the same as those described in subsection B. For the helium atom, the (5s)/[3s] basis set was augmented with diffuse s and p functions ($\alpha = 0.05$ and 0.22 respectively[14]) in order to describe the 2^3S_1 state of He which has a Rydberg character. In order to estimate the energy gaps of the avoided crossings between $He(2^3S_1) + HCl$ and $He + HCl^{**}$, where HCl^{**} represents the Rydberg states with doubly-excited configurations located near 20 eV, the energies of these states were obtained as different roots orthogonalized in a single CI diagonalization. In order to avoid any bias in the relative accuracy of the

$He(2^3S_1)+HCl$ and $He+HCl^{**}$ states, the molecular orbitals of $He+HCl^+(A^2\Sigma^+)$ were used for the CI calculation.

In the CI calculation, the configurations obtained by distributing electrons in the valence and Rydberg MO's were taken into consideration, excluding the configurations with two or more electrons in the Rydberg MO's of HCl and MO's of He-2p character. The K and L shells of chlorine were frozen. The total number of the configuration state functions was about 5500.

RESULTS

A. Potential curves of the excited states of HCl^+

The calculated potential energy curves are shown in Figure 1. The total energies are shifted to make the vertical ionization potential of the $A^2\Sigma^+$ state agree with the experimental value, 16.28 eV.[15] The calculated vertical ionization potentials are listed in Table I. In Figure 1, many repulsive states are found to be located at about 20 eV and all the states have doubly-excited configurations with reference to $HCl(X^1\Sigma^+)$. However, the $2^2\Sigma^+$ state, in which the most significant configuration is $(3p\pi)^{-2}(3p\sigma^*)^1$, is found to be strongly mixed with the inner-valence hole configuration, $(3s\sigma)^{-1}$. In fact, this $2^2\Sigma^+$ state can be produced substantially in photoionization through the intensity borrowing from the $(3s\sigma)^{-1}$ state,[9,10] which is predominant in the $3^2\Sigma^+$ state. On the other hand, the doubly-excited states other than $2^2\Sigma^+$ are not mixed with the inner-valence hole configuration, $(3s\sigma)^{-1}$, because of their different symmetries, and therefore, formation of these ionic states is essentially optically forbidden.

B. Energies of the Rydberg states

The calculated vertical excitation energies of the Rydberg states located at about 20 eV are listed in Table II. Only the 4s, 4p, 5s, and 5p states of each

Rydberg series are considered, where the lowest principal quantum number of the Rydberg state is tentatively assigned to be 4. The energy of the *nl* state converging to a given ionic state increases with *l* when *n* is fixed. Therefore, the Rydberg states with $l \geq 2$ converging to the ionic states other than the $1^4\Sigma^-$ state are expected to be located at above 20 eV and energetically inaccessible in the reaction in question. On the other hand, the Rydberg states with $l \geq 2$ converging to the $1^4\Sigma^-$ state are possibly located at about the excitation energy of He(2^3S_1), 19.81 eV. However, these states are essentially insignificant in the reaction under study; see DISCUSSION.

C. Potential energy surfaces of the He-HCl system

Typical sections and a three-dimensional plot of the potential surfaces are shown in Figures 2-5. The asymptotic energies of the excited states of the He+HCl system relevant to the reaction in question are listed in Table II. The excitation energies are shifted to make the asymptotic energy of He(2^3S_1)+HCl equal to 19.81 eV. The excitation energies of HCl** are consistent with those obtained by the calculation for the isolated HCl molecule described in CALCULATION B (see Table II).

The potential energy curves which appear in the section with a fixed internuclear distance of H and Cl, *r*(H-Cl), are found to be repulsive as shown in Figure 2. Avoided crossings appear in the section with a fixed internuclear distance of He and Cl, *R*(He-Cl), and the energy gaps increases as *R*(He-Cl) decreases. Details of the crossing seams are shown in Figures 3-5. In the case of the collinear approach of He on the Cl end of HCl, one can observe two avoided crossings as shown in Figure 3: Namely, He+HCl**($2^2\Sigma^+-4s$) and He+HCl**($1^4\Pi-4p$) have avoided crossings with He(2^3S_1)+HCl. In the case of the sideway attack shown in Figure 4, an avoided crossing can be observed only between He(2^3S_1)+HCl and He+HCl**($2^2\Sigma^+-4s$), and the energy gaps of the crossings between the He(2^3S_1)+HCl state and the He+HCl** states other than He+HCl**($2^2\Sigma^+-4s$) is too small to be observable (less than 0.01 eV), although both states have the same total symmetry,$^3A'$. The origin of this phenomenon is discussed in the following section. In the case of the collinear approach of He on the H end of HCl, shown in Figure 5, an avoided crossing can be observed only between He(2^3S_1)+HCl and He+HCl**($2^2\Sigma^+-4s$), as shown in the case of the sideway attack (Figure 4), but the former energy gap is much narrower than the latter.

DISCUSSION

*A. Mecanisms of the transition from He(2^3S_1)+HCl to He+HCl**.*

As mentioned in RESULTS C, the He(2^3S_1)+HCl state interacts only with the He+HCl**($2^2\Sigma^+-4s$) state in the case of the sideway attack of He(2^3S_1) on HCl (Figure 4). This observation can be interpreted as follows: The most significant configurations of the He+HCl** states are obtained by three-electron excitation from the main configuration of He(2^3S_1)+HCl, as illustrated in Figures 6 and 7, so that the Hamiltonian matrix elements between these configurations vanish. Therefore, the avoided crossings shown in Figures 3-5 are considered to originate from mixings of certain intermediate configurations into the entrance and excit channels. The $2^2\Sigma^+-4s$ state of HCl was found to be mixed strongly with the $(3s\sigma)^{-1}(4s)^1$ configuration, which is predominant in the $3^2\Sigma^+-4s$ state; this mixing originates from the mixing in the ion-core state, $2^2\Sigma^+$, as mentioned in RESULTS A. Consequently, the He+HCl**($2^2\Sigma^+-4s$) state can interact with the He(2^3S_1)+HCl state through mediation of the He+HCl**($(3s\sigma)^{-1}(4s)^1$) configuration, as illustrated in Figure 6. On the other hand, the doubly-excited states, HCl**, other than HCl**($2^2\Sigma^+-4s$) does not mix with the $(3s\sigma)^{-1}(4s)^1$ configuration because the symmetries of the ion-cores are different from $^2\Sigma^+$, and consequently, the avoided crossings between these He+HCl** states and the He(2^3S_1)+HCl state are very small. The above mechanism of the formation of HCl** resembles that in the "shake-down" process in photoionization,[17] in which the $2^2\Sigma^+$ ionic state is produced from the intensity borrowing from the inner valence hole state, $3^2\Sigma^+$.[9,10]

In the case of the collinear approach of He(2^3S_1) on the Cl end of HCl shown in Figure 3, the He+HCl**($1^4\Pi-4p$) state as well as the He+HCl**($2^2\Sigma^+-4s$) state interacts with the He(2^2S_1)+HCl state. The avoided crossing between He(2^3S_1)+HCl and He+HCl**($1^4\Pi-4p$) is considered to be caused by mediation of the charge transfer configuration, $He^+ + HCl^-$, as shown in Figure 7. This is verified by examining the Hamiltonian matrix elements on the crossing seam: Namely, the value of $<f|H|n><n|H|i>$, where $|i>$ and $|f>$ represent the most significant configurations of the He(2^3S_1)+HCl state and the He+HCl** state respectively, is the largest when $|n>$ is the charge transfer configuration, $He^+ + HCl^-$, in which the lowest unoccupied antibonding $3p\sigma^*$ orbital of HCl is occupied. The observation that the He+HCl**($1^4\Pi-4p$) state has no substantial interaction with the He(2^3S_1)+HCl state in the case of the sideway attack of He(2^3S_1) can be interpreted by a steric effect of the molecular orbital. Since the $3p\sigma^*$ orbital of HCl has its electron density mainly on the HCl molecular axis, the overlap of the $3p\sigma^*$ orbital of HCl and the 2s orbital of He(2^3S_1) is small in the sideway attack, and consequently, the mediation of the charge transfer configuration is ineffective.

B. Reaction Path

On the basis of the calculated potential energy surfaces, the present reaction can be interpreted by the following picture: When He(2^3S_1) approaches

HCl, the motion of the zero-point vibration of HCl causes the transition from $He(2^3S_1)+HCl$ to $He+HCl^{**}$ through the avoided crossings shown in Figures 3-5, and HCl^{**} dissociates to produce H^*+Cl and/or $H+Cl^*$. The energy of the zero-point vibration is estimated to be about 0.2 eV from the vibrational frequency of the isolated HCl molecule, 2991 cm^{-1}.[16] Therefore, the $He+HCl^{**}(2^2\Sigma^+-4s)$ state and the $He+HCl^{**}(1^4\Pi-4p)$ states are both accessible. The $He+HCl^{**}(2^2\Sigma^+-4s)$ state is expected to be the dominant final channel. This is because the energy gap of the corresponding avoided crossing is very large and the wave function of the vibration of HCl has its maximum around the avoided crossing between $He(2^3S_1)+HCl$ and $He+HCl^{**}(2^2\Sigma^+-4s)$, which is located near the bottom of the potential curve. The $He+HCl^{**}(1^4\Pi-4p)$ state is considered to be the second dominant channel, but the probability of the transition to this channel is expected to be much smaller than that of the transition to $He+HCl^{**}(2^2\Sigma^+-4s)$ in view of the magnitudes of the energy gaps. The $He+HCl^{**}$ states with energies higher than $He+HCl^{**}(1^4\Pi-4p)$ may have avoided crossings with $He(2^3S_1)+HCl$ at r(H-Cl) larger than 1.4 Å, but these channels are expected to be less significant because the nuclear wave function is small around the avoided crossing located at large r(H-Cl). On the other hand, the Rydberg states with $l\geq2$ converging to the $1^4\Sigma^-$ state are possibly located near 19.8 eV (see RESULTS B), and the corresponding $He+HCl^{**}$ states are expected to have intersections with the $He(2^3S_1)+HCl$ state at $r(H-Cl)<1.4$ Å. However, these states are not expected to be significant exit channel in the case of the sideway attack, because the $3^2\Sigma^+$ state does not mix with the $1^4\Sigma^-$ state on account of different symmetry. In the case of collinear attack, the $He+HCl^{**}(1^4\Sigma^- - nl)$ states have symmetries different from that of $He(2^3S_1)+HCl$, and therefore, they cannot be the exit channel.

The potential curves of HCl^+ intersect with each other in a complicated manner (see Figure 1). This indicates that the corresponding potential curves of the Rydberg states, $HCl^{**}(2^2\Sigma^+ - 4s)$ and $HCl^{**}(1^4\Pi - 4p)$, intersect with other Rydberg states with different ion-core states. Therefore, the electronic state of the ion-core and the quantum numbers *n* and *l* are expected to change in the course of the dissociation of HCl^{**}. These intersections are considered to govern the branching ratio of the products, $H^* + Cl$ and $H + Cl^*$, and the *n*-distribution of H^*.

References

(1) Ozaki, Y.; Kondow, T.; Kuchitsu, K. *Chem. Phys.* **1986,** *109,* 345.

(2) Chapter 1

(3) Chapter 2

(4) Niehaus, A. *Ber. Bunsenges. Phys. Chem.* **1973,** *77,* 632.

(5) Richardson, W.C.; Setser, D.W. *J. Chem. Phys.* **1973,** *58,* 1809.

(6) Higo, M.; Ogawa, T. *Chem. Phys.* **1979,** *44,* 279.

(7) Ibuki, T.; Sato, N.; Iwata, S. *J. Chem. Phys.* **1983,** *79,* 4805.

(8) von Niessen, W.; Cederbaum, L.S.; Domcke, W.; Diercksen, G.H.F. *Chem. Phys.* **1981,** *56,* 43.

(9) Adam, M.Y. *Chem. Phys. Letters* **1986,** *128,* 280.

(10) Daviel, S.; Iida, Y.; Carnovale, F.; Brion, C.E. *Chem. Phys.* **1984,** *83,* 319.

(11) Kosugi, N. Program GSCF3, Program Library, The Computer Centre, The University of Tokyo (1985).

(12) Kosugi, N. *Theoret. Chim. Acta* **1987,** in press.

(13) Dunning Jr., T.H.; Hay, P.J. in *Modern Theoretical Chemistry* **1977,** *3,* Chapter 1.

(14) Hang, B.; Morgner, H.; Staemmler, U. *J. Phys., B* **1985,** *18,* 259.

(15) Kimura, K.; Katsumata, S.; Achiba, Y.;Yamazaki, T.; Iwata, S. *Handbook of HeI Photoelectron Spectra of Fundamental Organic Molecules;* Japan Scientific Societies Press: Tokyo, 1981.

(16) Huber, K.P.; Herzberg, G. *Constants of Diatomic Molecules;* Van Nostrand: New York, 1979.

(17) Hamnett, A.; Stoll, W.; Brion, C.E. *J. El. Spectrosc.* **1976,** *8,* 367.

TABLE I. Vertical ionization potentials of HCl^+ (in eV).

state	calc.[a]	obs.
$X^2\Pi$	12.08	12.75 and 12.85[b,c]
$A^2\Sigma^+$	16.28	16.28[c]
$1^4\Sigma^-$	20.82	–[d]
$1^2\Sigma^-$	21.93	–[d]
$1^2\Delta$	22.83	–[d]
$1^4\Pi$	23.30	–[d]
$2^2\Sigma^+$	23.54	23.65[e]
$2^2\Pi$	25.03	–[d]
$3^2\Sigma^+$	27.22	25.85[e]

a) The present calculation of the ionization potential at r(H-Cl) = 1.268 Å (r_e of HCl(X)).[16] The total energies were shifted so as to make that of the $A^2\Sigma^+$ state equal to 16.28 eV.

b) Split due to spin-orbit interaction.

c) ref.15.

d) No experimental values have been reported.

e) ref.9.

TABLE II. Excitation energies (in eV) of the Rydberg states

state	I[a)]	II[b)]
$1^4\Sigma^- - 4p_-$	18.81	19.27
$1^4\Sigma^- - 5p_-$	20.03	20.54
$1^2\Sigma^- - 4p_-$	20.08	20.15
$1^2\Delta - 4s$	20.10	19.81
$1^4\Pi - 4s$	20.16	20.25
$2^2\Sigma^+ - 4s$	20.63	20.28
$1^4\Pi_+ - 4p_+$	20.88	21.45
$1^2\Delta - 4p\sigma$	20.18	-
$1^4\Pi - 4p\sigma$	21.11	-
$2^2\Sigma^+ - 4p\sigma$	21.65	-
$2^2\Pi - 4s$	21.68	-
$1^2\Delta - 5s$	22.05	-
$1^4\Pi_+ - 5p_+$	22.12	-

a) Calculated on isolated HCl (see CALCULATION B).

b) Calculated on He+HCl (see CALCULATION C and RESULTS C). The He atom is placed 6.0 Å apart from the Cl atom on the Cl side of the molecular axis of HCl.

Figure Captions

Figure 1: Potential energy curves of HCl^+ calculated in the present work (see CALCULATION A and RESULTS A).

Figure 2: Three-dimensional plot of the potential energy surfaces of $He(2^3S_1)+HCl(X^1\Sigma^+)$ and $He(1^1S_0)+HCl^{**}(2^2\Sigma^+-4s)$ in the case of the sideway attack of He on the HCl; the Cl atom is at the origin, the H atom is on the x-axis, and the He atom is on the y-axis.

Figure 3: A section of the potential energy surfaces in the case of the collinear attack of He on the Cl end of HCl with the internuclear distance between He and Cl fixed at 2.5 Å. Thick curves represents the states with $^3\Sigma^+$ symmetry, and thin curves represents the states with the other symmetries.

Figure 4: A section of the potential energy surfaces in the case of the sideway attack of He on HCl with the internuclear distance between He and Cl fixed at 2.5 Å; the Cl atom is at the origin, the H atom is on the x-axis, and the He atom is on the y-axis. All the states shown have $^3A'$ symmetry.

Figure 5: A section of the potential energy surfaces in the case of the collinear attack of He on the H end of HCl with the internuclear distance between He and Cl fixed at 3.5 Å. Thick curves represents the states with $^3\Sigma^+$ symmetry, and thin curves represents the states with the other symmetries.

Figure 6: Mechanism of formation of the doubly-excited state $HCl^{**}(2^2\Sigma^+-4s)$. The left, middle, and right columns represent the most significant configurations of $He(2^3S_1)+HCl(X^1\Sigma^+)$, $He(1^1S_0)+HCl^{**}(3^2\Sigma^+-4s)$, and $He(1^1S_0)+HCl^{**}(2^2\Sigma^+-4s)$, respectively. The most significant configuration of the initial state, $He(2^3S_1)+HCl(X^1\Sigma^+)$, does not interact with that of the final state, $He(1^1S_0)+HCl^{**}(2^2\Sigma^+-4s)$, because

three-electron excitation is required for the transition between these configurations. The most significant configuration of $He(1^1S_0)+HCl^{**}(3^2\Sigma^+-4s)$ can interact with those of the initial and final states, and it is expected to be effective as a virtual intermediate configuration in the transition from the initial to the final state.

Figure 7: Mechanism of formation of the doubly-excited state $HCl^{**}(1^4\Pi-4p)$. The left, middle, and right columns represent the most significant configurations of $He(2^3S_1)+HCl(X^1\Sigma^+)$, $He^+ + HCl^-$, and $He(1^1S_0)+HCl^{**}(1^4\Pi-4p)$, respectively. The most significant configuration of the initial state, $He(2^3S_1)+HCl(X^1\Sigma^+)$, does not interact with that of the final state, $He(1^1S_0)+HCl^{**}(1^4\Pi-4p)$, because three-electron excitation is required for the transition between these configurations. The configuration of $He^+ + HCl^-$ can interact with those of the initial and the final states, and it is expected to be effective as a virtual intermediate configuration in the transition from the initial to final state.

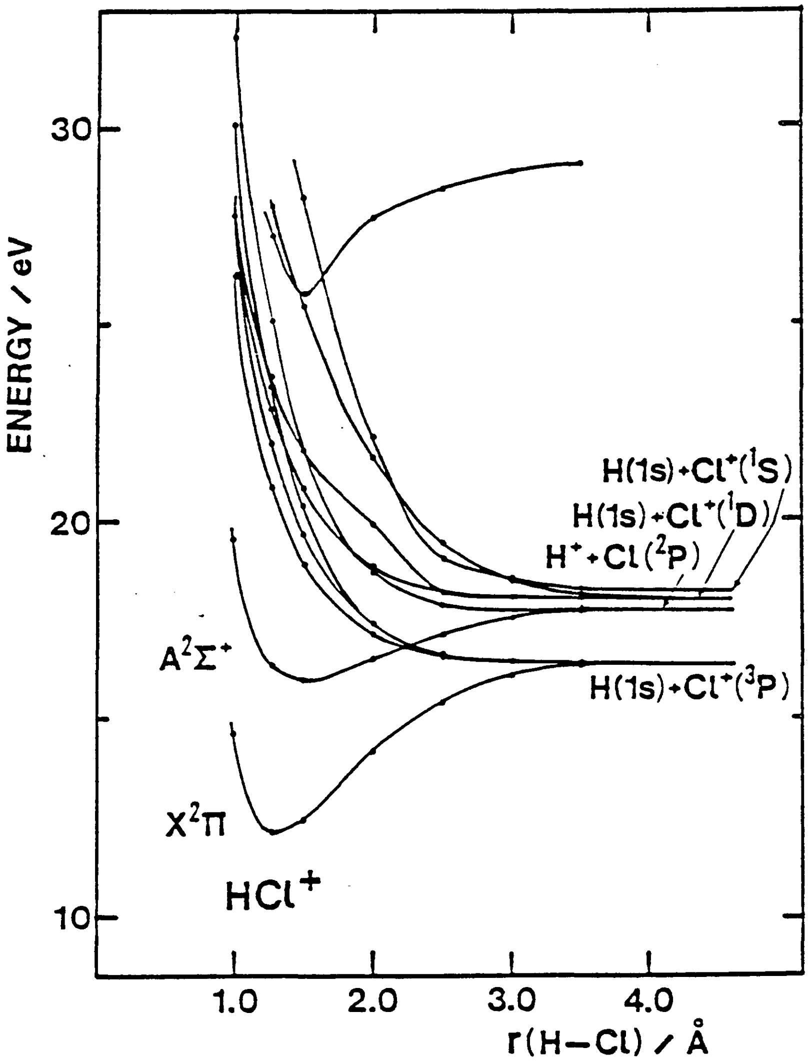
ENERGY / eV
30
20
10
1.0
2.0
3.0
4.0
r(H—Cl) / Å
H(1s)+Cl⁺(¹S)
H(1s)+Cl⁺(¹D)
H⁺+Cl(²P)
H(1s)+Cl⁺(³P)
A²Σ⁺
X²Π
HCl⁺

Figure 1

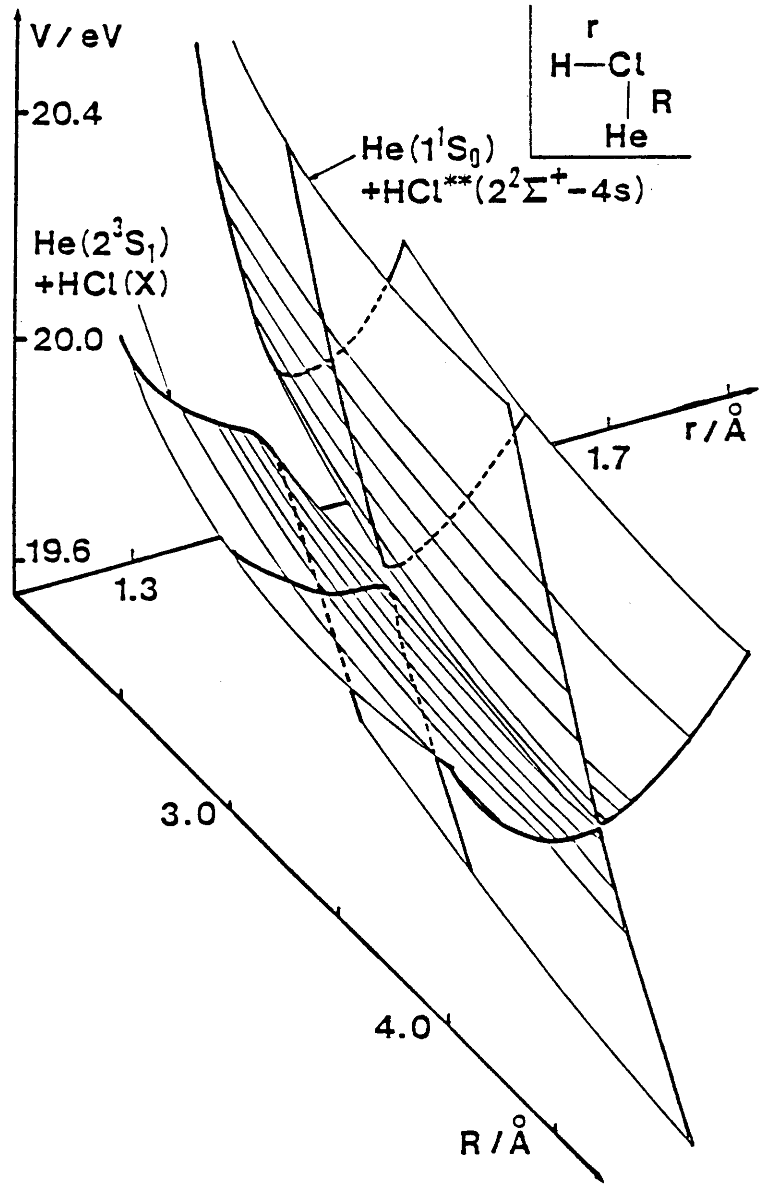

V / eV
20.4
20.0
19.6
1.3
1.7
r / Å
3.0
4.0
R / Å
r
H—Cl
R
He
He(1^{1}S$_0$)
+HCl**(2$^2\Sigma^+$−4s)
He(2^{3}S$_1$)
+HCl(X)

Figure 2

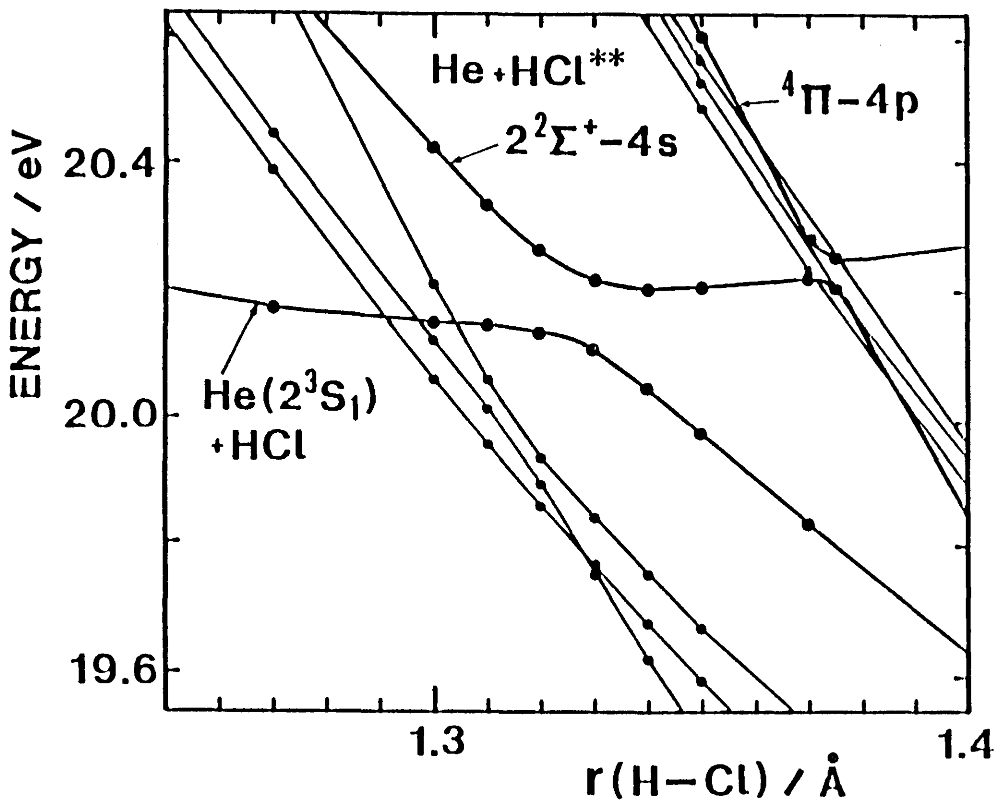
He + HCl**
$2^2\Sigma^+$-4s
$^4\Pi$-4p
He(2^3S_1) + HCl
ENERGY / eV
20.4
20.0
19.6
1.3
1.4
r(H—Cl) / Å

Figure 3

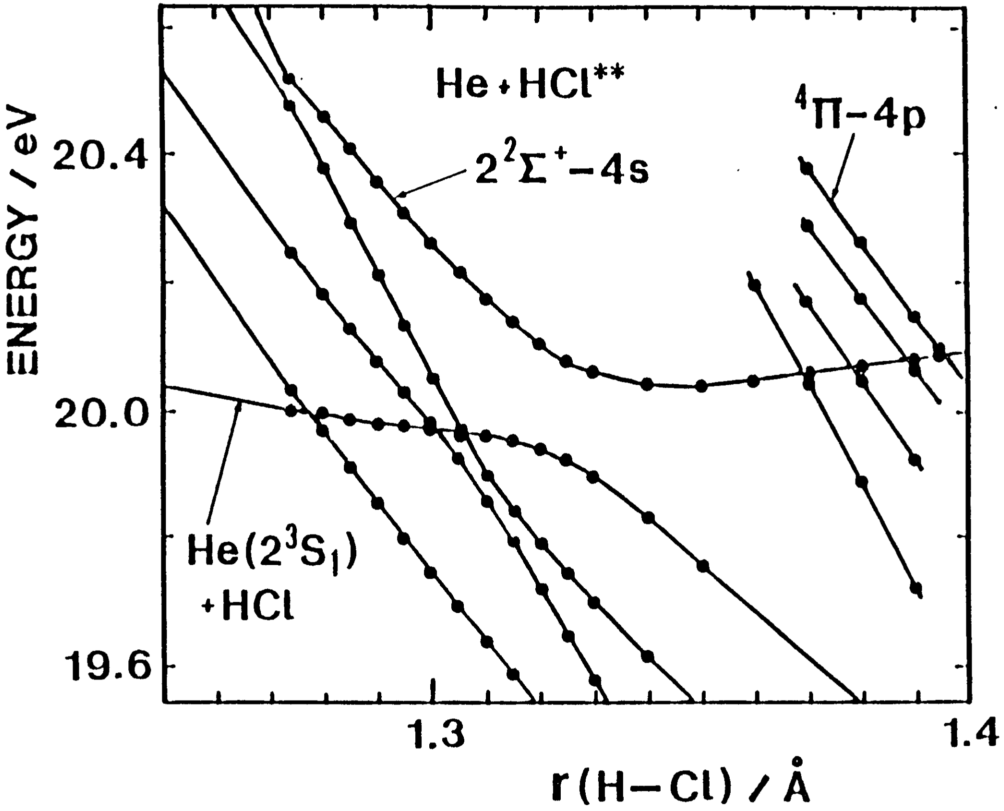
ENERGY / eV
20.4
20.0
19.6
1.3
1.4
r(H—Cl) / Å
He + HCl**
$2^2\Sigma^+$–4s
$^4\Pi$–4p
He(2^3S_1)
+HCl

Figure 4

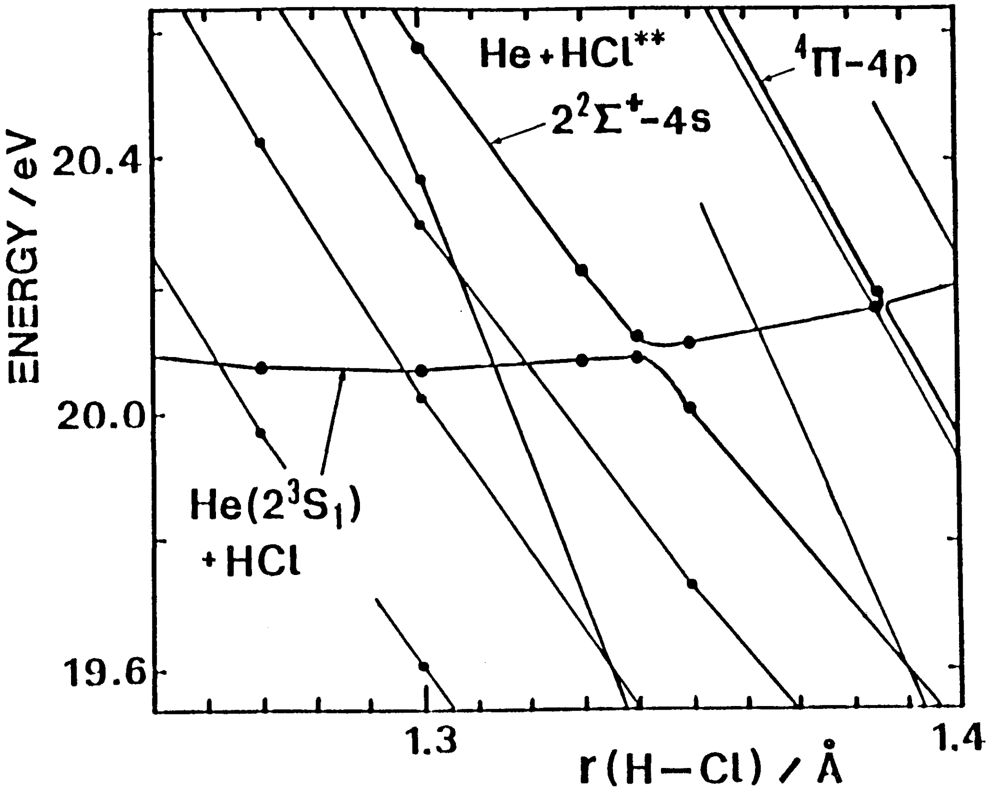

ENERGY /eV
20.4
20.0
19.6
1.3
1.4
r(H—Cl) / Å
He + HCl**
$2^2\Sigma^+$-4s
$^4\Pi$-4p
He(2^3S_1)
+HCl

Figure 5

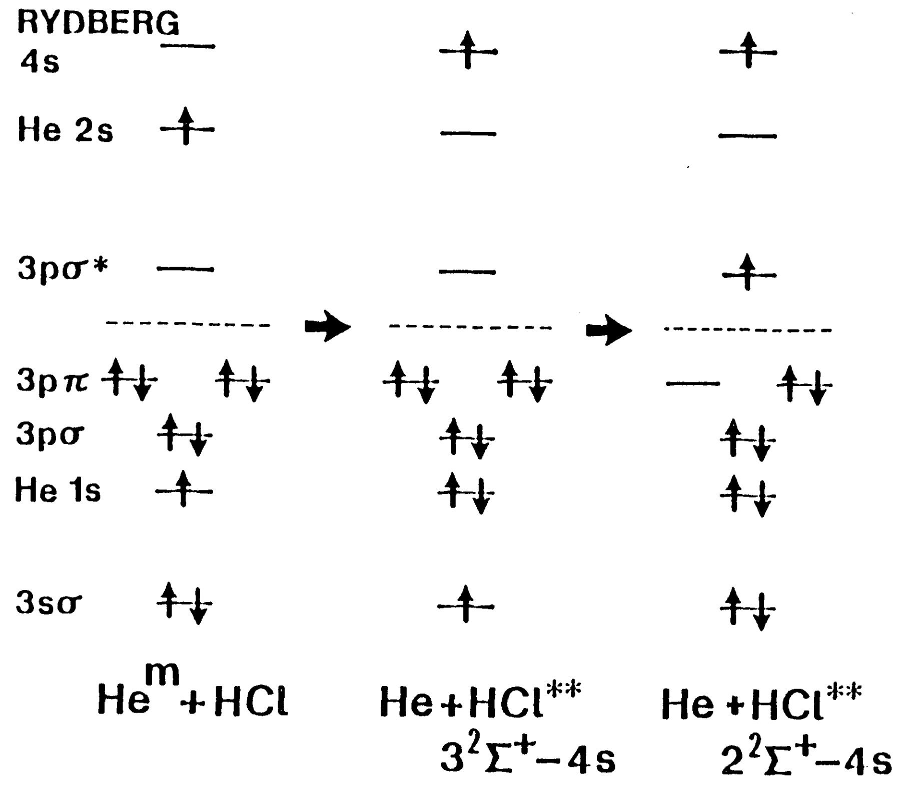
RYDBERG
4s
He 2s
3pσ*
3pπ
3pσ
He 1s
3sσ
He^m + HCl
He + HCl**
3²Σ⁺–4s
He + HCl**
2²Σ⁺–4s

Figure 6

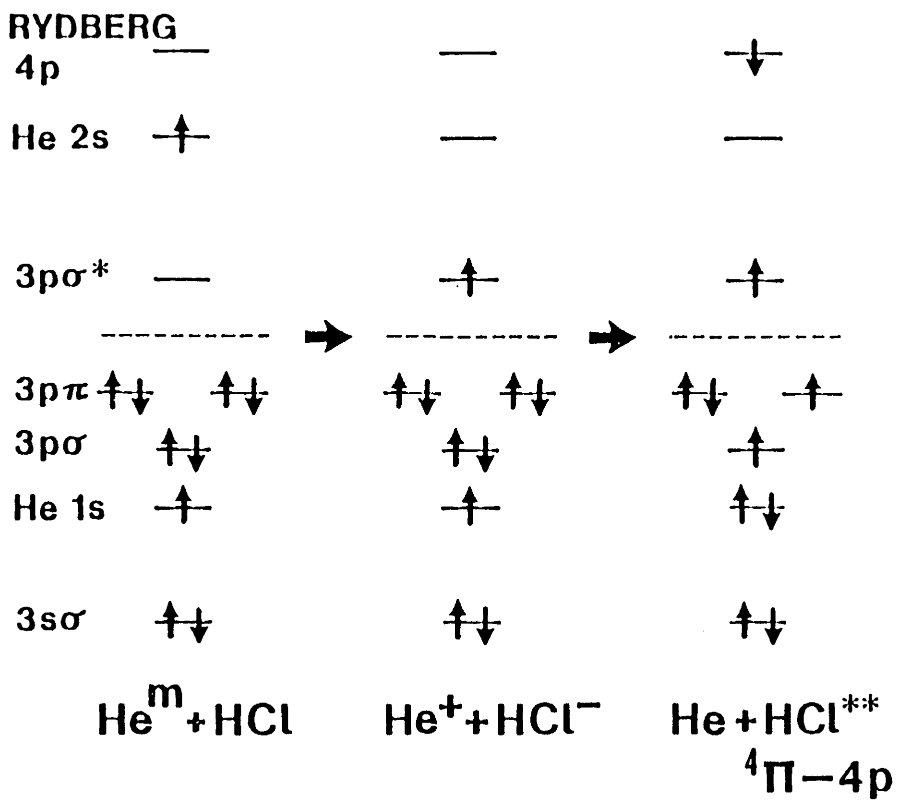

Figure 7

PART II

TIME-DEPENDENT VARIATIONAL METHOD FOR PHOTODISSOCIATION DYNAMICS

Chapter 5

Vibrational Distributions of Fragments Produced in Photodissociation

ABSTRACT

A theory of photodissociation dynamics based on TDHF (time-dependent Hatree-Fock) theory is developed. The density operator is propagated by an approximate time-evolution unitary operator, which involves two or four variational parameters. The time evolution of these variational parameters is determined from the time-dependent variational principle in accordance with the prescription presented by Tishby and Levine; it can practically be obtained from numerical integration of the TDHF equations, which requires a calculation comparable with that for integration of one or two classical trajectories. The approximate time-evolution operator is shown to be connected to a sequence of several transformations of the Wigner function in the phase space. In the limit where the Wigner function is localized in the phase space, the time evolution by this approximate time-evolution operator result in the classical mechanics of a point mass, and the variational parameters are shown to correlate to the classical dynamical variables. The formula for obtaining a vibrational-state distribution of a diatomic fragment produced in collinear dissociation of a triatomic molecule is derived; this formula is expressed explicity by the variational parameters. The vibrational distribution of the symmetric deformation of CF_3 produced in the photodissociation of CF_3I is calculated numerically by regarding CF_3I as a pseud-triatomic molecule $(F_3)-C-I$. The general trend of the distribution agrees with that calculated by the coupled channels method reported by Henning et al. by use of essentially the same Hamiltonian.

1. INTRODUCTION

A theory of molecular reaction dynamics generally requires a large amount of numerical calculation for solving the equations of motion derived from the first principle. Even if such a calculation is managedable, it does not necessarily lead us to an intuitive understanding on the essence of the dynamics. The present study aims at developing a theoretical method for obtaining approximately the final-state distributions of the reaction products with a tractable amount of numerical calculation in such a manner that some intuitive understanding on the dynamics can be obtained. In order to make the physical picture clear, it seems to be effective to trace the time evolution of the distribution function in the phase space itself, especially for discussing the final-state distributions. In the present study, the density operator, $\rho(t)$, is propagated by an approximate time-evolution unitary operator described by several variational parameters, each of which is connected to the geometrical transformation of the Wigner function (or the phase-space distribtuion function) in the phase space. The time evolution of the variational parameters is determined from the time-dependent variational principle[1-3] as in the time-dependent-Hartree-Fock (TDHF) theory on the density operator.[3]

In the present paper, attention is focused only on direct photodissociation, which can be regarded as one of the simplest cases in the dynamical processes of molecules. In direct photodissociation, the potential energy surface of the dissociative state is often so smooth that the wave packet (or the Wigner function) is hardly deformed. Therefore, it is expected to be effective to make some approximation in estimating deformation of the wave packet. Namely, the present method can be regarded as the wave packet theory based on the TDHF theory on the density operator. However, the present theory differs from the ordinary wave packet theories presented by Heller[4,5] in the following points: (1) The ansatz that the center of the wave packet moves along the classical trajectory is not necessary in the present theory, in which the equations of motion are derived purely mathematically from the variational principle and the trial function of the time evolution operator; (2) the conservation of the expectation value of the total Hamiltonian and the conservation of the entropy, $S=\mathrm{Tr}\{\rho \ln\rho\}$, are guaranteed in the present theory; (3) mixed states can be treated in completely the same manner as pure states; and (4) evolution of the Wigner function in the phase space can be represented simply by transformation in the phase space.

The variational method employed in the present theory is based on the formalism presented by Tishby and Levine.[6,7] A heuristic introduction of the approximate time evolution operator is as follows: The exact time evolution operator, U, is given by

$$U(t)=e^{-iHt}. \tag{1.1}$$

The Hamiltonian, H, can generally be expressed by a sum of the operators X_μ as

$$H=\alpha_1X_1+\alpha_2X_2+\cdots+\alpha_nX_n. \tag{1.2}$$

The U-operator in eq.(1.1) can be written as

$$U(t)=e^{-i(\alpha_1X_1+\alpha_2X_2+\cdots+\alpha_nX_n)t}$$

$$= e^{i\eta_1(t)X_1} e^{i\eta_2(t)X_2} \cdots e^{i\eta_N(t)X_N}; \tag{1.3}$$

the last expression is so called "the product representation", where $\{X_1, \ldots, X_N\}$ is the smallest Lie algebra which involves $\{X_1, \ldots, X_n\}$ as a subset and $\eta_\nu(t)$ is determined from the structure of the Lie algebra.[6] However, N becomes infinity unless the Hamiltonian is very simple. In the present approximation, the product representation of the U-operator in eq.(1.3) is approximated by a finite number of the component operators, $e^{i\eta_\nu(t)X_\nu}$; i.e.,

$$\begin{aligned} U(t) &= e^{i\eta_1(t)X_1} \cdots e^{i\eta_m(t)X_m}; \\ &\equiv \prod_{\nu=1}^{m} \exp[i\eta_\nu(t)\, X_\nu], \end{aligned} \tag{1.4}$$

by which the density operator is approximately propagated as

$$\rho(t) = U(t)\rho_0 U^{-1}(t). \tag{1.5}$$

The product representation of the U-operator (eq.(1.4)) indicates that the time evolution described by $U(t)$ can be expressed as a sequence of the transformations represented by $e^{i\eta_\nu(t)X_\nu}$ on the density operator. The approximate U-operator in eq.(1.4) can be expressed in "the sum representation" by using time-ordered exponential as

$$\begin{aligned} &\prod_{\nu=1}^{m} \exp[i\eta_\nu(t)X_\nu] \\ &\quad = T\exp[i\int_0^t dt' \sum_{\nu=1}^{m} \dot{\eta}_\nu(t')\, \tilde{X}_\nu(\eta(t'))], \end{aligned} \tag{1.6}$$

where the operator $\tilde{X}_\nu$ is defined by

$$\frac{\partial U}{\partial \eta_\nu} = i\tilde{X}_\nu U. \tag{1.7}$$

Equation (1.6) can be verified by differentiating both sides with respect to t. The operator $\tilde{X}_\nu$ can be expressed by a linear combination of operators X_ν;

$$\tilde{X}_\nu = \sum_{\mu=1}^{N} D_{\nu\mu} X_\mu \quad (\nu = 1, \ldots, m), \tag{1.8}$$

where X_ν ($\nu=1,\ldots,N(\geq m)$) forms a Lie algebra, and the matrix, $\boldsymbol{D}$, is a function of the parameters η_ν ($\nu=1,\ldots,m$).[6] From eq.(1.6), one can see that the time evolution of the system described by the approximate U-operator in eq.(1.4) is equivalent to the time evolution by a time-dependent effective Hamiltonian,

$$H_{\mathrm{eff}}(t)=-\sum_{\nu=1}^{m}\dot{\eta}_\nu(t)\tilde{X}_\nu(t)\ . \tag{1.9}$$

The equations of motion of the parameters η_ν are derived in accordance with the prescription presented by Tishby and Levine ;[6] the time evolution of η_ν is determined by the time-dependent variational principle[1,2] which leads to the Euler-Lagrange equations,

$$\mathrm{Tr}\{\tilde{X}_\nu(\frac{\mathrm{d}\rho}{\mathrm{d}t}-i[\rho,H])\}=0 \quad (\nu=1,\ldots,m). \tag{1.10}$$

This equation can be rewritten as

$$\sum_{\mu=1}^{N}D_{\nu\mu}\frac{\mathrm{d}<X_\mu>_t}{\mathrm{d}t}=i\sum_{\mu=1}^{N}D_{\nu\mu}<[H,X_\mu]>_t,\ (\nu=1,\ldots,m), \tag{1.11}$$

which is "a linear combination of Ehrenfest's theorem for X_μ". Here, $<\ >_t$ represents the expectation value evaluated by $\rho(t)$ approximately propagated by $U(t)$ in eq.(1.4). From eq.(1.10), one can obtain the equations of motion,

$$\dot{\eta}_\mu=\sum_{\nu=1}^{m}(\sigma^{-1})_{\mu\nu}\frac{\partial<H>_t}{\partial\eta_\nu} \quad (\mu=1,\ldots,m), \tag{1.12}$$

which determine the time evolution of η_ν. Here, $\sigma_{\mu\nu}$ is an antisymmetric matrix defined by

$$\sigma_{\mu\nu}=i\mathrm{Tr}\{\rho(t)[\tilde{X}_\mu,\tilde{X}_\nu]\}. \tag{1.13}$$

The time evolution of the system is obtained by solving the initial-value problem of eq.(1.12), where the initial conditions are $\eta_\mu(0)=0$ ($\mu=1,\ldots,m$), which are required from $U(t=0)=\mathbf{1}$. It is noted here that the dimension of the variational space, m, must be even in order that an antisymmetric matrix σ is invertible.

In the present paper, the approximate U-operator for photodissociation dynamics is studied, and the vibrational state distribution of a diatomic fragment produced in collinear dissociation of a triatomic molecule is formulated. The approximate U-operators employed in the present work are presented in section 2, and the nature of the approximation is discussed in sections 3 and 4. Collinear dissociation of a triatomic molecule ABC into A+BC is formulated in section 5, and the results of a numerical calculation are presented in section 6.

2. APPROXIMATE *U*-OPERATORS

In the collinear photodissociation of a triatomic molecule, in which an electronically excited molecule ABC dissociates into an atom A and a diatomic fragment BC maintaining a linear configuration, the motions of the system are described by the vibration of BC and the relative translation of A and BC. The Hamiltonian of the dissociative state is expressed as

$$H = \tfrac{1}{2}P_R^2 + \tfrac{1}{2}P_r^2 + \tfrac{1}{2}\omega^2 Q_r^2 + V(Q_R, Q_r), \tag{2.1}$$

where Q_r and Q_R represent the mass-weighted coordinates of the vibration of BC and the relative translation of A and BC respectively, P_r and P_R are the momentum operators conjugate to Q_r and Q_R respectively, and ω is the vibrational frequency of the fragment BC. The interaction, $V(Q_R, Q_r)$, between the translation and vibration is assumed to vanish in the dissociation limit, $Q_R \to \infty$. The final state is described by the vibrational quantum number, n, and the momentum of the relative translation, p, and the final-state distribution is given by $\langle np|U\rho_0 U^{-1}|np\rangle$.

The U-operator of the whole system is approximated by a product of the U-operators of the vibration and the relative translation,

$$U = U_{\mathrm{vib}} U_{\mathrm{trans}}. \tag{2.2}$$

The "one-particle U-operators," U_{vib} and U_{trans}, are expressed as

$$U_{\mathrm{vib}}=\prod_{\nu=1}^{m'}\exp[i\eta_\nu X_\nu], \tag{2.3}$$

$$U_{\mathrm{trans}}=\prod_{\nu=m'+1}^{m}\exp[i\eta_\nu X_\nu], \tag{2.4}$$

where $[X_\mu, X_\nu]=0$ if $\mu\leq m'<\nu$. In consequence, the σ-matrix is decomposed into a direct sum of the σ-matrix for U_{vib} and that for U_{trans}, and the equations of motion is partly decoupled as

$$\dot{\eta}_\mu=\sum_{\nu=1}^{m'}(\sigma^{-1})_{\mu\nu}\frac{\partial<H>_t}{\partial\eta_\nu}\quad(\mu=1,\ldots,m'), \tag{2.5}$$

$$\dot{\eta}_\mu=\sum_{\nu=m'+1}^{m}(\sigma^{-1})_{\mu\nu}\frac{\partial<H>_t}{\partial\eta_\nu}\quad(\mu=m'+1,\ldots,m). \tag{2.6}$$

The vibration and translation are coupled only through the expectation value of the Hamiltonian. Namely, the present approximation belongs to the mean-field (or Hartree) approximation. However, in the present approximation the density operator (or wave function) itself is not necessarily represented by the Hartree product such as $\rho=\rho_{\mathrm{vib}}\rho_{\mathrm{trans}}$. In eqs.(2.3) and (2.4), the set of operators $\{X_\nu\}$ should be so chosen that at least the following two conditions are satisfied: (1) The σ-matrix is invertible, and (2) the final-state distribution is independent of time. In the following subsections, several possible choices of $\{X_\nu\}$ for describing photodissociaion dynamics are presented: In subsections A and B an approximate U-operator with two parameters, which corresponds to the approximation with the minimal dimension of the variational space, is considered for describing the translation and vibration. In subsection C the dimension of the variational space of U_{vib} is extended to 4.

2.A. Approximate U-operator with two parameters for translation: frozen wave packet approximation

The simplest choice of $\{X_\nu\}$ is to choose a pair of operators canonically conjugate to each other. For describing the translation, an approximate U-

operator expressed by the position operator, Q_R, and the momentum operator, P_r,

$$U_{\rm trans}=\exp[i\eta P_R]\exp[i\xi Q_R], \tag{2.7}$$

is considered. The equations of motion for η and ξ are found to be (see Appendix A)

$$\dot{\eta}=-\frac{\partial<H>_t}{\partial\xi}=-<P>_0-\xi\ , \tag{2.8}$$

$$\dot{\xi}=\frac{\partial<H>_t}{\partial\eta}=\frac{\partial<V(Q_R-\eta,\ U_{\rm vib}^{-1}Q_rU_{\rm vib})>_0}{\partial\eta}=-<\frac{\partial V(Q_R,\ Q_r)}{\partial Q_R}>_t. \tag{2.9}$$

These equations are analogous to the canonical equations in classical mechanics; η corresponds to the position and ξ to the momentum. It should be noted that the forms of eqs.(2.8) and (2.9) always hold when one employs any pair of operators canonically conjugate to each other. The time evolution of the expectation values of P and Q is given by

$$<P>_t=<U^{-1}PU>_0=<P>_0+\xi, \tag{2.10}$$

$$<Q>_t=<U^{-1}QU>_0=<Q>_0-\eta. \tag{2.11}$$

On the other hand, the second-order moments of P and Q do not depend on time; namely,

$$<(P-<P>_t)^2>_t=<(P-<P>_0-\xi)^2>_t=<(P-<P>_0)^2>_0\ , \tag{2.12}$$

$$<(Q-<Q>_t)^2>_t=<(Q-<Q>_0+\eta)^2>_t=<(Q-<Q>_0)^2>_0\ . \tag{2.13}$$

This implies that the present approximation corresponds to the frozen wave packet approximation, as will be shown in section 3.

In the dissociation limit, the force $<\partial V/\partial Q_R>_t$ in eq.(2.9) vanishes, and the asymptotic behavior of $\eta(t)$ and $\xi(t)$ is found to be $\eta(t)\sim\eta_\infty t$ and $\xi(t)\sim\xi_\infty$, where η_∞ and ξ_∞ are constants. In this limit, the diagonal elements of the density matrix can be reduced to

$$<np\,|U\rho_0U^{-1}|np>=<np\,|e^{i\eta_\infty tP}e^{i\xi_\infty Q}\ U_{\rm vib}\rho_0U_{\rm vib}^{-1}\ e^{-i\xi_\infty Q}e^{-i\eta_\infty tP}|np>$$

$$= e^{i\eta_\infty tp} <np|e^{i\xi_\infty Q}\, U_{\mathrm{vib}}\rho_0 U_{\mathrm{vib}}^{-1}\, e^{-i\xi_\infty Q}|np> e^{-i\eta_\infty tp}$$

$$= <np|e^{i\xi_\infty Q}\, U_{\mathrm{vib}}\rho_0 U_{\mathrm{vib}}^{-1}\, e^{-i\xi_\infty Q}|np>. \qquad (2.14)$$

Namely, the momentum distribution in the final state is independent of time. On the other hand, if the U-operator in eq.(2.7) is used for U_{vib} the vibrational distribution depends on time, because η and ξ oscillate in the disocciation limit, and because P is not diagonal in the eigenstate $|n>$. Accordingly, the U-operator in eq.(2.7) is applicable to the relative translation but not to the vibration.

2.B Approximate U-operator with two parameters for vibration

In order that the vibrational distribution in the dissociation limit is independent of time, the operator X_1 in eq.(1.4) should be the number operator, N, of the harmonic oscillator defined by

$$N = \frac{1}{2\omega}(P_r^2 + \omega^2 Q_r^2). \qquad (2.15)$$

It would be desirable if a pair of operators, N and X, which satisfy $[N, X] = -i$ can be taken in the approximate U-operator as $U = \exp[i\theta N]\exp[i\zeta X]$, because the equations of motion of θ and ζ have canonical forms similar to those given in eqs.(2.8) and (2.9). However, no such operator X can exist, because N has a discrete eigenvalue spectrum.[8]

In the present paper, the U-operator defined as

$$U_{\mathrm{vib}} = \exp[i\theta N]\exp[i\zeta P_r] \qquad (2.16)$$

is considered. The equations of motion of θ and ζ are found to be (see Appendix B)

$$\dot{\theta} = -\frac{1}{\sigma_{12}}\frac{\partial <H>_t}{\partial \zeta} = -\omega - \frac{1}{\sigma_{12}}\frac{\partial <V>_t}{\partial \zeta}, \qquad (2.17)$$

$$\dot{\zeta} = \frac{1}{\sigma_{12}}\frac{\partial <H>_t}{\partial \theta} = \frac{1}{\sigma_{12}}\frac{\partial <V>_t}{\partial \theta}, \qquad (2.18)$$

where $\sigma_{12}=-\omega(<Q>_0-\zeta)$. In the dissociation limit, θ and ζ behave as $\theta(t)\sim\theta_\infty t$ and $\zeta(t)\sim\zeta_\infty$, where θ_∞ and ζ_∞ are constants. The vibrational distribution in the dissociation limit is shown to be independent of time as follows,

$$<np|U\rho_0U^{-1}|np> = <np|e^{i\theta_\infty tN}e^{i\zeta_\infty P}\ U_{\rm trans}\rho_0U_{\rm trans}^{-1}\ e^{-i\zeta_\infty P}e^{-i\theta_\infty tN}|np>$$

$$= e^{i\theta_\infty tn}<np|e^{i\zeta_\infty P}\ U_{\rm trans}\rho_0U_{\rm trans}^{-1}\ e^{-i\zeta_\infty P}|np>e^{-i\theta_\infty tn}$$

$$= <np|e^{i\zeta_\infty P}\ U_{\rm trans}\rho_0U_{\rm trans}^{-1}\ e^{-i\zeta_\infty P}|np>. \qquad (2.19)$$

The expectation values of P and Q are given by

$$<P>_t = <P>_0\cos\theta+\omega(<Q>_0-\zeta)\sin\theta, \qquad (2.20)$$

$$<Q>_t = (<Q>_0-\zeta)\cos\theta-\frac{1}{\omega}<P>_0\sin\theta. \qquad (2.21)$$

In photodissociation, where $<P>_0=0$ and $<Q>_0\neq 0$, $<P>_t$ and $<Q>_t$ oscillate, in the dissociation limit, about zero with amplitudes $\omega(<Q>_0-\zeta_\infty)$ and $<Q>_0-\zeta_\infty$, respectively. When $\zeta_\infty=<Q>_0$, the amplitudes vanish: Namely, the center of the wave packet is fixed at the origin. In such a case, σ_{12} in eqs.(2.17) and (2.18) vanishes and the equations of motion break down. However, such a case is not expected to occur in the photodissociation in which the fragment is vibrationally excited.

Another possible choice is to use the U-operator, defined by

$$U=\exp[i\theta N]\exp[i\zeta' Q], \qquad (2.22)$$

which leads to an approximation similar to that presented above; the equations of motion of θ and ζ' are found to be identical to eqs.(2.17) and (2.18), respectively, except that $\sigma_{12}=-\omega(<P>_0-\zeta')$. However, σ_{12} vanishes at $t=0$ in photodissociation, in which case $<P>_0=0$. Therefore, the U-operator in eq.(2.22) cannot be used for describing photodissociation.

2.C. Approximate U-operator with four parameters for vibration

Approximation presented in subsection 2.B is expected to be improved to some extent by introducing two additional parameters in U_{vib} defined in eq.(2.16). For describing photodissociation dynamics, the following operator is considered to be effective:

$$U_{\mathrm{vib}}=\exp[i\theta N]\exp[i\zeta P] \times \exp[-i\langle Q\rangle_0 P]\exp[i\chi Z]\exp[i\kappa W]\exp[i\langle Q\rangle_0 P], \tag{2.23}$$

where

$$Z=\frac{1}{2\omega}(P^2-\omega^2Q^2), \tag{2.24}$$

$$W=\frac{1}{2}(PQ+QP). \tag{2.25}$$

The reason for employing this U-operator is presented in section 3. The equations of motion of the variational parameters, θ, ζ, χ, and κ, are found to be (see Appendix C)

$$\dot{\theta}=-\omega-\frac{1}{\sigma_{12}\sigma_{34}}\frac{\partial\langle V\rangle_t}{\partial\zeta}, \tag{2.26}$$

$$\dot{\zeta}=-\frac{1}{\sigma_{12}\sigma_{34}}(\sigma_{34}\frac{\partial\langle V\rangle_t}{\partial\theta}+\sigma_{14}\frac{\partial\langle V\rangle_t}{\partial\chi}-\sigma_{13}\frac{\partial\langle V\rangle_t}{\partial\kappa}), \tag{2.27}$$

$$\dot{\chi}=-\frac{1}{\sigma_{12}\sigma_{34}}(-\sigma_{14}\frac{\partial\langle V\rangle_t}{\partial\zeta}+\sigma_{12}\frac{\partial\langle V\rangle_t}{\partial\kappa}), \tag{2.28}$$

$$\dot{\kappa}=-\frac{1}{\sigma_{12}\sigma_{34}}(\sigma_{13}\frac{\partial\langle V\rangle_t}{\partial\zeta}-\sigma_{12}\frac{\partial\langle V\rangle_t}{\partial\chi}), \tag{2.29}$$

where

$$\sigma_{12}=\omega(\zeta-\langle Q\rangle_0), \tag{2.30}$$

and other matrix elements, σ_{ij}, are given in eqs.(C.11)-(C.16) in Appendix C. In the dissociation limit, where all the derivatives of $\langle V\rangle_t$ vanish, the asymptotic behavior of the parameters is found to be $\theta(t)\sim\theta_\infty t$, $\zeta(t)\sim\zeta_\infty$, $\chi(t)\sim\chi_\infty$, and $\kappa(t)\sim\kappa_\infty$, where θ_∞, ζ_∞, χ_∞, and κ_∞ are constants. Therefore, the vibrational distribution in the dissociation limit is shown to be independent of time by a calculation similar to that in eq.(2.19). When $<P>_0=0$, which always holds in photodissociation, the expectation values of P and Q are given by (see eqs.(C.9) and (C.10))

$$<P>_t=\omega(<Q>_0-\zeta)\sin\theta, \tag{2.31}$$
$$<Q>_t=(<Q>_0-\zeta)\cos\theta, \tag{2.32}$$

which are identical to those of U_{vib} with two parameters (eqs.(2.20) and (2.21) with $<P>_0=0$). Therefore, σ_{12} is expected to be nonvanishing when the fragment is vibrationally excited. Since σ_{34} cannot vanish, as can be shown by eq.(C.16), the denominators in the right-hand sides of the equations of motion, eqs.(2.26)-(2.29), are expected to be nonvanishing.

3. TIME EVOLUTION OF THE WIGNER FUNCTION

In order to obtain some intuition in regard to the evolution of the system described by a given approximate U-operator, the time evolution of the Wigner function[9,10] is studied. The Wigner function, $f(p, q; t)$, is defined by

$$f(p, q; t)=\int dr\ e^{-ipr}<q+\frac{r}{2}|\rho(t)|q-\frac{r}{2}>, \tag{3.1}$$

or equivalently[10,11]

$$f(p, q; t)=\mathrm{Tr}\{\rho(P, Q; t)\ \delta(p-P, q-Q)\}, \tag{3.2}$$

where the δ function is defined by

$$\delta(p-P, q-Q)=\frac{1}{4\pi^2}\int d\alpha \int d\beta\ \exp[-i\{\alpha(p-P)+\beta(q-Q)\}]. \tag{3.3}$$

The Wigner function at t can be expressed as

$$\begin{aligned} f(p, q; t)&=\mathrm{Tr}\{U(t)\ \rho(P, Q; t=0)U^{-1}(t)\ \delta(p-P, q-Q)\} \\ &=\mathrm{Tr}\{\rho(P, Q; t=0)\ \delta(p-U^{-1}PU, q-U^{-1}QU)\}\ . \end{aligned} \tag{3.4}$$

Suppose that the U-operator transforms P and Q as

$$U^{-1}PU=u_{11}P+u_{12}Q+u_P\ , \tag{3.5}$$
$$U^{-1}QU=u_{21}P+u_{22}Q+u_Q\ , \tag{3.6}$$

where

$$u_{11}u_{22}-u_{12}u_{21}=1. \tag{3.7}$$

The U-operators which consists only of the quadratic forms of P and Q always transform P and Q as eqs.(3.5)-(3.7). The delta function can then be reduced as see (Appendix D)

$$\begin{aligned}\delta(p-U^{-1}PU,\, q-U^{-1}QU) = \delta(&u_{22}(p-u_P)-u_{12}(q-u_Q)-P,\\ &-u_{21}(p-u_P)+u_{11}(q-u_Q)-Q).\end{aligned} \tag{3.8}$$

Therefore, eq.(3.4) can be rewritten as

$$\begin{aligned}f(p,q;t)&=\mathrm{Tr}\{\rho(P,Q;t=0)\,\delta(\,u_{22}(p-u_P)-u_{12}(q-u_Q)-P,\\ &\qquad -u_{21}(p-u_P)+u_{11}(q-u_Q)-Q)\}\\ &=f(\,u_{22}(p-u_P)-u_{12}(q-u_Q),\\ &\qquad -u_{21}(p-u_P)+u_{11}(q-u_Q);\ t=0),\end{aligned} \tag{3.9}$$

or inversely,

$$f(u_{11}p+u_{12}q+u_P,\, u_{21}p+u_{22}q+u_Q;\, t)=f(p,q;t=0). \tag{3.10}$$

Equation (3.9) or (3.10) means that the evolution of the Wigner function can be represented by an affine transformation in the phase space, (p,q), which corresponds to the transformation of (P,Q) in eqs.(3.5) and (3.6).

In the case of $U_{\mathrm{trans}}=\exp[i\eta P]\exp[i\xi Q]$, the Wigner function is found to be transformed as

$$f(p,q;t)=f(p-\xi(t),\, q+\eta(t);\, t=0); \tag{3.11}$$

namely, it is the parallel translation along the p- and q-axes, represented by a coordinate transformation in the phase space,

$$p\rightarrow p'=p+\xi, \tag{3.12}$$

$$q\rightarrow q'=q-\eta. \tag{3.13}$$

In the case of $U_{\mathrm{vib}}=\exp[i\theta N]\exp[i\zeta P]$, the Wigner function at t is given by

$$f(p,q;t)=f(\,p\cos\theta-\omega q\sin\theta,\, q\cos\theta+\frac{p}{\omega}\sin\theta+\zeta;\, t=0). \tag{3.14}$$

Namely, $f(p,q;t)$ is obtained from $f(p,q;t=0)$ by the parallel translation along the q-axis,

$$p \to p' = p, \tag{3.15}$$
$$q \to q' = q - \zeta, \tag{3.16}$$

followed by a special-linear transformation,

$$p' \to p'' = p'\cos\theta + \omega q'\sin\theta, \tag{3.17}$$
$$q' \to q'' = q'\cos\theta - \frac{p'}{\omega}\sin\theta, \tag{3.18}$$

as illustrated in Figure 1. The latter transformation is equivalent to moving any point of the Wigner function along the phase flow of harmonic oscillator. When the U_{trans} and U_{vib} with two parameters are employed, only the position of the Wigner function is taken into consideration, and deformation of the Wigner function is disregarded (in the case of U_{trans}) or automatically determined by the position (in the case of U_{vib}).

On the other hand, the effect of U_{vib} with four parameters (eq.(2.23)) corresponds to the following sequence of transformations: (i) The center of $f(p, q; t=0)$ is moved to the origin of the phase space by a parallel trnaslation along the q-axis,

$$p \to p' = p, \tag{3.19}$$
$$q \to q' = q - \langle Q \rangle_0; \tag{3.20}$$

(ii) a special-linear transformation,

$$p \to p' = e^{-\kappa}p, \tag{3.21}$$
$$q \to q' = e^{\kappa}q, \tag{3.22}$$

is made as shown in Figure 2.(a); (iii) a special-linear transformation,

$$p \to p' = p\cosh\chi + \omega q\sinh\chi, \tag{3.23}$$
$$q \to q' = \frac{1}{\omega}p\sinh\chi + q\cosh\chi, \tag{3.24}$$

is made as shown in Figure 2.(b); (iv) the center of the Wigner function is replaced by that of $f(p, q; t=0)$ by the inverse transformation of eqs.(3.17) and (3.18); (v) a parallel translation,

$$p \to p' = p, \tag{3.25}$$
$$q \to q' = q - \zeta, \tag{3.26}$$

is made; and (vi) a special-linear transformation in eqs.(3.17) and (3.18) is made. In the above transformations (i)-(iv), deformation of the Wigner function is approximately taken into account by two special-linear transformations (ii) and (iii), and in the last two steps (v) and (vi), which are identical to the transformation made by U_{vib} with two parameters, the center position of the Wigner function is described.

In summary, time evolution by approximate U-operators constructed by operators quadratic in P and Q is represented by an affine transformation of the Wigner function in the phase space. Therefore, one can examine the choice of the operators to be involved in the approximate U-operator in accordance with the geometrical picture of the transformation generated by the operators.

4. LIMIT OF THE LOCALIZED WIGNER FUNCTION

The time evolution described by approximate U-operators involving two parameters is analogous to that of calssical mechanics, as can be seen from the equation of motion of the parameters and from the evolution of the Wigner function. Especially, in the limit where the Wigner function is localized in the phase sapce the time evolution by approximate U-operators is expected to result in that of the classical mechanics of a point mass. In subsection A, the equations of motion of the expectation values, $<P>_t$ and $<Q>_t$, are shown to be the canonical equations with a Hamiltonian $<H>_t$ in the case of U_{trans} and U_{vib} with two parameters. In subsection B, the variational parameters are shown to be connected to the classical variables, and their equations of motion are proved to be equivalent to that of the classical mechanics in the limit of the localized Wigner function.

4.A. Equations of motion of $<P>_t$ *and* $<Q>_t$

The time evolution of the system described by $U_{\rm trans}$ in eq.(2.7) and $U_{\rm vib}$ in eq.(2.16) can be shown to result in the classical mechanics of the point mass in the limit of the localized Wigner function. The time-derivative of $<P>_t$ propagated by an approximate U-operator,

$$U=\exp[i\eta X]\exp[i\xi Y], \tag{4.1}$$

is found to be

$$\frac{{\rm d}<P>_t}{{\rm d}t}=\dot{\eta}\frac{\partial<P>_t}{\partial\eta}+\dot{\xi}\frac{\partial<P>_t}{\partial\xi}$$

$$=(\sigma^{-1})_{12}\frac{\partial<H>_t}{\partial\xi}\frac{\partial<P>_t}{\partial\eta}+(\sigma^{-1})_{21}\frac{\partial<H>_t}{\partial\eta}\frac{\partial<P>_t}{\partial\xi}. \tag{4.2}$$

Since the expectation value $<H>_t$ can be regarded as a function of $<P>_t$ and $<Q>_t$, it follows that

$$\frac{{\rm d}<P>_t}{{\rm d}t}=-\frac{1}{\sigma_{12}}\left(\frac{\partial<H>_t}{\partial<P>_t}\frac{\partial<P>_t}{\partial\xi}+\frac{\partial<H>_t}{\partial<Q>_t}\frac{\partial<Q>_t}{\partial\xi}\right)\frac{\partial<P>_t}{\partial\eta}$$

$$+\frac{1}{\sigma_{12}}\left(\frac{\partial<H>_t}{\partial<P>_t}\frac{\partial<P>_t}{\partial\eta}+\frac{\partial<H>_t}{\partial<Q>_t}\frac{\partial<Q>_t}{\partial\eta}\right)\frac{\partial<P>_t}{\partial\xi}$$

$$=\{P,Q\}_{\eta\xi}\frac{\partial<H>_t}{\partial<Q>_t}, \tag{4.3}$$

where $\{P,Q\}_{\eta\xi}$ is the generalized Poisson bracket[6,12] defined by

$$\{P,Q\}_{\eta\xi}=-\frac{1}{\sigma_{12}}\left(\frac{\partial<P>_t}{\partial\eta}\frac{\partial<Q>_t}{\partial\xi}-\frac{\partial<P>_t}{\partial\xi}\frac{\partial<Q>_t}{\partial\eta}\right). \tag{4.4}$$

Similarly, the time-derivative of $<Q>_t$ is found to be

$$\frac{{\rm d}<Q>_t}{{\rm d}t}=\{Q,P\}_{\eta\xi}\frac{\partial<H>_t}{\partial<P>_t}. \tag{4.5}$$

If $\{P,Q\}_{\eta\xi}=1$, the equations (4.1) and (4.5) are exactly the canonical equations for $<P>_t$ and $<Q>_t$ with Hamiltonian $<H>_t$ which is a function of $<P>_t$ and $<Q>_t$. In such a case, the equations of motion, eqs.(4.1) and (4.5), are reduced to those of the classical mechanics of the point mass when the Wigner function is so localized that the equation $<P^nQ^m>_t=<P>_t^n<Q>_t^m$ holds.

For $U_{\mathrm{trans}}=\exp[i\eta P]\exp[i\xi Q]$ (eq.(2.7)), the generalized Poisson bracket $\{P,Q\}_{\eta\xi}$ is easily found to be 1 by using eqs.(2.10), (2.11), and (A.4). For $U_{\mathrm{vib}}=\exp[i\theta N]\exp[i\zeta P]$ (eq.(2.16)), it can also be shown that $\{P,Q\}_{\eta\xi}=1$ by use of eqs.(2.20), (2.21), and (B.3). Accordingly, the time evolution by approximate U-operators U_{trans} in eq.(2.7) and U_{vib} in eq.(2.16) are shown to result in that of the classical motions of the point mass when the Wigner function is localized in the phase space. Therefore, one can expect that the approximations by these U-operators are applicable to the system in which the wave packet is localized both in the coordinate and momentum spaces, such as photodissociation from the vibrationally ground state, the nuclear wave function of which is the minimal-uncertainty wave packet.

3.B Relation between the variational parameters and the classical variables

For the U-operators U_{trans} in eq.(2.7) and U_{vib} in eq.(2.16), which involve two variational parameters, the variational parameters are shown to be connected to the classical variables. In the case of $U_{\mathrm{trans}}=\exp[i\eta P]\exp[i\xi Q]$, one can see from eqs.(2.11) and (2.12) that the parameters $-\eta$ and ξ equal to the canonical variables $q(t)-q_0$ and $p(t)-p_0$, respectively, in the limit of the localized Wigner function. The equations of motion of η and ξ, eqs.(2.8) and (2.9), has the same form as the canonical equations of motion in classical mechanics.

In the case of $U_{\mathrm{vib}}=\exp[i\theta N]\exp[i\zeta P]$, the parameters θ and ζ are connected with the classical variables by

$$p(t)=p_0\cos\theta+\omega(q_0-\zeta)\sin\theta \tag{4.6}$$

$$q(t)=(q_0-\zeta)\cos\theta-\frac{1}{\omega}p_0\sin\theta \tag{4.7}$$

in the limit of localized wave packet, as is derived from eqs.(2.20) and (2.21). Equations (4.6) and (4.7) can be inverted as

$$\theta=\tan^{-1}\left(\frac{p(t)}{\omega q(t)}\right)+\sin^{-1}\left(\frac{p_0}{\{p(t)^2+\omega^2 q(t)^2\}^{1/2}}\right), \tag{4.8}$$

$$|\zeta-q_0|=\frac{1}{\omega}\{p(t)^2+\omega^2 q(t)^2-p_0^2\}^{1/2}. \tag{4.9}$$

In photodissociation, in which $p_0=0$, the above equations are reduced to

$$\theta=\tan^{-1}\left(\frac{p(t)}{\omega q(t)}\right) \tag{4.10}$$

$$|\zeta-q_0|=\frac{1}{\omega}\{p(t)^2+\omega^2 q(t)^2\}^{1/2}. \tag{4.11}$$

Namely, $\pi/2-\theta$ and $\frac{1}{2}\omega(\zeta-q_0)^2$ are equal to the angle and the action variable of the harmonic oscillator, respectively. In fact, it can be shown that the equations of motions of θ and ζ, eqs.(2.17) and (2.18), are equivalent to the classical equations of motion of θ and ζ as the classical variables defined in eqs.(4.10) and (4.11).

5. VIBRATIONAL DISTRIBUTION

In the time-dependent treatment of photodissociation, the cross section producing the vibrational state n is given by[5]

$$\begin{aligned} P(n,E_{\mathrm{ph}}) &= \epsilon E_{\mathrm{ph}}\lim_{t\to\infty}|<n\ p(n,E_{\mathrm{ph}})|U(t)|\Psi_0>|^2 \\ &= \epsilon E_{\mathrm{ph}}\lim_{t\to\infty}<n\ p(n,E_{\mathrm{ph}})|\rho(t)|n\ p(n,E_{\mathrm{ph}})>, \end{aligned} \tag{5.1}$$

where E_{ph} is the energy of photon, $|\Psi_0>$ is the nuclear wave function of the initial bound state, and ϵ is a constant related to electronic transition moment. In eq.(5.1), the final momentum p is uniquely determined from n and E_{ph} by energy conservation:

$$\frac{1}{2}p^2=E_{\mathrm{ph}}-D_0-\omega(n+1/2), \tag{5.2}$$

where D_0 is the dissociation energy. By using eq.(2.2), eq.(5.1) can be written as

$$P(n,E_{\mathrm{ph}})=\Big|\sum_{n'}\sum_{m}\int \mathrm{d}p' \; <n|U_{\mathrm{vib}}(\infty)|n'><p\,|U_{\mathrm{trans}}(\infty)|p'>$$
$$<p'\,|m><n'm|\Psi_0>\Big|^2, \qquad (5.3)$$

where $<p'\,|m>$ represents the wave function of a harmonic oscillator with an arbitrary frequency and an arbitrary equilibrium distance, which may be chosen for the convenience of the calculation of the Franck-Condon factors. By substituting the matrix element of $U_{\mathrm{trans}}(\infty)$ by eq.(A.8), eq.(5.3) is further reduced as

$$P(n,E_{\mathrm{ph}})=\Big|\sum_{n'}\sum_{m}<n|U_{\mathrm{vib}}(\infty)|n'><p'-\zeta_\infty|m><n'm|\Psi_0>\Big|^2. \qquad (5.4)$$

The matrix element of $U_{\mathrm{vib}}(\infty)$ is given in Appendices B and C for U_{vib} with two parameters and U_{vib} with four parameters, respectively.

A model Hamiltonian

$$H=\frac{1}{2}P_R^2+\frac{1}{2}(P_r^2+\omega^2Q_r^2)+V_0e^{-\alpha_RQ_R+\alpha_rQ_r} \qquad (5.5)$$

is considered. The expectation value of the interaction $<V_0e^{-\alpha_RQ_R+\alpha_rQ_r}>_t$ and its derivatives with respect to the variational parameters can be obtained in explicit forms (see Appendix E). Therefore, equations of motion of the variational parameters can be written explicitly. Accordingly, the procedure for obtaining the vibrational distribution is as follows: calculation of the Franck-Condon factor in eq.(5.4), integration of the equations of motion of the variational parameters, calculation of the U-matrix element, and then, multiplication of the matrices in eq.(5.4).

6. EXAMPLE

A numerical calculation was made on the photodissociation of $CF_3I(\tilde{X})$[13] in the vibrationally ground state,

$$CF_3I \rightarrow CF_3(\tilde{X})+I(^2P_{1/2}), \qquad (6.1)$$

by a collinear model, in which the symmetric derformation of CF_3 and the C-I stretching motions are taken into consideration. The results are compared with the exact one reported by Henning et al.[14] by a coupled channels method, in which essentially the same Hamiltonian is employed. Since the aim of the present calculation is to test the validity of the present approximation, the Hamiltonian used may not be sufficiently realistic to explain the experimental results; for example, the excitation of the stretching and degenerate deformation modes of CF_3 are left out, and non-adiabatic transitions to the other potential surfaces are ignored.

The wave function of the bound state, $CF_3I(\tilde{X})$, is approximated by that of the two-dimensional harmonic oscillator whose frequencies, $\bar{\omega}_1$ and $\bar{\omega}_2$, and normal coordinates are calculated from the potential surface of $CF_3(\tilde{X})$ employed by Henning et al.[14] The frequences are $\bar{\omega}_1/2\pi c = 745\mathrm{cm}^{-1}$ and $\bar{\omega}_2/2\pi c = 287\mathrm{cm}^{-1}$, the corresponding spectroscopic values being $\bar{\omega}_1/2\pi c = 741\mathrm{cm}^{-1}$ (ν_2: CF_3 symmetric deformation) and $\bar{\omega}_2/2\pi c = 286\mathrm{cm}^{-1}$ (ν_4: C-I stretching).[15] The transformation between the normal coordinates of CF_3I, (Q_1, Q_2), and the mass-weighted Jacobi coordinates, (Q_r, Q_R), defined in section 2, is found to be

$$Q_r = +0.98494\, Q_1 + 0.17290\, Q_2 + 18.2979, \tag{6.2}$$

$$Q_R = -0.17290\, Q_1 + 0.98494\, Q_2 + 1362.77, \tag{6.3}$$

in atomic units.

Following Henning et al.[14], the functional form of eq.(5.5) is used for the Hamiltonian of the dissociative state; the interaction is assumed to be the repulsion between C and I atoms: $V = V_0 e^{-\alpha R_{C-I}}$. The values of the constants are as follows: $\omega/2\pi c = 705\mathrm{cm}^{-1}$, $V_0 = 1945.0$, and $\alpha = 2.2$. These values lead to $\alpha_R = 7.707 \times 10^{-3}\, a_0^{-1}$ and $\alpha_r = 0.01309\, a_0^{-1}$. The dissociation energy, D_0, is $0.1176\, e^2 a_0^{-1}$. The expectation value, $\langle H \rangle_t$, is calculated by the formula given in Appendix E.

In the calculation of the Franck-Condon factor, eqs.(6.2) and (6.3) are approximated by

$$Q_r = Q_1 + 18.2979, \tag{6.4}$$
$$Q_R = Q_2 + 1362.77. \tag{6.5}$$

Then, it follows that

$$\begin{aligned} <nm|\Psi_0> &= \int dQ_r \int dQ_R \ \psi_n^{(r)}(Q_r)\ \psi_m^{(R)}(Q_R)\ \psi_0^{(1)}(Q_1)\ \psi_0^{(2)}(Q_2) \\ &\approx \int dQ_r \ \psi_n^{(r)}(Q_r)\ \psi_0^{(1)}(Q_r + d_r) \\ &\quad \int dQ_R \ \psi_m^{(R)}(Q_R)\ \psi_0^{(2)}(Q_R + d_R). \end{aligned} \tag{6.6}$$

The equilibrium distance and the frequency of the harmonic oscillator wave function $\psi_m^{(R)}$, which can be chosen arbitrarily (see eq.(5.3)), are set equal to those of $\psi_0^{(2)}$; then, the second integral in eq.(6.6) becomes δ_{m0}. The first integral is estimated by using the recursion formula.[16]

The equations of motion of the variational parameters is integrated numerically by means of the Runge-Kutta method. The U-matrix elements are calculated by use of the expression given in Appendices B and C.

The results of the calculation by using $U_{\rm trans}$ in eq.(2.7) and $U_{\rm vib}$ with two parameters (eq.(2.16)) are shown in Figure 3, in which the exact solution by the coupled channels method reported by Henning et al.[14] is also shown. The peak of the vibrational distribution is shifted towards larger n when the photon energy is increased; the position of the peak is well reproduced by the present calculation, though the distributions are wider than the exact ones. This trend is reasonable because the present approximation, in which the U-operators with two parameters are employed, corresponds to the "frozen" wave packet approximation, and the deformation of the Wigner function is not fully taken into account.

In order to make a more severe test, a numerical calculation is performed by use of a more complicated potential, presented also by Hennning et al.[14]; namely, the harmonic potential in eq.(5.9), $\frac{1}{2}\omega^2 Q_r^2$, is replaced by the potential in which the equilibrium distance and the frequency depend on the C-I distance:

$$H=\frac{1}{2}P_R^2+\frac{1}{2}P_r^2+\frac{1}{2}Z(Q_R)^2\omega^2(Q_r-\Delta(Q_R))^2+V_0e^{-\alpha_RQ_R+\alpha_rQ_r}, \qquad (6.7)$$

where the functional form of $Z(Q_R)$ and $\Delta(Q_R)$ are given in eqs.(F.1) and (F.2). The expectation value of the Hamiltonian is given in Appendix F, where an approximation is made in evaluating the expectation values of $Z(Q_R)$ and $\Delta(Q_R)$. The results are shown in Figure 4. The position of the peak is reproduced, but the distribution is narrower than the exact one. The distribution calculated by U_{vib} with four parameters is wider, i.e., closer to the exact one than that calculated by U_{vib} with two parameters; the level of approximation is indeed improved by extension of the variational space. The remaining desagreement can be ascribed to the limitation of the frozen wave packet approximation for the translation and the mean-field approximation.

APPENDICES

APPPENDIX A: EQUATIONS OF MOTION AND MATRIX ELEMENT FOR U_{trans}

One can obtain $\tilde{P}$ by differentiating U by η,

$$\frac{\partial U}{\partial\eta}=iPe^{i\eta P}e^{i\xi Q}=iPU. \qquad (A.1)$$

By definition (eq.(1.7)), it is obvious that $\tilde{P}=P$. Differentiation by ξ gives

$$\frac{\partial U}{\partial\xi}=ie^{i\eta P}Qe^{i\xi Q}=i(Q+\eta)e^{i\eta P}e^{i\xi Q}; \qquad (A.2)$$

namely, $\tilde{Q}=Q+\eta$. Here, the last equality in eq.(A.2) can be derived from the Kubo identity

$$[X,e^Y]=\int_0^1 e^{sY}[X,Y]e^{-sY}\,\mathrm{d}s\;e^Y. \qquad (A.3)$$

Then, the σ-matrix is given by

$$\sigma_{12} = i<[\tilde{P}, \tilde{Q}]>_t = i<[P, Q+\eta]>_t = 1. \tag{A.4}$$

The transformation, $U^{-1}PU$ and $U^{-1}QU$, can be calculated by using the Baker-Hausdorf expansion,

$$e^X Y e^{-X} = e^{ad\,X} Y \equiv \sum_{n=0}^{\infty} \frac{1}{n!}(ad\,X)^n Y, \tag{A.5}$$

where $(ad\,X)Y \equiv [X, Y]$. For example, $U^{-1}PU$ is obtained as

$$\begin{aligned} U^{-1}PU &= e^{-i\,ad\,\xi Q} e^{-i\,ad\,\eta P} P \\ &= e^{-i\,ad\,\xi Q} P \\ &= P + \xi. \end{aligned} \tag{A.6}$$

The expectation value of the kinetic energy operator is given by

$$\begin{aligned} <\frac{1}{2}P^2>_t &= \mathrm{Tr}\{U\rho_0 U^{-1}\,\frac{1}{2}P^2\} \\ &= \mathrm{Tr}\{\rho_0\, U^{-1}\frac{1}{2}P^2 U\} \\ &= \mathrm{Tr}\{\rho_0\,\frac{1}{2}(U^{-1}PU)^2\} \\ &= \frac{1}{2}<(P+\xi)^2>_0 = \frac{1}{2}<P^2>_0 + \xi<P>_0 + \frac{1}{2}\xi^2. \end{aligned} \tag{A.7}$$

Accordingly, one obtains the equations of motion of η and ξ, eqs.(2.8) and (2.9).

On the other hand, the matrix element of U_{trans} in the momentum representation is obtained, by recalling that the effect of the operator $e^{i\xi Q}$ is a shift of the momentum by ξ;

$$<p'|e^{i\eta P} e^{i\xi Q}|p> = e^{i\eta p'}\delta(p - p' + \xi). \tag{A.8}$$

APPENDIX B: EQUATIONS OF MOTION AND MATRIX ELEMENT FOR U_{vib} WITH TWO PARAMETERS

The operator $\tilde{N}$ is given by $\tilde{N} = N$. Differentiation of U_{vib} (eq.(2.16)) by ζ leads to

$$\frac{\partial U_{\mathrm{vib}}}{\partial \zeta} = i e^{i\theta N} P e^{i\zeta P} \equiv i\tilde{P} e^{i\theta N} e^{i\zeta P}. \tag{B.1}$$

It follows that

$$\tilde{P}=e^{i\theta N}Pe^{-i\theta N}=P\cos\theta-\omega Q\sin\theta. \tag{B.2}$$

The σ-matrix is obtained as follows:

$$\begin{aligned}\sigma_{12}&=i<[\tilde{N},\tilde{P}]>_t\\ &=i<U^{-1}[N,e^{i\theta ad\,N}P]U>_0\\ &=i<e^{-i\zeta ad\,P}e^{-i\theta ad\,N}[N,e^{i\theta ad\,N}P]>_0\\ &=i<[e^{-i\zeta ad\,P}N,P]>_0\\ &=i<[N-\zeta\omega Q+\frac{1}{2}\omega\zeta^2,P]>_0\\ &=-\omega<Q-\zeta>_0\end{aligned} \tag{B.3}$$

The expectation value of N is given by

$$\begin{aligned}<N>_t&=<U^{-1}NU>_0=<e^{-i\zeta ad\,P}N>_0\\ &=<N>_0-\zeta\omega<Q>_0+\frac{1}{2}\zeta^2\end{aligned} \tag{B.4}$$

Accordingly, the equations of motion, eqs.(2.17) and (2.18), are obtained.

On the other hand, the matrix element of U_{vib} is given by

$$\begin{aligned}<n|U_{\text{vib}}|m>&=<n|e^{i\theta N}e^{i\zeta P}|m>\\ &=e^{i\theta n}<n|e^{i\zeta P}|m>.\end{aligned} \tag{B.5}$$

The operator P can be expressed by anihilation and creation operators, a and a^+, as

$$P=i(\frac{\omega}{2})^{½}(a^+-a). \tag{B.6}$$

By using the above expression, it follows that

$$\begin{aligned}<n|e^{i\zeta P}|m> &= <n|e^{-\zeta(\omega/2)^{½}(a^+-a)}|m>\\ &= <n|e^{-\zeta(\omega/2)^{½}a^+}e^{\zeta(\omega/2)^{½}a}e^{-(\omega/4)\zeta^2}|m>\\ &= e^{-(\omega/4)\zeta^2}\sum_{l=0}^{\min(n,m)}<n|e^{-\zeta(\omega/2)^{½}a^+}|l><l|e^{\zeta(\omega/2)^{½}a}|m>\\ &= e^{-(\omega/4)\zeta^2}\sum_{l=0}^{\min(n,m)}\frac{\{-\zeta(\omega/2)^{½}\}^{n-l}}{(n-l)!}(\frac{n!}{l!})^{½}\frac{\{\zeta(\omega/2)^{½}\}^{m-l}}{(m-l)!}(\frac{m!}{l!})^{½}\\ &= (n!m!)^{½}e^{-(\omega/2)\zeta^2}\sum_{l=0}^{\min(n,m)}\frac{\{-\zeta(\omega/2)^{½}\}^{n-l}\{\zeta(\omega/2)^{½}\}^{m-l}}{(n-l)!(m-l)!l!}.\end{aligned} \tag{B.7}$$

Namely, the matrix element is given by a polynomial of ζ.

This U-matrix element can be shown to have a functional form similar to that of the forced harmonic oscillator. For example, the squared modulus of the matrix element $<n|U|0>$ is given by

$$|<n|U|0>|^2=\frac{1}{n!}(\frac{\omega}{2}\zeta^2)^n e^{-\frac{\omega}{2}\zeta^2}, \tag{B.8}$$

which equals to $|<n|U|0>|^2$ of the forced harmonic oscillator with a mean vibrational quantum $\bar{n}=½\omega\zeta^2$. However, the present approximation is not completely equivalent to the forced harmonic osicllator, because the effective Hamiltonian in eq.(1.9) is found to be

$$H_{\rm eff}=-\dot{\theta}N-\dot{\zeta}(P\cos\theta-\omega Q\sin\theta), \tag{B.9}$$

which is different from the Hamiltonian of the forced harmonc oscillator in that $H_{\rm eff}$ involves the operator P.

APPENDIX C: EQUATIONS OF MOTION AND MATRIX ELEMENT FOR U_{vib} WITH FOUR PARAMETERS

The effects of the U-operator on P and Q are considered first. Each component of the U-operator transforms P and Q as follows:

$$e^{-i\,ad\,\theta N}P \;=\; P\cos\theta+\omega Q\sin\theta, \tag{C.1}$$
$$e^{-i\,ad\,\theta N}Q \;=\; -\frac{1}{\omega}P\sin\theta+Q\cos\theta, \tag{C.2}$$
$$e^{-i\,ad\,\zeta P}P=P, \tag{C.3}$$
$$e^{-i\,ad\,\zeta P}Q=Q-\zeta, \tag{C.4}$$
$$e^{-i\,ad\,\chi Z}P=P\cosh\chi-\omega Q\sinh\chi, \tag{C.5}$$
$$e^{-i\,ad\,\chi Z}Q=-\frac{1}{\omega}P\sinh\chi+Q\cosh\chi, \tag{C.6}$$
$$e^{-i\,ad\,\kappa W}P=e^{\kappa}P, \tag{C.7}$$
$$e^{-i\,ad\,\kappa W}Q=e^{-\kappa}Q, \tag{C.8}$$

which are obtained by using the Baker-Hausdorf expansion (eq.(A.5)). The effect of the whole U-operator on P and Q are given by

$$\begin{aligned}U^{-1}PU =&Pe^{\kappa}(\cos\theta\cosh\chi-\sin\theta\sinh\chi)\\ &-\omega(Q-<Q>_0)e^{-\kappa}(\cos\theta\sinh\chi-\sin\theta\cosh\chi)\end{aligned}$$

$$-\omega(\zeta-\langle Q\rangle_0)\sin\theta, \tag{C.9}$$

$$\begin{aligned} U^{-1}QU =& (Q-\langle Q\rangle_0)e^{-\kappa}(\cos\theta\cosh\chi+\sin\theta\sinh\chi) \\ &-\frac{1}{\omega}Pe^{\kappa}(\cos\theta\sinh\chi+\sin\theta\cosh\chi) \\ &-(\zeta-\langle Q\rangle_0)\cos\theta. \end{aligned} \tag{C.10}$$

The σ-matrix elements are given by

$$\sigma_{12}=\omega(\zeta-\langle Q\rangle_0), \tag{C.11}$$

$$\sigma_{13}=\frac{1}{\omega}\{\langle P^2\rangle_0 e^{2\kappa}+\omega^2\langle\bar{Q}^2\rangle_0 e^{-2\kappa}\}\sinh 2\chi, \tag{C.12}$$

$$\sigma_{14}=\frac{1}{\omega}\{\langle P^2\rangle_0 e^{2\kappa}-\omega^2\langle\bar{Q}^2\rangle_0 e^{-2\kappa}\}\cosh 2\chi, \tag{C.13}$$

$$\sigma_{23}=0, \tag{C.14}$$

$$\sigma_{24}=0, \tag{C.15}$$

$$\sigma_{34}=\frac{1}{\omega}\{\langle P^2\rangle_0 e^{2\kappa}+\omega^2\langle\bar{Q}^2\rangle_0 e^{-2\kappa}\}, \tag{C.16}$$

where $\bar{Q}\equiv Q-\langle Q\rangle_0$ and the initial condition of photodissociation, $\langle P\rangle_0 = \langle PQ+QP\rangle_0 =0$, has been used; the condition $\langle PQ+QP\rangle_0 =0$ holds when the nuclear wave function of the bound state is a product of those of harmonic oscillator. The expectation value of N is given by

$$\begin{aligned} \langle N\rangle_t=& \frac{1}{2\omega}\{\langle P^2\rangle_0 e^{2\kappa}+\omega^2\langle\bar{Q}^2\rangle_0 e^{-2\kappa}\}\cosh 2\chi \\ &+\frac{\omega}{2}(\zeta-\langle Q\rangle_0)^2. \end{aligned} \tag{C.17}$$

The equations of motion are obtained from eqs.(C.9)-(C.17) as eqs.(2.26)-(2.29).

In the calculation of the matrix element of U_{vib} in eq.(2.23), the matrix element of each component, $e^{i\zeta P}$, $e^{i\chi Z}$, and $e^{i\kappa W}$, are calculated from the analytical expression, and the matrix element of the whole U_{vib} is obtained by numerical multiplication of each component matrix. The analytical expressions of the matrix elements of $e^{i\chi Z}$ and $e^{i\kappa W}$ are obtained as follows: The matrix element of the former is considered first. By use of the anihilation and creation operators, $e^{i\chi Z}$ is expressed as

$$e^{i\chi Z}=e^{-i(\chi/2)(aa+a^+a^+)}. \tag{C.18}$$

The normal product representation, in which the anihilation operator is collected on the right-hand side of the operator, the right-hand side of the above equation is obtained by the following procedure: The normal product representation of the operator

$$U=e^{\alpha s(aa+a^+a^+)}, \tag{C.19}$$

is expected to have the form

$$V=e^{A(s)}e^{B(s)a^+a^+}e^{C(s)a^+a}e^{D(s)aa}. \tag{C.20}$$

The derivatives with respect to the parameter s of U and V are given by

$$\frac{\mathrm{d}U}{\mathrm{d}s}=\alpha(aa+a^+a^+)U, \tag{C.21}$$

and

$$\begin{aligned}\frac{\mathrm{d}V}{\mathrm{d}s}=[&\frac{\mathrm{d}A}{\mathrm{d}s}+\frac{\mathrm{d}B}{\mathrm{d}s}a^+a^++\frac{\mathrm{d}C}{\mathrm{d}s}\{a^+a-2B(s)a^+a^+\}\\ &+\frac{\mathrm{d}D}{\mathrm{d}s}e^{-2C(s)}\{aa-4B(s)(a^+a+\frac{1}{2})+4B(s)^2a^+a^+\}]V.\end{aligned} \tag{C.22}$$

If $A(0)=B(0)=C(0)=D(0)=0$ and $\alpha(aa+a^+a^+)$ is equal to the interior of the bracket in eq.(C.22), the operator V is equal to the operator U. Equating $\alpha(aa+a^+a^+)$ to the interior of the bracket in eq.(C.22), one obtains

$$\dot{A}-2\dot{D}Be^{-2C}=0, \tag{C.23}$$
$$\dot{C}-4\dot{D}Be^{-2C}=0, \tag{C.24}$$
$$\dot{D}e^{-2C}=\alpha, \tag{C.25}$$
$$\dot{B}-2\dot{C}B+4B^2\dot{D}e^{-2C}=\alpha, \tag{C.26}$$

where the dot represents the derivative with respect to s. The solution of the above differential equations under the initial conditions that $A(0)=B(0)=C(0)=D(0)=0$ are given by

$$A=-\frac{1}{2}\ln|\cos(2\alpha s)|, \tag{C.27}$$
$$B=\frac{1}{2}\tan(2\alpha s), \tag{C.28}$$
$$C=\frac{1}{2}A, \tag{C.29}$$
$$D=B. \tag{C.30}$$

By putting $s=1$ and $\alpha=-(i/2)\chi$, one obtains

$$e^{i\chi Z} = e^{-(i/2)\tanh\chi\cdot a^+a^+} e^{-\ln(\cos\chi)\cdot(a^+a+½)} \\ e^{-(i/2)\tanh\chi\cdot aa}. \tag{C.31}$$

The matrix element can be obtained as

$$\begin{aligned} &<n|e^{i\chi Z}|m> \\ &= \sum_{n'=0}^{\min(n,m)} <n|e^{Ba^+a^+}|n'> e^{C(n'+½)} <n'|e^{Baa}|m> \\ &= (m!n!)^{½} e^{C/2} B^{(m+n)/2} \sum_{n'=0}^{\min(n,m)} \frac{(e^C/B)^{n'}}{n'!} \,/\, \{(\frac{n-n'}{2})!(\frac{m-n'}{2})!\}, \end{aligned} \tag{C.32}$$

where the matrix element is nonvanishing only if m and n are both even or odd, and the summation over n' is taken for even (odd) n' when m and n are even (odd).

On the other hand, the normal product representation of the operator

$$e^{i\kappa W} = e^{\kappa(aa-a^+a^+)} \tag{C.33}$$

is given by

$$e^{\kappa(aa-a^+a^+)} = e^{B'a^+a^+} e^{C'(a^+a+½)} e^{-B'aa}, \tag{C.34}$$

where

$$B' = -\frac{1}{2}\tanh(2\kappa), \tag{C.35}$$

$$C' = -\ln\{\cosh(2\kappa)\}. \tag{C.36}$$

The matrix element is given by

$$\begin{aligned} &<n|e^{i\kappa W}|m> \\ &= (m!n!)^{½} e^{C'/2} B'^{(m+n)/2} \\ &\sum_{n'=0}^{\min(n,m)} (-1)^{(m-n')/2} \frac{(e^{C'}/B')^{n'}}{n'!} \,/\, \{(\frac{n-n'}{2})!(\frac{m-n'}{2})!\}, \end{aligned} \tag{C.37}$$

where the matrix element vanishes unless m and n are both even or odd, and the summation over n' is taken for even (odd) n' when m and n are even (odd).

APPENDIX D: A PROOF OF EQ.(3.8).

By definition, the left hand side of eq.(3.8) is expressed as

$$\begin{aligned}
&\delta(p-U^{-1}PU,\ q-U^{-1}QU)\\
&=\frac{1}{4\pi^2}\int d\alpha\int d\beta \exp[-i\{\alpha(p-u_{11}P-u_{12}Q-u_P)\\
&\qquad\qquad\qquad +\beta(q-u_{21}P-u_{22}Q-u_Q)\}]\\
&=\frac{1}{4\pi^2}\int d\alpha\int d\beta \exp[-i\{(p-u_P)\alpha-P(u_{11}\alpha+u_{21}\beta)\\
&\qquad\qquad\qquad +(q-u_Q)\beta-Q(u_{12}\alpha+u_{22}\beta)\}].
\end{aligned}\tag{D.1}$$

Changes of the integration variables,

$$\alpha'=u_{11}\alpha+u_{21}\beta,\tag{D.2}$$

$$\beta'=u_{12}\alpha+u_{22}\beta,\tag{D.3}$$

lead to

$$\begin{aligned}
&\delta(p-U^{-1}PU,\ q-U^{-1}QU)\\
&=\frac{1}{4\pi^2}\int d\alpha'\int d\beta' \exp[-i\{(p-u_P)(u_{22}\alpha'-u_{21}\beta')-P\alpha'\\
&\qquad\qquad\qquad +(q-u_Q)(-u_{12}\alpha'+u_{11}\beta')-Q\beta'\}]\\
&=\frac{1}{4\pi^2}\int d\alpha'\int d\beta' \exp[-i(\alpha'\{u_{22}(p-u_P)-u_{12}(q-u_Q)-P\}\\
&\qquad\qquad\qquad +\beta'\{-u_{21}(p-u_P)+u_{11}(q-u_Q)-Q\})]\\
&=\delta(u_{22}(p-u_P)-u_{12}(q-u_Q)-P,\\
&\quad -u_{21}(p-u_P)+u_{11}(q-u_Q)-Q),
\end{aligned}\tag{D.4}$$

which is to be proved.

APPENDIX E: THE EXPECTATION VALUE OF THE HAMILTONIAN IN EQ.(5.5)

The expectation values of the kinetic energy operator, $\frac{1}{2}P_R^2$, and the Hamiltonian of harmonic oscillator, ωN, are given in Appendices A, B, and C. The expectation value of the interaction is given by

$$\begin{aligned}
<V>_t&=<U^{-1}e^{-\alpha_R Q_R}e^{\alpha_r Q_r}U>_t\\
&=<\exp[-\alpha_R U_{\rm trans}^{-1}Q_r U_{\rm trans}+\alpha_r U_{\rm vib}^{-1}Q_r U_{\rm vib}]>_0.
\end{aligned}\tag{E.1}$$

The transformation of Q_r is given by

$$U_{\rm trans}^{-1}Q_r U_{\rm trans}=Q_r-\eta,\tag{E.2}$$

and the transformation of Q_r by $U_{\rm vib}$ with two parameters and $U_{\rm vib}$ with four parameters can be expressed as

$$U_{\mathrm{vib}}^{-1}Q_rU_{\mathrm{vib}}=u_{21}P_r+u_{22}Q_r+u_Q. \tag{E.3}$$

Substisution of eqs.(E.2) and (E.3) into eq.(E.1) leads to

$$<V>_t=<\exp[-\alpha_RQ_R+\alpha_r(u_{21}P_r+u_{22}Q_r)]>_0 \exp[\alpha_R\eta+\alpha_ru_Q]. \tag{E.4}$$

For the initial wave function, by which the expectation value $< >_0$ is calculated, the ground state of a two-dimensional harmonic oscillator is considered. The normal coordinate of the bound state (Q_1,Q_2) and the Jacobi coordinates (Q_r,Q_R) are connected by an orthogonal transformation,

$$Q_r=s_{11}Q_1+s_{12}Q_2+d_r, \tag{E.5}$$

$$Q_R=s_{21}Q_1+s_{22}Q_2+d_R. \tag{E.6}$$

It follows that

$$P_r=s_{11}P_1+s_{21}P_2, \tag{E.7}$$

$$P_R=s_{12}P_1+s_{22}P_2, \tag{E.8}$$

where P_1 and P_2 are the momentum operator canonically conjugate to Q_1 and Q_2 respectively. Then, eq.(E.4) can be reduced to

$$<V>_t=<e^{A_1P_1+B_1Q_1}e^{A_2P_2+B_2Q_2}>_0e^{\alpha_r(u_Q+u_{22}d_r)+\alpha_R(\eta-d_R)}, \tag{E.9}$$

where

$$A_1=\alpha_ru_{21}s_{11}, \tag{E.10}$$

$$A_2=\alpha_ru_{21}s_{21}, \tag{E.11}$$

$$B_1=\alpha_ru_{22}s_{11}-\alpha_Rs_{21}, \tag{E.12}$$

$$B_2=\alpha_ru_{22}s_{12}-\alpha_Rs_{22}. \tag{E.13}$$

When the normal frequencies of the bound state harmonic oscillator are $\bar{\omega}_1$ and $\bar{\omega}_2$, eq.(E.9) can be reduced to

$$\begin{aligned}<V>_t=&\exp[\frac{1}{4\bar{\omega}_1}(B_1^2+\bar{\omega}_1^2A_1^2)]\exp[\frac{1}{4\bar{\omega}_2}(B_2^2+\bar{\omega}_2^2A_2^2)]\\&\exp[\alpha_r(u_Q+u_{22}d_r)+\alpha_R(\eta-d_R)].\end{aligned} \tag{E.14}$$

The derivatives of $<V>_t$, which are required for obtaining the equations of motion, can be obtained explicitly; for example, in the case of U_{vib} with two parameters, the derivatives are given by

$$\begin{aligned}\frac{\partial<V>_t}{\partial\theta}&=\frac{\partial<V>_t}{\partial u_{21}}\frac{\partial u_{21}}{\partial\theta}+\frac{\partial<V>_t}{\partial u_{22}}\frac{\partial u_{22}}{\partial\theta}+\frac{\partial<V>_t}{\partial u_Q}\frac{\partial u_Q}{\partial\theta}\\&=-\frac{\alpha_r^2}{2}(\overline{\omega}_1 s_{11}^2+\overline{\omega}_2 s_{12}^2)u_{21}<V>_t\frac{1}{\omega}\cos\theta\\&\quad-\{\frac{1}{2\overline{\omega}_1}\alpha_r s_{11}B_1+\frac{1}{2\overline{\omega}_2}\alpha_r s_{12}B_2+\alpha_r d_r\}<V>_t\sin\theta\\&\quad+\alpha_r<V>_t\zeta\sin\theta,\end{aligned}\tag{E.15}$$

$$\begin{aligned}\frac{\partial<V>_t}{\partial\zeta}&=\frac{\partial<V>_t}{\partial u_Q}\frac{\partial u_Q}{\partial\zeta},\\&=-\alpha_r<V>_t\sin\theta,\end{aligned}\tag{E.16}$$

and the derivatives with respect to η and ξ are given by

$$\frac{\partial<V>_t}{\partial\eta}=\alpha_R<V>_t,\tag{E.17}$$

$$\frac{\partial<V>_t}{\partial\xi}=0.\tag{E.18}$$

Thus, the equations of motion of η, ξ, θ, and ζ can be written in an explicit form. The equations of motion of η, ξ, θ, ζ, κ, and χ can also be expressed in an explicit form.

APPENDIX F: THE EXPECTATION VALUE OF THE POTENTIAL IN EQ.(6.7)

The functional forms of $Z(Q_R)$ and $\Delta(Q_R)$ in eq.(6.7) are given by

$$Z(Q_R)=[\tanh\{\frac{1}{M^{1/2}}(Q_R-d_R-2a_0)\}+x+1]/(x+2),\tag{F.1}$$

$$\Delta(Q_R)=u\mu^{1/2}\{1-Z(Q_R)\},\tag{F.2}$$

where $M=m_{CF_3}m_I/m_{CF_3I}$, $\mu=m_C m_{F_3}/m_{CF_3}$, and d_R is a position of the center of the wave packet at $t=0$ (see eq.(E.6)). The value of the constant, x, is chosen to be 1.9 so that the $Z(Q_R)$ satisfies the relations, $Z(d_R)=1/2$ and $Z(\infty)=1$. The value of u is set equal to 0.8. The third term of the right-hand side of eq.(6.7) can be reduced to

$$\frac{1}{2}Z(Q_R)^2\omega^2\{Q_r-\Delta(Q_R)\}^2$$

$$
\begin{aligned}
&= \frac{1}{2}\omega^2 Q_r^2 + \frac{1}{2}\{Z(Q_R)^2 - 1\}\omega^2 Q_r^2 \\
&\qquad - Z(Q_R)^2 \omega^2 \mu^{1/2} u\{1 - Z(Q_R)\} Q_r \\
&\qquad + \frac{1}{2} Z(Q_R)^2 \omega^2 \mu u^2 \{1 - Z(Q_R)\}^2 .
\end{aligned} \tag{F.3}
$$

The harmonic part, $\frac{1}{2}\omega^2 Q_r^2$, is combined with $\frac{1}{2}P_r^2$ to make ωN. The expectation value of the remaining part, the second to fourth terms in eq.(F.3), is approximately evaluated by

$$
\begin{aligned}
&\frac{1}{2}\{Z(<Q_R>_t)^2 - 1\}\omega^2 <Q_r^2>_t \\
&- Z(<Q_R>_t)^2 \omega^2 \mu^{1/2} u\{1 - Z(<Q_R>_t)\} <Q_r> \\
&+ \frac{1}{2} Z(<Q_R>_t)^2 \omega^2 \mu u^2 \{1 - Z(<Q_R>_t)^2\} .
\end{aligned} \tag{F.4}
$$

References

(1) Dirac, P.A.M. *Proc. Cambridge Philos. Soc.* **1930,** *26,* 376.

(2) Balian, R.; Veneroni, M. *Phys. Rev. Letters* **1981,** *47,* 1353, and 1765.

(3) Blaizot, J.-P.; Ripka, G. *Quantum Theory of Finite Systems*; MIT Press: Cambridge, Massashusetts, **1986.**

(4) Heller, E.J. *J. Chem. Phys.* **1976,** *64,* 63.

(5) Lee, S.Y.; Heller, E.J. *J. Chem. Phys.* **1982,** *76,* 3035.

(6) Tishby, N.Z.; Levine, R.D. *Phys. Rev.A* **1984,** *30,* 1477.

(7) Levine, R.D. *J. Phys. Chem.* **1985,** *89,* 2122.

(8) Jordan, P. *Z. Physik* **1927,** *44,* 1.

(9) Wigner, E. *Phys. Rev.* **1932,** *40,* 749.

(10) Moyal, J.E. *Proc. Cambridge Philos. Soc.* **1949,** *45,* 99.

(11) Lee, H.W.; Scully, M.D. *J. Chem. Phys.* **1980,** *73,* 2238.

(12) Rowe, D.J.; Ryman, A.; Rosensteel, G. *Phys. Rev.A* **1980,** *22,* 2362.

(13) van Veen, G.N.A.; Baller, T.; de Vries, A.E.; Shapiro, M. *Chem. Phys.* **1985,** *93,* 277.

(14) Henning, S.; Engel, V.; Schinke, R. *J. Chem. Phys.* **1986,** *84,* 5444.

(15) Herzberg, G. *Electronic Spectra of Polyatomic Molecules* Van Nostrand Reinhold, New York **1966.**

(16) Drallos, P.J.; Wadehra, J.M. *J. Chem. Phys.* **1986,** *85,* 6524.

Figure Captions

Figure 1: Transformations of the Wigner function in the phase space by U_{vib} with two parameters in eq.(2.16): (a) a parallel translation along the q-axis represented by the transformation in eqs.(3.15) and (3.16), and (b) a special-linear transformation given in eqs.(3.17) and (3.18).

Figure 2: The deformation of the Wigner function described by U_{vib} with four parameters in eq.(2.23): (a) the transformation given in eqs.(3.21) and (3.22), and (b) the transformation given in eqs.(3.23) and (3.24).

Figure 3: Vibrational distributions of the symmetric deformation of $CF_3(\tilde{X})$ produced in photodissociation of $CF_3I(\tilde{X})$ at the excitation wavelengths indicated in the figure. The closed circles represent the results of the calculation in the present study by employing the approximate U-operators, U_{trans} in eq.(2.7) and U_{vib} with two parameters in eq.(2.16). The open circles represent the results of the close-coupling calculation reported by Henning et al.[14] The same Hamiltonian (eq.(5.5)) is used in these calculations; the CF_3I molecule is regarded as a pseudo-triatomic molecule $(F_3)-C-I$.

Figure 4: Vibrational distribution of the symmetric deformation of $CF_3(\tilde{X})$ produced in the photodissociation of $CF_3I(\tilde{X})$ at the excitation wavelengths indicated in the figure. The triangles represent the results of the calculation in the present study by employing the approximate U-operators, U_{trans} in eq.(2.7) and U_{vib} with two parameters in eq.(2.16), and the closed circles represent the results by employing U_{trans} in eq.(2.7) and U_{vib} with four parameters in eq.(2.23). The open circles represent the results of the close-coupling calculation reported by Henning et al.[14] The same Hamiltonian (eq.(6.7)) is employed in these calculations. The squares represent the experimental results reported by van Veen et al.[13]

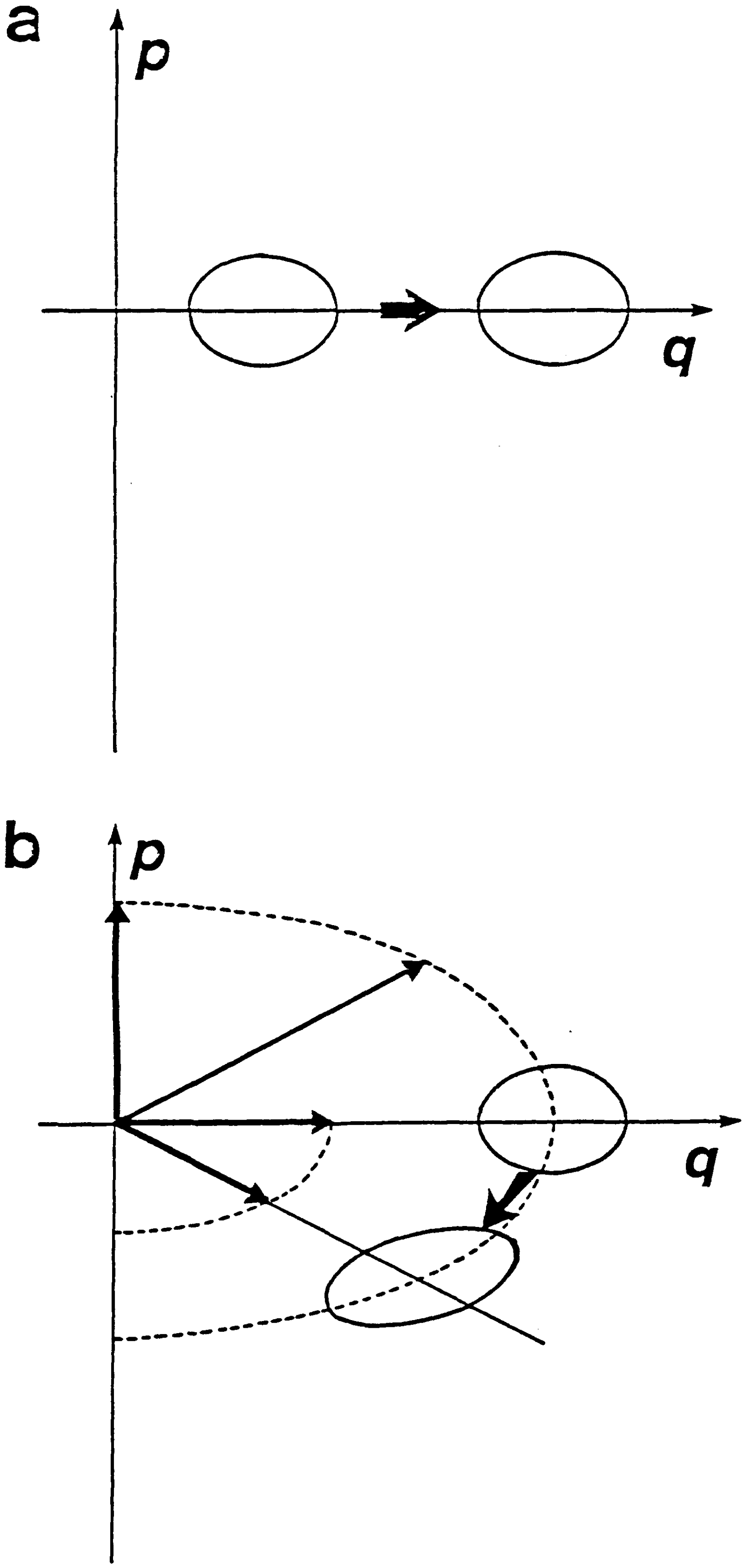

Figure 1

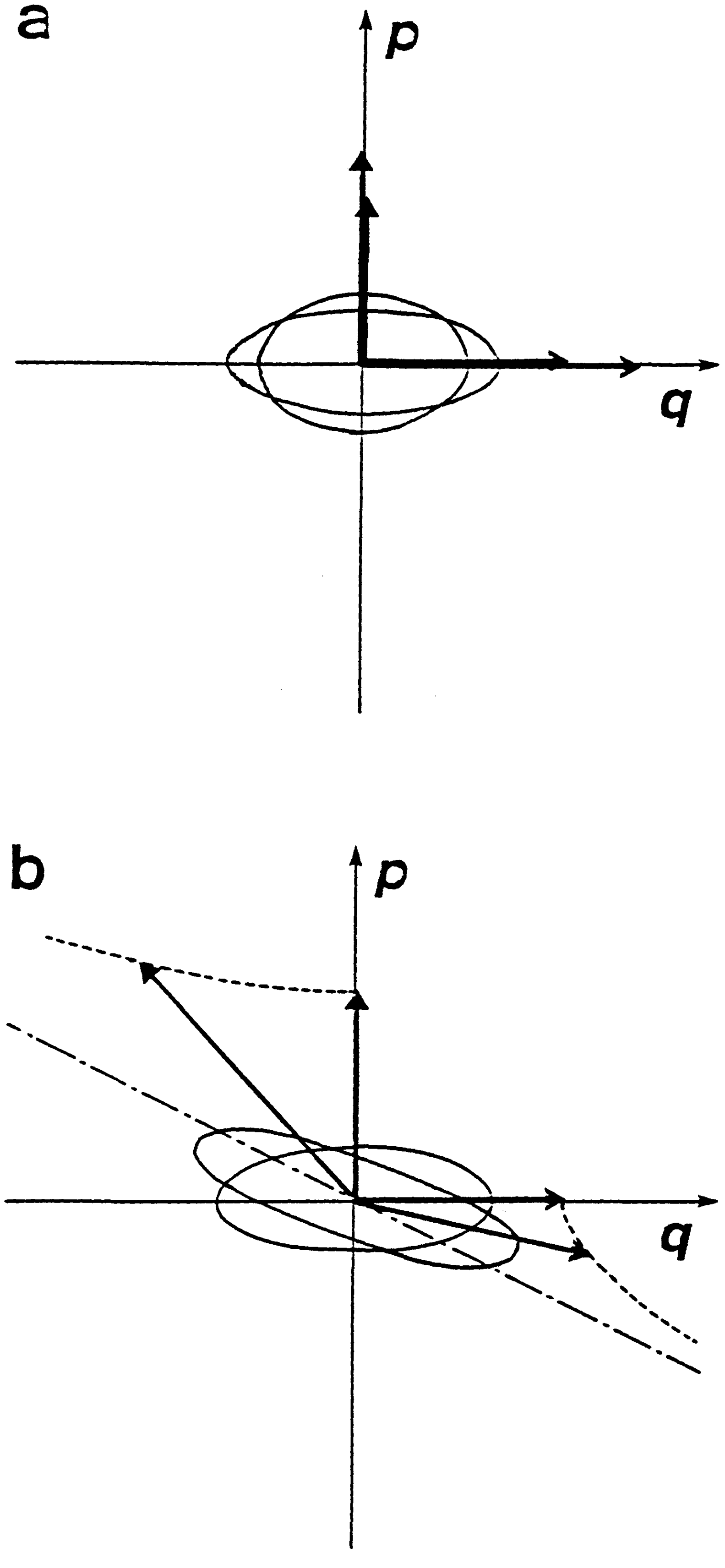

Figure 2

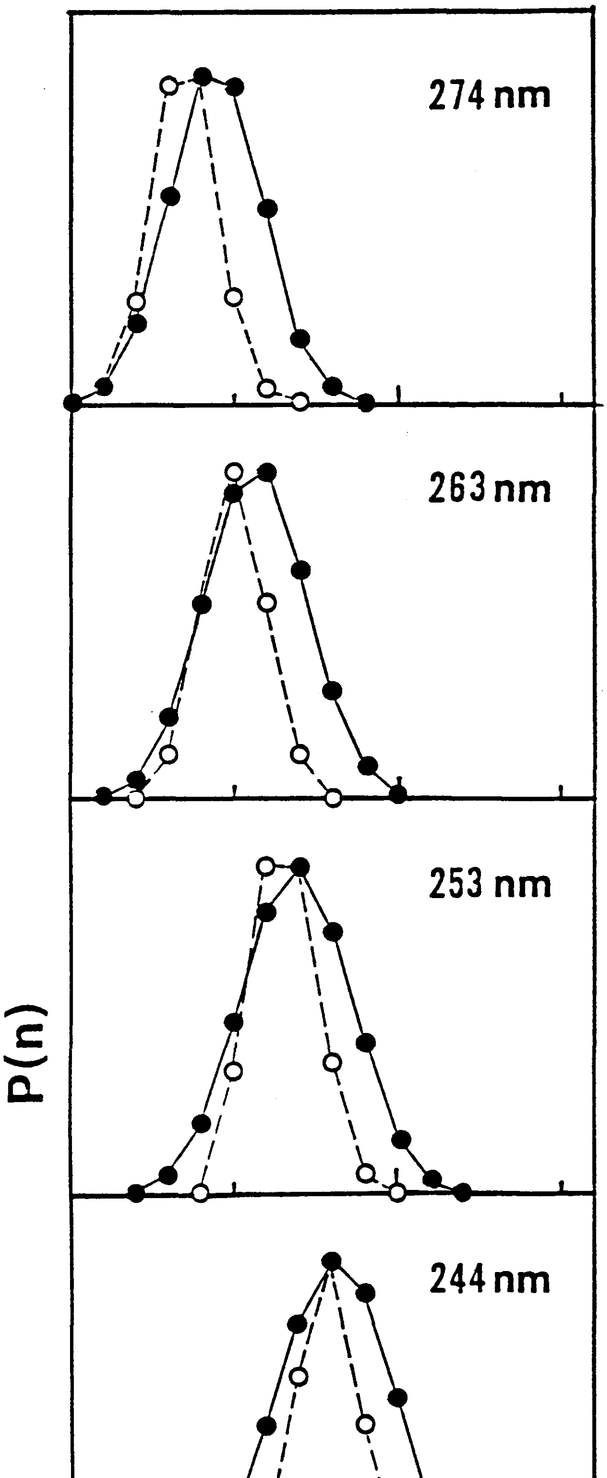

Figure 3

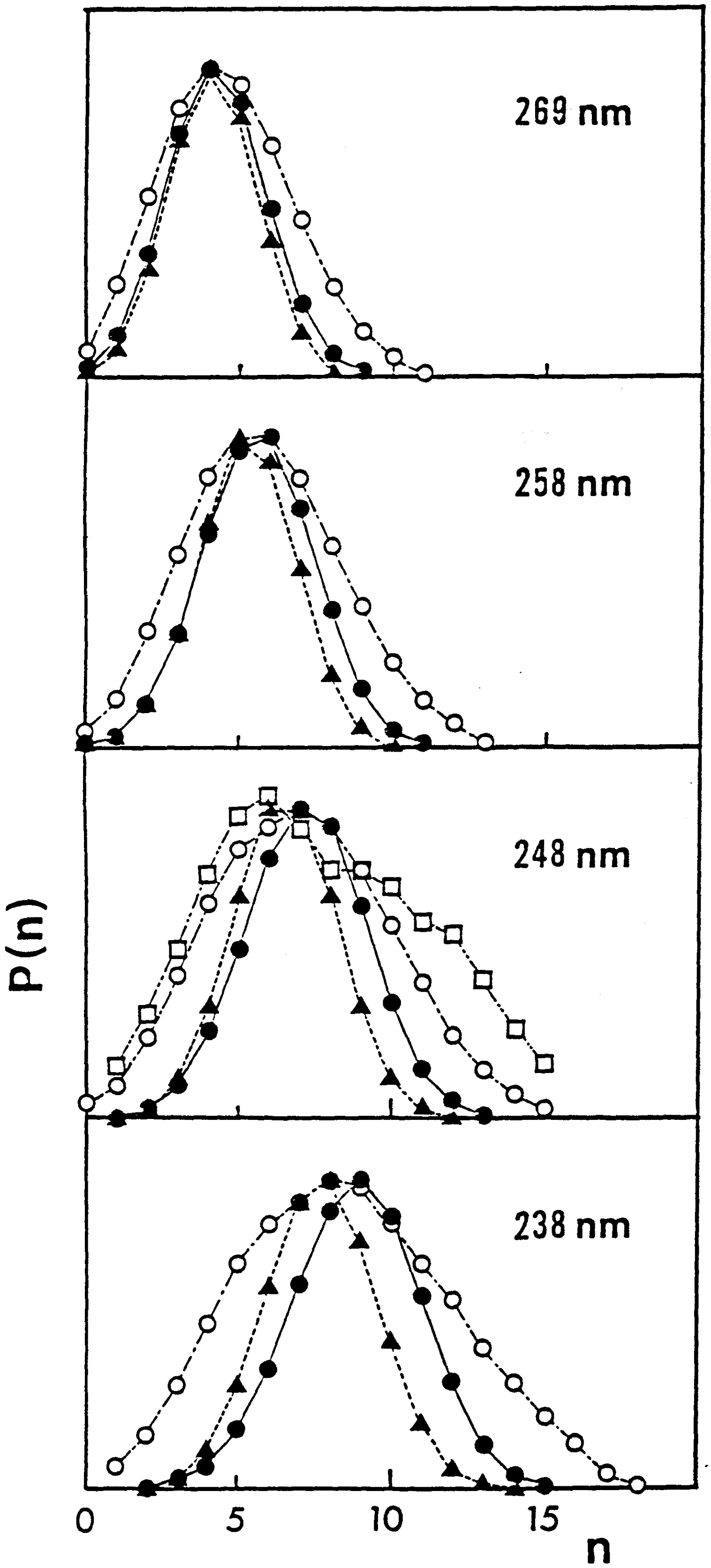

Figure 4